

A FUNDAMENTAL UNDERSTANDING OF THE EFFECTS OF CERAMIC  
PROCESSING ON PRODUCT MICROSTRUCTURE

Final Report

G. G. Long  
J. P. Cline  
J. J. Ritter

Ceramics Division  
National Institute of Standards and Technology  
Gaithersburg, MD 20899

February 15, 1992  
U.S. Army Research Office  
ARO MIPR's 120-89, 102-90, 118-91

Approved for Public Release  
Distribution Unlimited

Accesion For	
NTIS	CRA&I <input checked="" type="checkbox"/>
DTIC	TAB <input type="checkbox"/>
Unannounced <input type="checkbox"/>	
Justification .....	
By .....	
Distribution /	
Availability Codes	
Dist	Avail and/or Special
A-1	

DTIC QUALITY INSPECTED 3

**AD-A255 729**

## ITION PAGE

Form Approved  
OMB No. 0704-0188Pub  
gatt  
coll  
Davi

verage 1 hour per response, including the time for reviewing instructions, searching existing data sources, the collection of information. Send comments regarding this burden estimate or any other aspect of this report to Washington Headquarters Services, Directorate for Information Operations and Reports, 1215 Jefferson Management and Budget, Paperwork Reduction Project (0704-0188), Washington, DC 20503.

## 1. AGENCY USE ONLY (Leave blank)

## 2. REPORT DATE

February 15, 1992

## 3. REPORT TYPE AND DATES COVERED

## 4. TITLE AND SUBTITLE

A Fundamental Understanding of the Effects of Ceramic Processing on Product Microstructure

## 5. FUNDING NUMBERS

(1)

## 6. AUTHOR(S)

Gabrielle Long, James Cline, and Joseph Ritter

## 7. PERFORMING ORGANIZATION NAME(S) AND ADDRESS(ES)

Ceramics Division  
National Institute of Standards and Technology

## 8. PERFORMING ORGANIZATION REPORT NUMBER

S DIC ELECTE SEP 22 1992 AD

## 9. SPONSORING/MONITORING AGENCY NAME(S) AND ADDRESS(ES)

U. S. Army Research Office  
P. O. Box 12211  
Research Triangle Park, NC 27709-2211

## 10. SPONSORING/MONITORING AGENCY REPORT NUMBER

## 11. SUPPLEMENTARY NOTES

The view, opinions and/or findings contained in this report are those of the author(s) and should not be construed as an official Department of the Army position, policy, or decision, unless so designated by other documentation.

## 12a. DISTRIBUTION/AVAILABILITY STATEMENT

Approved for public release; distribution unlimited.

92 9 22 007

420/958 92-25576 5708

## 13. ABSTRACT (Maximum 200 words)

This is the final report arising from our research program involving the investigation of processing/microstructure relationships in selected ceramic systems. The first year of this program was dedicated to the development and detailed assessment of the novel neutron scattering and x-ray diffraction techniques required for the measurement of ceramic microstructure evolution as a function of sintering and chemistry. The next two years of the program were used to study several systems in detail, and has led to some remarkable conclusions which have changed the way in which the sintering stages in different systems are understood.

The sintering behavior of a ceramic body and the properties of the ceramic product depend directly on the internal microstructure. The goal of our research program with the ARO has been to investigate well-characterized systems and to measure microstructure evolution during ceramic processing in order to obtain an improved understanding of the relationships between processing and microstructure. This approach has led to progress in improving process models and to improved predictability of product microstructure.

## 14. SUBJECT TERMS

Ceramic Processing, Microstructure Characterization, Processing Models, Intelligent Processing

15. NUMBER OF PAGES  
55

16. PRICE CODE

## 17. SECURITY CLASSIFICATION OF REPORT

UNCLASSIFIED

## 18. SECURITY CLASSIFICATION OF THIS PAGE

UNCLASSIFIED

## 19. SECURITY CLASSIFICATION OF ABSTRACT

UNCLASSIFIED

## 20. LIMITATION OF ABSTRACT

UL

## 1. FOREWARD

This is the final report arising from our research program involving the investigation of processing/microstructure relationships in selected ceramic systems. The first year of this program was dedicated to the development and detailed assessment of the novel neutron scattering and x-ray diffraction techniques required for the measurement of ceramic microstructure evolution as a function of sintering and chemistry. The next two years of the program were used to study several systems in detail, and has led to some remarkable conclusions which have changed the way in which the sintering stages in different systems are understood.

The sintering behavior of a ceramic body and the properties of the ceramic product depend directly on the internal microstructure. The goal of our research program with the ARO has been to investigate well-characterized systems and to measure microstructure evolution during ceramic processing in order to obtain an improved understanding of the relationships between processing and microstructure. This approach has led to progress in improving process models and to improved predictability of product microstructure.

**2. TABLE OF CONTENTS**

<b>Forward</b>	<b>1</b>
<b>List of Appendices</b>	<b>3</b>
<b>List of Illustrations</b>	<b>4</b>
<b>Final Report</b>	<b>5</b>
<b>Appendices</b>	<b>17</b>

## **List of Appendices**

- I. Multiple Small-Angle Neutron Scattering Characterization of the Densification of Alumina**
- II. Evolution of the Pore-Size Distribution in Final-Stage Sintering of Alumina Measured by SAXS**
- III. Characterization of the Densification of Alumina by Multiple SANS**
- IV. The Effect of Green Density and the Role of MgO Additive on the Densification of Alumina Measured by SANS**
- V. SANS Characterization of Processing/Microstructure Relationships in the Sintering of Crystalline and Glassy Ceramics**

## List of Illustrations

- Figure 1. Effective pore radii for the 13-series alumina as a function of %TD derived from MSANS, from Porod scattering, and from MIP.
- Figure 2. Effective pore radii,  $R_{\text{eff}}(0)$  as a function of %TD for all four series of samples. The number appearing near the leftmost symbols is the average green body density for each series.
- Figure 3. Pore volume fraction, normalized to S/V, as a function of densification (% TD) for silica and alumina.
- Figure 4.  $R_{\text{eff}}(0)$  as a function of percent theoretical density for silica and alumina.
- Figure 5. In situ x-ray diffraction during the sintering of alumina. Spectra were measured for 15 minutes after 2 minutes of equilibration at temperature.
- Figure 6. Volume size distribution,  $V(D)$ , of the pores derived using the maximum entropy procedure, plotted as a function of diameter, D, for the MgO-doped alumina samples. For clarity, smoothed lines have been drawn through the data points.
- Figure 7. Scanning electron micrographs of undoped alumina samples 13-7 (97.0 % TD), 13-8 (99.0 % TD) and of MgO-doped samples D-6 (97.5 % TD) and D-7 (99.0 % TD).

## 2. INTRODUCTION

Starting with the multiple small-angle neutron scattering formalism originally developed by Berk and Hardman-Rhyne<sup>1</sup> at NIST, we applied it to such questions as:

- o What effect does the green-body density have on pore-size evolution and grain-size evolution during sintering?
- o What is the role of a sintering aid in the intermediate and final stages of sintering?
- o What signals the beginning of final stage sintering and how does the porosity evolve as full theoretical density is approached?
- o How do the sintering mechanisms (surface and volume diffusion; viscous flow) change the porous-phase evolution?

The answer to this last question, for example, is beginning to have a major impact on the community because the results differ significantly from classical well-accepted theory. The answers to all of these questions will be described in the neutron scattering section (Section 3) which follows.

High temperature x-ray diffraction, incorporating several ceramic-specific features, has been used to investigate in-situ sintering in terms of the evolving grain sizes and phases of several systems. In addition, we have studied the sintering kinetics of materials synthesized at NIST under the support of this program. Finally, the evolution of pore sizes and size distributions during final-stage sintering has been investigated using small-angle x-ray scattering. The latter results indicate that for many applications, a product with less than full theoretical density leads to properties superior to a product with nearly full density. These results will be described in the x-ray section (Section 4) which follows.

### 3. SMALL-ANGLE NEUTRON SCATTERING CHARACTERIZATION

The central thrust of this research program was the application of advanced scattering techniques to study the processing/microstructure relationships in real ceramic materials, leading to an improved understanding of ceramic process models. In this study, it was possible for the first time to follow particle sizes, pore sizes, size distributions and morphology from the earliest "green" state, through intermediate stage sintering, through to the final stages of sintering.

The first system that we studied was undoped  $\alpha$ -alumina, which served as a model material. Our intention was to test the quantitative capabilities of our new scattering techniques with a system which is well understood. We measured the effective pore radii for alumina 56-98% dense and found that we could not only quantify the pore sizes but we could also identify the transition from intermediate-stage sintering to final-stage sintering from the morphological change which takes place in the shape of the pores present at each stage. In the intermediate stage we measure the cross sections of the interconnected (i.e., open) pore channels, whereas in the final stage we measure the diameters of isolated pores. Our ability to measure the density at which the transition from intermediate to final stage takes place turned out later in this program to be essential for understanding the effect of sintering aids on microstructure and the effect of green-body density on product microstructure. These results will be detailed below. At this time, we show in Figure 1 the effective pore radius as a function of sintering for undoped alumina. For densities between 55% and 87% of theoretical density, the effective pore radius remains nearly constant. This, at first surprising, result for intermediate stage sintering is actually consistent with sintering models in which the stable topological decay of an interconnected pore network is taking place. This constant-radius result is confirmed by mercury porosimetry results and Porod scattering results on the same samples. For densities between 90% and 98% dense, the radii of the remaining pores

increases monotonically. We have identified these radii as being a measure of the pore size distributions of the final stage of sintering, in which the pores are isolated from one another and the decay in percent porosity is no longer stable. Thus MSANS and Porod scattering have identified for the first time where the transition to isolated porosity takes place, and has led to strong confirmation of the topological decay model<sup>2</sup> for intermediate-stage sintering, which until now has probably not received the attention it deserves.

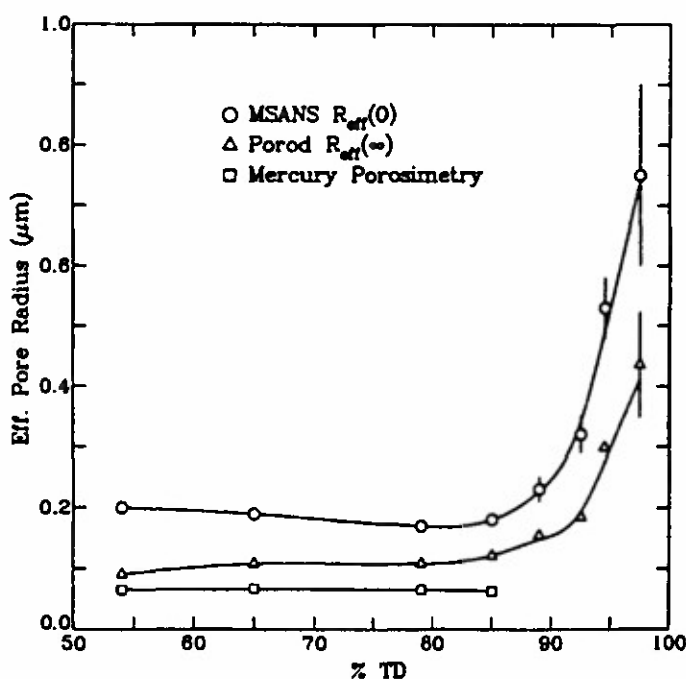


Fig. 1. Effective pore radii for the 13-series alumina as a function of %TD derived from MSANS, from Porod scattering, and from MIP.

Next we studied the effect of green density and the role of a sintering aid on the densification during sintering of alumina. It is well known that high green-state porosity leads to difficulties in sintering, and it is also well known the addition of small amount (0.25 wt %) of MgO leads to a much finer-grained and denser ceramic product. It was not known, however, why a low green-body density could not be overcome by sintering or the mechanism by which the addition of MgO inhibits grain growth to form a much finer-grained denser ceramic product with fewer incipient porous flaws. In research supported by this program, we examined the sintering of alumina with and without additive, and we followed the course

of the pore size distributions starting with green densities from 46% to 53%. The results showed unequivocally that the initial connectivity in the green body determined the size of the pores in the intermediate sintering stage, which are always constant (see Figure 2). Further, it was demonstrated that the density at which the transition from stable intermediate-stage sintering to final-stage sintering takes place is determined in part by the green body density. The denser the green body, the later the transition takes place, and the smaller the isolated pores which remain at the end of the final stage.

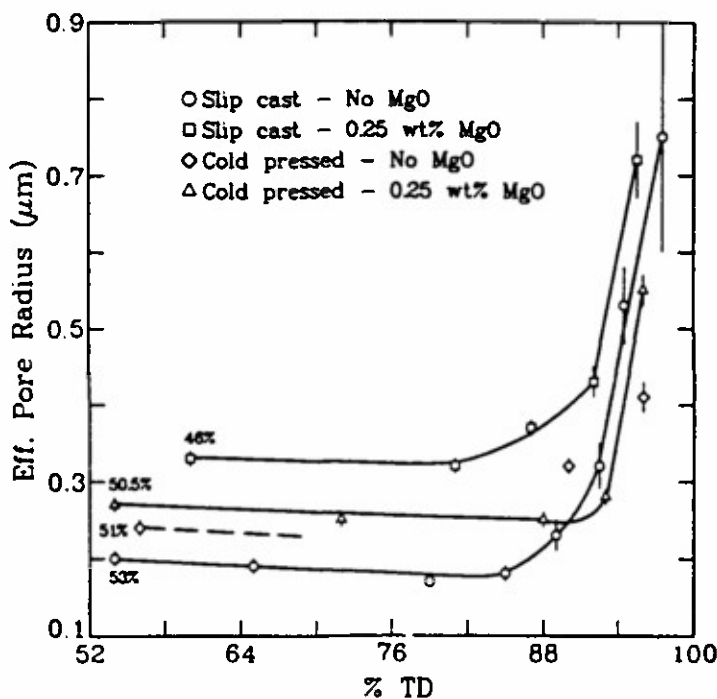


Fig. 2. Effective pore radii,  $R_{\text{eff}}(0)$ , as a function of %TD for all four series of samples. The number appearing near the leftmost symbols is the average green body density for each series.

With regard to the effect of sintering aid, it was learned that the addition of 0.25 wt % MgO can overcome some of the problems associated with low green body density. Our MSANS data indicated that even with low green body density, the onset of final stage sintering is delayed. This leads to finer grains and smaller pores in the product material because the stable intermediate densification stage is extended to densities well over 92% of theoretical.

Although it is difficult to achieve a concensus regarding many aspects of sintering mechanisms, there is general agreement that the driving force for sintering is the reduction in surface free energy. The shape of the minimum free energy surface influences strongly the microstructure evolutions during processing. In another research problem investigated with the support of this ARO program, we measured the pore sizes, size distributions, surface areas and number distributions of the porous phase in glassy silica and in polycrystalline alumina. In this way we had a probe of two very different sintering mechanisms: viscous flow in the processing of the glass, and surface and volume diffusion in the processing of the polycrystalline material. The goal was to gain a quantitative measure of the structural evolution when different sintering mechanisms dominate densification. The remarkable result of this study was that, from a topological point of view, both systems evolve the same way. This is shown in Figure 3, where we show the pore volume fraction,  $\phi$ ,

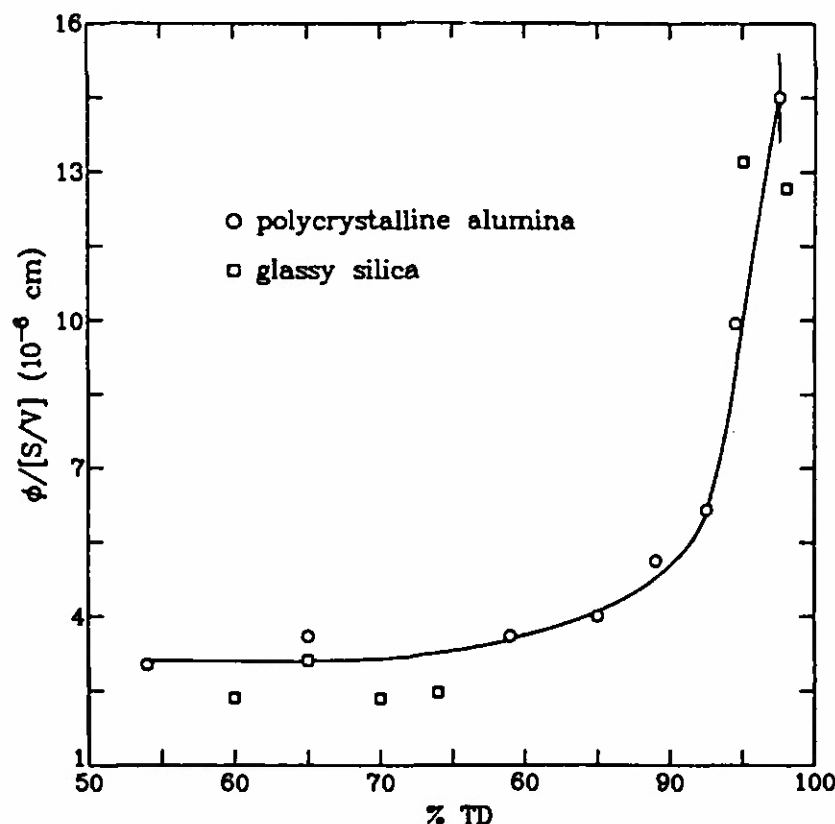


Fig. 3. Pore volume fraction, normalized to  $S/V$ , as a function of densification (% TD) for silica and alumina.

normalized to the pore surface area per unit volume,  $S/V$ , as a function of densification. The points for both systems for this topological parameter,  $\phi/(S/V)$ , fall on a universal curve. However, in terms of the actual pore sizes and morphology, the two sintering mechanisms lead to two very different structural evolution signatures. In Figure 4, we show the average pore

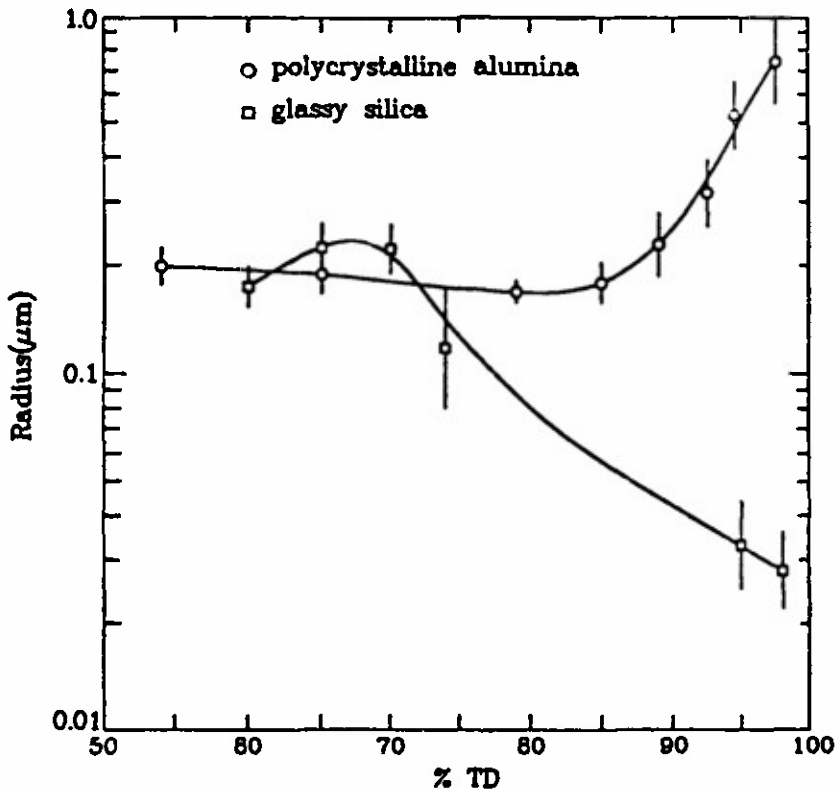


Fig. 4.  $R_{\text{eff}}(0)$  as a function of percent theoretical density for silica and alumina.

radius as a function of densification for the two systems. The alumina results are familiar from Figure 1. The silica results show that the average pore size increases and then decreases in the intermediate stage instead of remaining constant. This is because, in the glassy system, the aggregates first densify, removing the smaller pores inside the clusters. This leaves behind larger spaces (pores) between the clusters. The peak radius identifies the point in the densification at which all of the small pores have been removed. After that, the porc size decreases rapidly. In addition, there is a morphological change in the pore shape that goes

from interconnected cylindrical channels to interconnected flat (disklike) pores in the final stage. The transition to collapsed porosity in silicia is currently under further investigation. This densification behavior is attributed to the lack of constraints associated with the absence of a grain boundary in the glassy system. The density of the green body plays a much less important role when viscous flow is the operative sintering mechanism.

Further research on processing/microstructure relationships will include silicon nitride sintering as a natural progression arising from the program just completed. The new research will be directed toward examining conventional silicon nitride processing using variety of sintering aids, microwave-assisted reaction-bonded silicon nitride which is not sintered and involves no sintering aids, and nanophase processing of silicon nitride which also involves no sintering aids. The goal will be to understand the underlying mechanisms for silicon nitride fabrication leading to optimized reproducible processing of this promising ceramic.

#### 4. SYNTHESIS AND X-RAY CHARACTERIZATION

The sol gel method is one of the most active areas of ceramics research. Part of the synthesis and x-ray program supported by the ARO was devoted to exploring the sol gel method with regard to new possibilities in the preparation of alumina. Earlier investigations focussed on boehmite ( $\text{AlOOH}$ ), its conversion to  $\alpha$ -alumina, and the subsequent sintering behavior. In this program we have synthesized and evaluated a hydrous vitreous alumina precursor (HVAP). These precursors have been prepared both with and without the addition of  $\alpha$ -alumina seed particles, and their behavior as they are converted to corundum ( $\alpha$ -alumina) has been compared to that of microcrystalline boehmite precursors. Our x-ray diffraction and differential thermal analysis data indicated that the HVAP material converts to corundum at a lower temperature than the boehmite. Moreover, the presence of  $\alpha$ -alumina "seed" particles in these precursors lowers the respective transition temperatures even further. A comparison of x-ray diffraction intensities from seeded and unseeded samples suggests that the presence of

seed particles has an effect on the formations of  $-Al-OH-Al-$  and  $-Al-O-Al-$  networks. Low alumina recoveries from gravimetric alumina-content assays on the HVAP indicate that it chemically bonds water and possibly alcohol into its structure. In contrast, the boehmite precursors have alumina yields more consistent with theoretical predictions. We conclude that the HVAP materials offer a new route to synthesis of alumina, and further research is planned to continue to explore these possibilities.

As part of this research program, we have measured x-ray diffraction profiles during the in-situ sintering of alumina. (See Figure 5.) The peaks at  $2\theta = 40^\circ$  and  $58^\circ$  arise from the molybdenum heating strip. The sintering process causes the width and the intensity of the sample diffraction profiles to change as the temperature increases. The initial submicron size of the crystallites (Sumitomo, HKP50,  $0.2\mu m$ ) causes the diffraction peaks to be broad. During the early stage of sintering, crystallites grow out of this range and the diffraction profiles become narrower. A second effect is extinction, which noticeably reduces the diffracted intensity of the strongest lines as the crystallites coarsen to sizes larger than those which can be followed by peak broadening. Both effects are sometimes subtle alterations of the diffraction profiles. The analysis of this data requires that the diffuse thermal scattering be removed and the effects of extinction be derived from the fitting of the profile shapes. Such analyses are underway and the grain-size evolution data is expected to be complementary to the pore-size evolution results described earlier.

Finally, we describe a project in which we have investigated the pore-size distribution in final-stage sintering by means of small-angle x-ray scattering. The values of the median size and the width of the pore-size distributions are of particular interest in gaining an understanding of the processes which take place as a ceramic body approaches full theoretical density. The distribution of pore sizes is related to distribution of dihedral angles between grains, which are in turn directly related to the driving force for sintering, i.e., the surface free energy. This research was stimulated, at least in part, by our neutron scattering results which indicated that the median size of the few remaining pores in final stage sintering

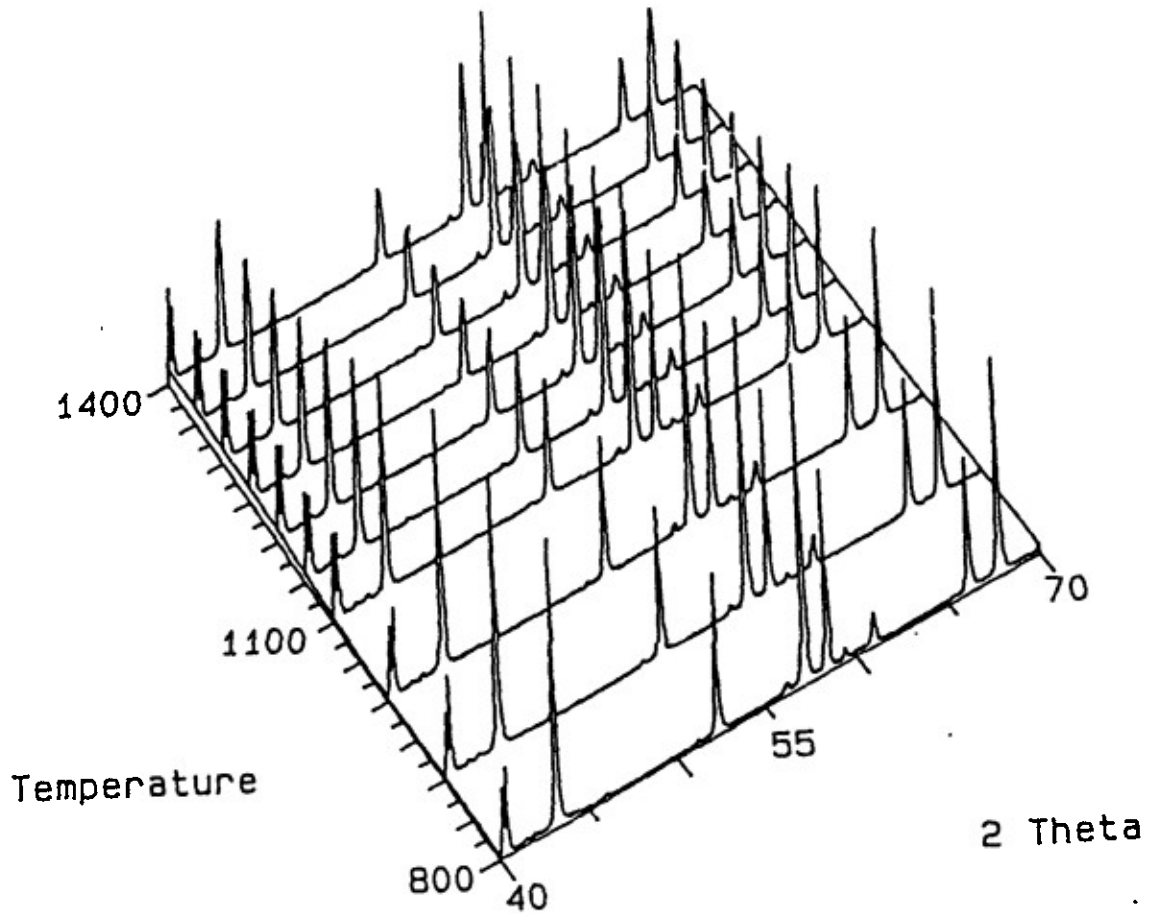


Fig. 5.

In situ x-ray diffraction during the sintering of pure alumina. Spectra were taken in 15 minutes after 2 minutes for equilibration at temperature.

always increased as density increased. We measured samples of alumina, both doped with MgO and undoped, that were between 97% and more than 99% dense. The high resolution x-ray results showed that the mean pore radius continues to increase as density increases, confirming and extending the neutron results. In addition, it was found that the pore-size distribution broadens significantly (Figure 6) as density increases. Scanning electron micrographs (Figure 7) of these specimens support the scattering results and show a concomitant growth of the alumina grains. Lastly, for a given sample density, the average grain and pore sizes are markedly smaller, and their size distributions are narrower, in the MgO-doped case. This study gives statistical validity to earlier research<sup>3</sup> which suggested that the distribution of dihedral angles between grains, and thus the grain and pore size distributions, are narrower in MgO-doped alumina than undoped alumina at ~99% dense.

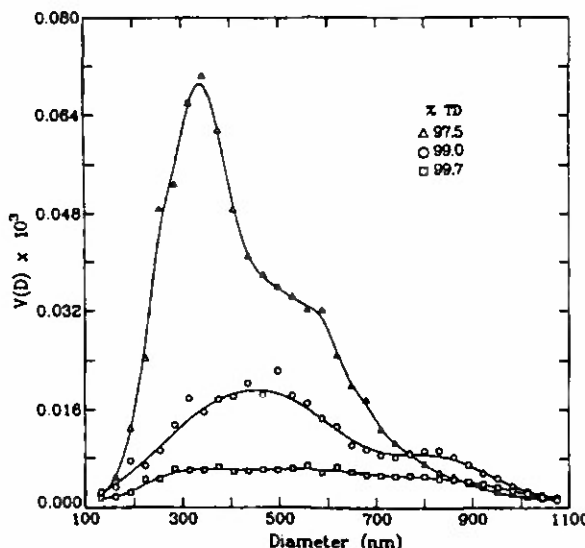
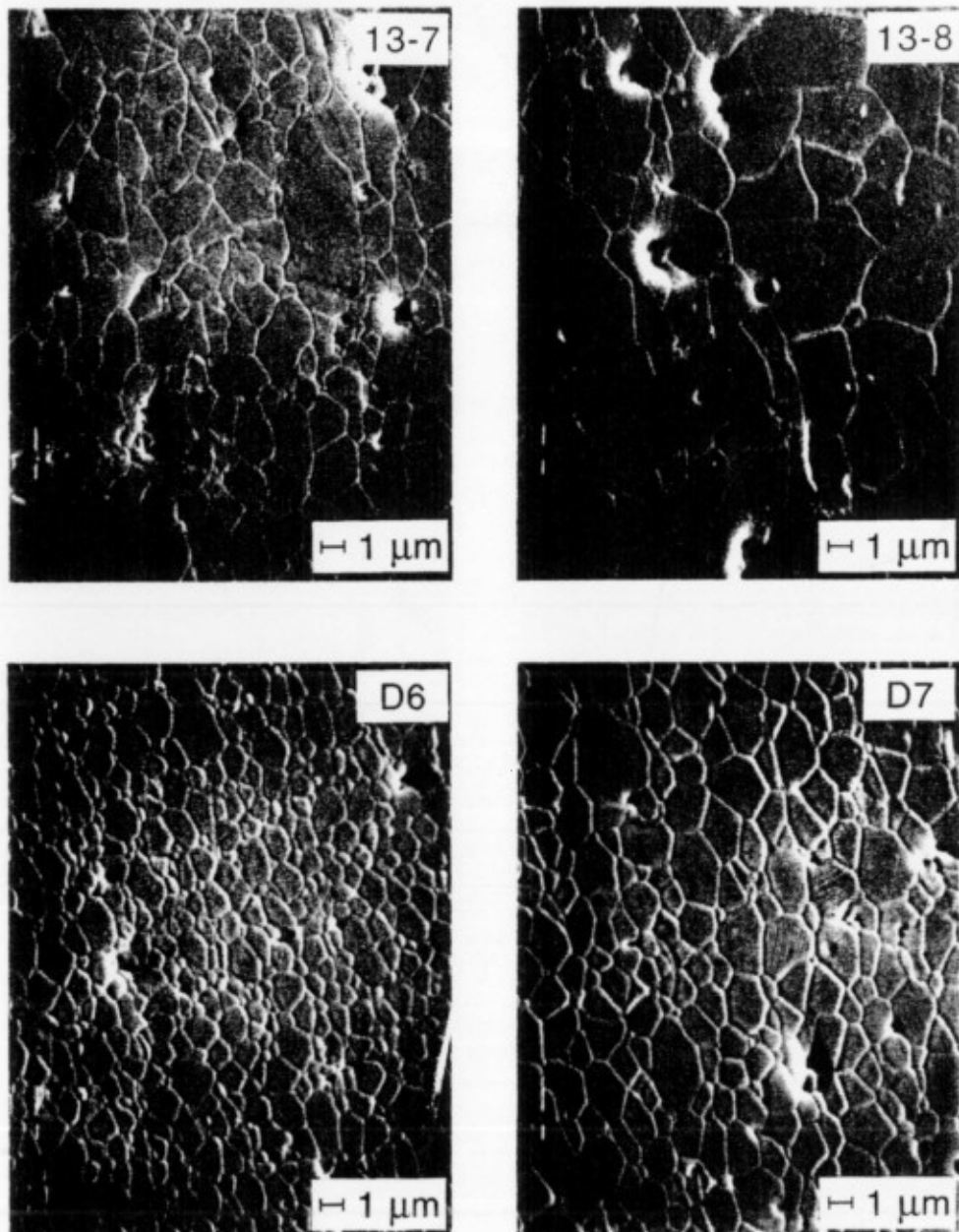


Fig. 6. Volume size distributions  $V(D)$ , of the pores derived using the maximum entropy procedure, plotted as a function of diameter,  $D$ , for the MgO-doped alumina samples. For clarity, smoothed lines have been drawn through the data points.



**Fig. 2.** Scanning electron micrographs of undoped alumina samples 13-7 (97.0% TD), 13-8 (99.0% TD) and of MgO-doped samples D-6 (97.5% TD) and D-7 (99.0% TD).

## REFERENCES

1. N. F. Berk and K. A. Hardman-Rhyne, *J. Appl. Cryst.* 18 (1985) 467-472; and *J. Appl. Cryst.* 21 (1988) 645-651.
2. R. T. DeHoff, R. A. Rummel, H. P. LaBuff, and F. N. Rhines, in Modern Developments in Power Metallurgy, edited by H. H. Hausner, Vol. 1, (1966), New York: Plenum Press, pp. 310-331; and F. N. Rhines and R. T. DeHoff, in Sintering and Heterogeneous Catalysis, Materials Science Research, edited by G. C. Kuczynski, A. E. Miller and G. A. Sargent, Vol. 16, (1984), New York: Plenum Press, pp. 49-61.
3. C. A. Handwerker, J. M. Dynys, R. M. Cannon and R. L. Coble, *J. Amer. Ceram. Soc.* 73 (1990) 1371-1377.

**MULTIPLE SMALL ANGLE NEUTRON SCATTERING CHARACTERIZATION  
OF THE DENSIFICATION OF ALUMINA**

S. KRUEGER\*, G.G. LONG\* and R.A. PAGE<sup>†</sup>

\*Materials Science and Engineering Laboratory, National Institute of Standards and Technology (formerly NBS), Gaithersburg, MD 20899

<sup>†</sup>Department of Materials and Mechanics, Southwest Research Institute, 6220 Culebra Road, San Antonio, TX 78228

**ABSTRACT**

Multiple small angle neutron scattering (MSANS) was used to follow the evolution of the pore size distribution in  $\alpha\text{-Al}_2\text{O}_3$  through the intermediate and final stages of sintering. This technique makes it possible to determine microstructure morphology in the 0.08 to 10  $\mu\text{m}$  size regime under conditions where the total scattering cross-section is dominated by elastic incoherent multiple scattering, as is often the case for ceramics. The MSANS results indicate an initial decrease in the effective pore radius from 0.19  $\mu\text{m}$  at 57% of theoretical density (TD) to 0.17  $\mu\text{m}$  at 79% TD. As the sample density further increased, there was a transition region after which the effective pore radius grew rapidly to  $\geq 0.5 \mu\text{m}$  at 98% TD. Standard Porod analysis on scattering by the same samples also indicates a transition between the intermediate and final stages of processing. Both sets of results support a topological model of sintering in which the interconnected pore network in the intermediate stage of sintering decays in a stable manner. The pores become fewer, while retaining the same diameter, as densification proceeds. In the final stage, isolated pores remain.

**INTRODUCTION**

Knowledge of the microstructure evolution as a function of thermal processing is important for the development of process models in ceramics. For dilute concentrations of scatterers between 1 nm and 100 nm, small angle neutron scattering (SANS) is invaluable for the determination of bulk microstructural parameters. The complementary MSANS technique, first described by Berk and Hardman-Rhyne [1,2], is applicable when the scatterers are in the 0.08  $\mu\text{m}$  to 10  $\mu\text{m}$  size range. In such cases, the total scattering cross-section is dominated by elastic incoherent multiple scattering. Effective (volume-weighted average) radii of the scatterers are extracted by measuring the wavelength dependence of the scattering curves at low scattering vector. Thus, it becomes possible to investigate thicker and denser materials than is possible with SANS. Of the many methods available for the determination of microstructure morphology, MSANS and SANS have the advantage of being able to measure both open and closed pores.

In this work, an investigation of the microstructure evolution of  $\alpha\text{-Al}_2\text{O}_3$  as a function of thermal processing was conducted. This is a system for which the process models [3] are comparatively well-understood, and thus it can serve as a model system for the new scattering technique. An earlier study of microstructure evolution as a function of thermal processing in porous silica [4] has demonstrated that MSANS and SANS effectively cover the full range of relevant microstructure sizes. For the alumina system, MSANS was used throughout the intermediate and final stages because the pore sizes were large. Standard Porod [5] analysis, performed on the high angle portion of the scattering curves, was used to determine

total scattering surface areae, from which effective (surface area-weighted average) pore radii were calculated.

### MSANS THEORY

The interaction of neutrone with matter ie determined by the phase shift,  $\nu$ , that a plane wave undergoes in traversing a particle of radius,  $R$ . This phase shift depends on the index of refraction of the particle or void,  $\Delta n$ , relative to the scattering matrix such that  $\nu = (4\pi/\lambda)\Delta n R$ , where  $\lambda$  is the neutron wavelength.  $\Delta n = \Delta b \lambda^2 / 2\pi$ , where  $\Delta b$  is the relative scattering length density, or contrast, of the particle or void:

$$\Delta b = \sum_{cell} b_i / V_{cell} - b_{matrix} \quad (1)$$

Thus, the phase shift  $\nu$  is given by

$$\nu = 2\Delta b R \lambda, \quad (2)$$

meaning that it is directly dependent on the material contrast, the dimensions of the scatterer and the neutron wavelength.

If  $\nu \ll 1$ , the measurement is in the conventional SANS diffraction regime. The form of the scattering curve as a function of the scattering wavevector  $Q$  (where  $|Q| = 2\pi/\lambda$ , and  $\epsilon$  is the scattering angle) is independent of neutron wavelength and depends only on the particle dimensions. On the other hand, if  $\nu \gg 1$ , the experiment involves multiple refraction, where every particle scatters and geometrical optics applies.

The scattering curve depends on neutron wavelength as  $\lambda^2$ . When  $\nu \leq 1$ , the MSANS diffraction formalism applies [1,2] and the scattering curve broadens as a function of neutron wavelength. The predicted neutron intensity is approximately gaussian at  $Q = 0$  and has a width proportional to  $\lambda^2$ . Even though the wavelength dependence is the same as that for multiple refraction, the fact that  $\nu \leq 1$  allows an effective particle radius,  $R_{eff}(0)$ , to be determined from the wavelength dependence of the radius of curvature,  $r_c$ , at  $Q = 0$  of the scattering spectrum.

A measure of the amount of multiple scattering is given by the parameter  $\bar{z}$  which is the sample thickness,  $z$ , divided by the statistical mean free path length,  $f$ .

$$\bar{z} = z/f = 1.5 \phi z (\Delta b \lambda)^2 R_{eff}(0), \quad (3)$$

where  $\phi$  is the volume fraction of scatterers and the dimensions of the parameters are expressed in centimeters.  $\bar{z}$  is related to the scattering radius of curvature via an empirical relation [2]

$$r_c[QR] = 0.926(\bar{z} \ln^{0.85-0.5} \bar{z}) \text{ for } \bar{z} > 5. \quad (4)$$

For  $\bar{z} > 10$ , the agreement with the theory is better than 0.1%. The analysis requires only the sample thickness, the wavelength dependence of the radius of curvature, the scattering volume fraction (which is a refinable parameter) and the scattering length density to derive  $R_{eff}(0)$ . For large  $Q$ , the scattering is determined by the single scattering Porod law [5], which applies even when the region near  $Q = 0$  is dominated by multiple scattering [1].

### ALUMINA SAMPLES

The samples were Baikowski alumina powder (CR6), slipcast to an average green density of 53% TD. The slip consisted of 43.5 vol.% alumina powder mixed into water, along with 0.5 wt.% of a polyelectrolyte dispersant (Darvan C). The suspension was ultrasonicated for 15 min and allowed to sit overnight before being poured into moulds with teflon rings on top of plaster-of-paris blocks. After 55 minutes, the moulds were removed from the blocks and sealed in a container overnight. The partially-dried samples were then removed from the moulds and annealed in containers for 2 days. The containers were then opened to the air for an additional 5-7 days before a series of oven-drying steps were performed as follows: 2 days at 64°C, 1 day at 81°C, 1 day at 102°C and 1 day at 116°C, after which a dry, solid green body is obtained. In this fashion, a family of eight nearly-identical samples were prepared.

During sintering, samples were removed one by one from the furnace to yield examples of material between 56.5 and 98% TD. Figure 1 is a time-temperature curve for the sintering. Each circle represents a sample removed from the furnace and the number alongside is the measured %TD.

### NEUTRON SCATTERING MEASUREMENTS

Measurements were made at the 20 MW research reactor at the National Institute of Standards and Technology (NIST, formerly the National Bureau of Standards). The NIST SANS facility [6] includes a velocity selector for choosing the mean incident wavelength,  $\lambda$ , of the neutrons with a spread,  $\Delta\lambda/\lambda = 0.25$ . Copious neutron fluxes can be obtained in the wavelength region between 0.5 and 2.0 nm due to a cryogenic moderator installed in the reactor core. The neutron beam is collimated with a 12 mm aperture which follows the velocity selector and a 8 mm aperture which precedes the sample

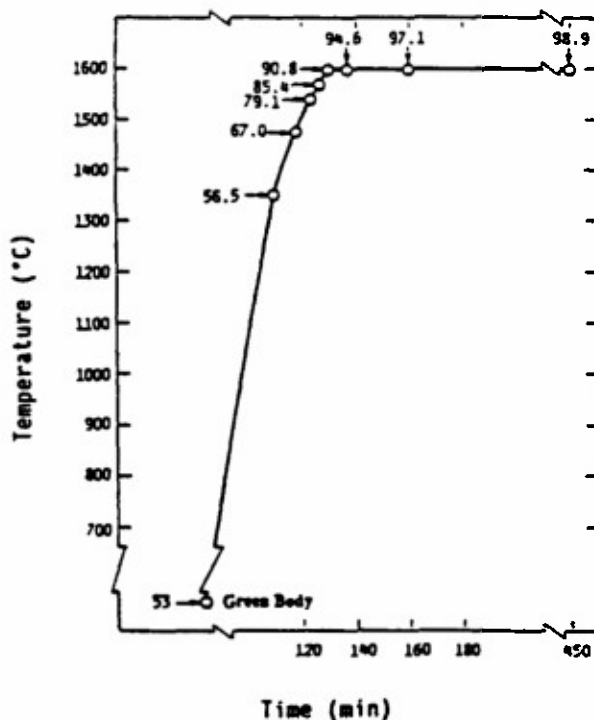


Figure 1. Sintering time-temperature curve for the alumina samples sintered to densities ranging from 56.5 to 98% TD.

position. Scattered neutrons are detected by a  $64 \times 64 \text{ cm}^2$  position-sensitive detector divided into  $128 \times 128$  pixels. The data are circularly averaged to produce one-dimensional intensity,  $I(Q)$ , versus  $Q$  curves. For Porod analysis, scattering cross-sections are placed on an absolute scale by normalizing to that of a standard silica gel sample measured under the same conditions.

## RESULTS AND DISCUSSION

MSANS measurements were performed on each sample at a minimum of 5 different neutron wavelengths. The scattering curves exhibited the expected broadening with increasing neutron wavelength. Gaussian fits were made to each curve in the range extending from 90% of  $I(0)$ , the intensity at  $Q=0$ , to 45% of  $I(0)$ . The scattering curves no longer fit well to a gaussian in the higher  $Q$  region, where the scattering intensity falls below 40% of  $I(0)$ . For each fit, a radius of curvature was extracted from the standard deviation,  $r_c = \sqrt{1/2\sigma}$ . Blank spectra (with no scatterer in place), measured at each wavelength, were also fitted in order to make a correction for the instrument function. The measured values of  $r_c$  (symbols) along with the theoretical values determined using the MSANS formalism (solid lines) are plotted versus neutron wavelength in Figure 2 for each sample. The densities measured volumetrically and those determined by the neutron scattering are shown in the inset to the figure. The derived values of  $R_{aff}(0)$  fit the theory well for all samples measured.

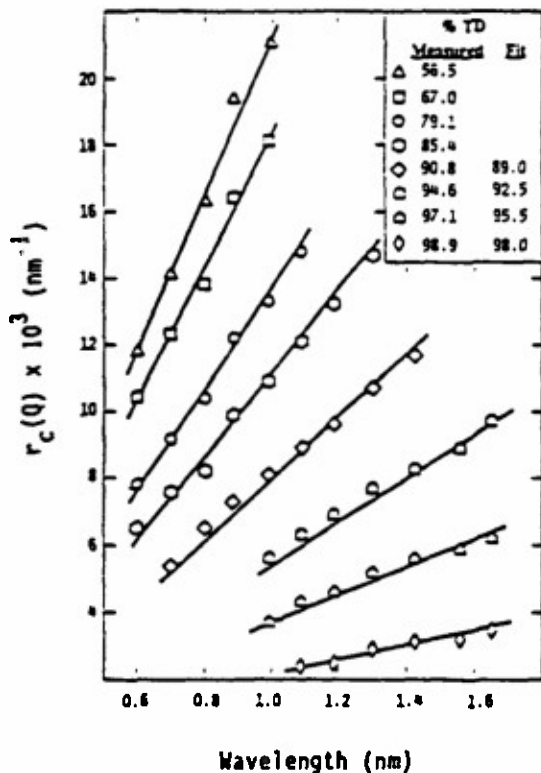


Figure 2. Measured radii of curvature (symbols) and the corresponding theoretical radii (solid lines) as a function of neutron wavelength for all samples measured. The sample densities measured volumetrically are shown in the inset, along with those determined by the neutron scattering measurements, if different.

$R_{\text{eff}}(0)$  was derived from Figure 2 for each alumina sample. A plot of  $R_{\text{eff}}(0)$  as a function of %TD is illustrated in Figure 3, along with the average pore radius,  $R_{\text{eff}}(\infty)$ , derived from single particle Porod measurements assuming spherical scatterers. The MSANS determinations, which are strongly weighted to the larger volume particles [4], indicate that the average pore radius for the distribution within the alumina decreases slightly from  $0.19 \mu\text{m}$  to  $0.17 \mu\text{m}$  in the intermediate sintering stage and increases sharply to  $>0.5 \mu\text{m}$  in the final stage. The Porod determinations, which are weighted to the smaller volume particles, indicate an average pore radius that is slowly increasing during the intermediate stage of sintering and more rapidly increasing during the final stage. Both results indicate a transition in the microstructure morphology between 85 and 95% TD. The quantitative differences arise in part because  $R_{\text{eff}}(0)$  is derived from a measure of the volume fraction of voids in the system and  $R_{\text{eff}}(\infty)$  from a measure of the total surface area in the spaces (or necks) between tetrahedrally positioned particles. Mercury porosimetry measurements (R.A. Page, unpublished results) performed on the samples below 85% TD, where open porosity is expected, agree qualitatively with both sets of SANS results and the average pore radii are quantitatively closer to the  $R_{\text{eff}}(\infty)$  values.

The important result of both the SANS and porosimetry measurements is that the effective pore radius remains relatively constant through the intermediate stage of sintering. This is consistent with intermediate stage sintering models in which topological decay of an interconnected pore network is taking place [7]. Throughout the intermediate stage of sintering, the ratio  $\phi/S_v$ , or volume fraction to surface area per unit volume, is constant [8]. Consequently, the pore channels retain a constant diameter as densification proceeds.

The effective pore radii measured with MSANS correspond to the cross-section of the pore channels. The average length of the pore channels is  $>10 \mu\text{m}$ , which is beyond the range of the MSANS technique. Thus,  $R_{\text{eff}}(0)$

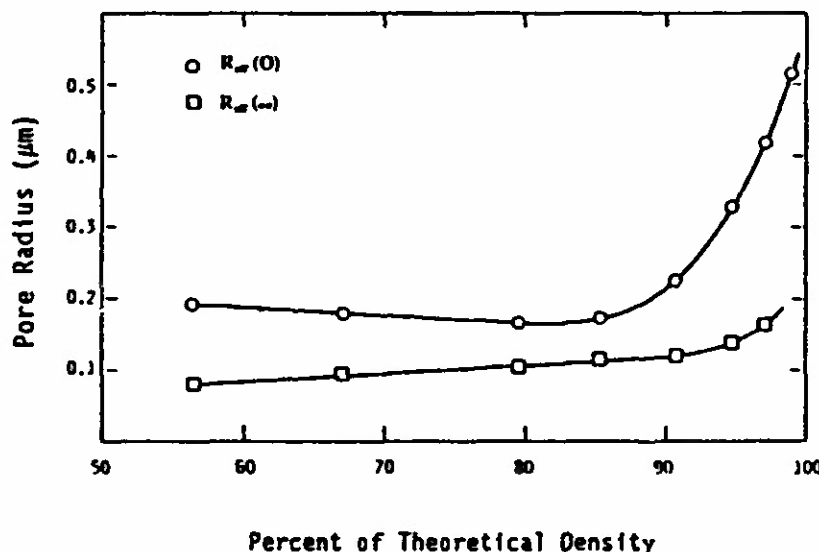


Figure 3. Effective pore radii for the alumina samples as a function of percent theoretical density determined from the MSANS formalism ( $R_{\text{eff}}(0)$ ) and from the single particle Porod measurements ( $R_{\text{eff}}(\infty)$ ).

remains relatively constant as densification proceeds and the pore channel network decays.

Before the channels have disappeared altogether, a transition into the final sintering stage occurs in which the porosity becomes isolated. Pore isolation possibly occurs due to a rupture or "pinching off" of the channels as they can no longer maintain their length while at the same time remaining stable against the increasing sintering force [7]. The isolated pores are more spherical, having diameters which are greater than the cross-sectional diameters of the original channels, yet small enough to be within the MSANS range. As the number of isolated pores increases, the larger dimension makes an increasing contribution to the total scattering, until it finally dominates the MSANS cross-section. Thus,  $R_{\text{eff}}(0)$  increases gradually as the transition from intermediate to final sintering stage begins. Late in the final stage, a more rapid increase is seen as the microstructure becomes dominated by the isolated pores.

#### CONCLUSIONS

The transition from one sintering stage to another in sintered alumina was detected by small angle neutron scattering. The effective radius of the pore size distribution, as measured by both multiple small angle neutron scattering and single particle Porod scattering, remained fairly constant throughout the intermediate stage of sintering, with a rapid increase as densification proceeds beyond 85% of theoretical density. The results are consistent with sintering models which equate the intermediate stage with the decay of the topological network of channels and junction pores in the system. Before complete decay can occur, a transition into the final sintering stage occurs in which the porosity becomes isolated spherical voids.

#### ACKNOWLEDGEMENTS

This work was supported in part by the U.S. Army Research Office under contract no. ARO-MS26123 and in part by the Department of Energy under grant no. DE-FG05-84ER45063.

#### REFERENCES

1. N.F. Berk and K.A. Hardman-Rhyne, J. Appl. Crystallogr. **18**, 467-472 (1985).
2. N.F. Berk and K.A. Hardman-Rhyne, J. Appl. Crystallogr. **21**, 645-651 (1988).
3. R.L. Coble, J. Appl. Phys. **32**, 787-792 (1961) and J. Appl. Phys. **32**, 793-799 (1961).
4. G.G. Long and S. Krueger, J. Appl. Crystallogr. **22**, xxx-xxx (1989).
5. G. Koantor, Treatise on Materials Science and Technology, Vol. 15 (Academic Press, New York, 1979).
6. C.J. Glinka, J.M. Rowe and J.G. LaRock, J. Appl. Crystallogr. **19**, 427-439 (1986).
7. F.N. Rhines and R.T. DeHoff, in Sintering and Heterogeneous Catalysis. Materials Science Research, Vol. 16, edited by G.C. Kuczynski, A.E. Miller and G.A. Sargent (Plenum Press, New York, 1984) pp. 49-61.
8. R.T. DeHoff, R.A. Rummel, H.P. LaBuff and F.N. Rhines, in Modern Developments in Powder Metallurgy, Vol. 1, edited by H.H. Hausner (Plenum Press, New York 1966) pp. 310-331.

## Evolution of the Pore Size Distribution in Final-Stage Sintering of Alumina Measured by Small-Angle X-ray Scattering

Susan Krueger, Gabrielle G. Lang,\* David R. Black, and Dennis Minor

National Institute of Standards and Technology, Gaithersburg, Maryland 20899

Pete R. Jemian\* and G. William Nieman

Department of Materials Science, Northwestern University, Evanston, Illinois 60208

Richard A. Page\*

Southwest Research Institute, San Antonio, Texas 78228

**Small-angle X-ray scattering was used to follow the evolution of the pore size distribution during final-stage sintering of alumina and of alumina doped with 0.25 wt% magnesia. The volume-weighted (Guinier) results indicate that the effective size of the largest pores increases as the body goes from 97% to more than 99% dense. The surface-area-weighted (Porod) results show that the median size of the smallest pores decreases slightly over the same density range. Taken together, these data indicate that the pore size distribution becomes broader as final-stage densification proceeds. This was confirmed by a maximum entropy analysis, which was used to derive pore size distributions directly from the data. Finally, the evolution of the pore size distributions in alumina, with and without sintering aid, were compared. [Key words: alumina, sintering, pore size distribution, X-ray, magnesia.]**

### I. Introduction

THE microstructure evolution of the porous phase during final-stage sintering of alumina and of alumina with 0.25 wt% MgO sintering aid has been studied by means of high-resolution small-angle X-ray scattering (SAXS). The values of the median and the width of the pore size distributions are of special interest in gaining an understanding of the processes which take place as the ceramic body approaches full theoretical density. In particular, the distribution of pore sizes is related to the distribution of the dihedral angles between grains, which are in turn directly related to the driving force for sintering, i.e., the surface free energy.

Earlier studies<sup>1</sup> of the microstructure evolution of alumina as a function of sintering were performed using multiple small-angle neutron scattering. In that work, both the intermediate and final stages of sintering were studied and the results indicated that the effective pore radius is constant during the intermediate stage, independent of the presence of

MgO. During that stage, the value of the effective pore radius was shown to depend on the green body density or, equivalently, on the connectivity in the compact before sintering. When final-stage sintering begins, the open interconnected porosity of the intermediate stage breaks up into isolated porosity, and the effective pore size increases abruptly.<sup>2</sup> It was found that the role of MgO as a sintering aid lies, at least in part, in prolonging the stability of intermediate-stage sintering such that the body achieves greater density before the transition to isolated porosity takes place, leading to a finer-grained finished ceramic in the case of the densified material containing MgO. Contrary to expectation, the measured effective pore radius was never observed to decrease as density increased, even for material that had reached 98% of theoretical density (TD).

The present study was undertaken to measure the evolution of the pore size distributions during late final-stage densification. This kind of information, which can be derived from single-particle scattering, is not generally available from multiple scattering measurements unless the shape of the distribution is known. A high-resolution SAXS camera,<sup>3,4</sup> which can measure sizes between 3 nm and 1 μm, was used to measure samples of alumina and alumina doped with 0.25 wt% MgO with densities ranging from 97% to more than 99% of theoretical. The effective mean pore radius was found to increase as density increased, confirming the earlier multiple neutron scattering results. In addition, it was found that the pore size distribution broadens significantly as density increases. This behavior can be compared to the trends that are observed<sup>5</sup> in the distributions of dihedral angles between grains.

### II. Samples

The samples (13-series and 8-series) were made from Baikowski alumina powder (CR6, 6 m<sup>3</sup>·g<sup>-1</sup>) and slip cast to green densities of approximately 53% of theoretical, where the theoretical density of alumina is 3.985 g·cm<sup>-3</sup>. The slip consisted of 43.5 vol% alumina powder mixed into water, along with 0.5 wt% of a polyelectrolyte dispersant.<sup>6</sup> The suspension was agitated ultrasonically for 15 min and allowed to settle overnight before being poured into molds with Teflon<sup>7</sup> rings on top of plaster-of-paris blocks. The following efforts were made to guarantee that the material was dried slowly to prevent cracking. After 55 min, the molds were removed from the blocks and sealed in a container overnight. The partially dried samples were then removed from the molds and sealed

M. P. Harmer—contributing editor

Manuscript No. 196879. Received March 4, 1991; approved June 12, 1991. Presented at the 93rd Annual Meeting of the American Ceramic Society, Cincinnati, OH, May 2, 1991 (Basic Science Division, Paper No. 156-B-91). Supported by the U.S. Army Research Office under Contract No. MIPR ARO 102-90, by the U.S. Department of Energy under Contract Nos. DE-FG02-86ER45229 and DE-FG03-84ER45063, and by the U.S. Department of Energy, Division of Basic Energy Sciences—Materials Science, under Contract No. W-31-109-ENG-38.

\*Member, American Ceramic Society.

<sup>†</sup>Present address: Materials Science Division, Building 223, Argonne National Laboratory, Argonne, IL 60439.

<sup>1</sup>Darvan C. R. T. Vanderbilt Co., Inc., Norwalk, CT.  
<sup>2</sup>DuPont, Wilmington, DE.

into containers for 2 days, after which the containers were opened to the air for 5 to 7 days. Finally, a series of oven-drying steps were performed: 2 days at 64°C, 1 day at 81°C, 1 day at 102°C, and 1 day at 116°C. At this point a dry, solid green body was achieved. Compacts (D-series) were also prepared by cold-pressing from the same powder doped with 0.25 wt% MgO. Green densities of approximately 51% of theoretical were obtained for these doped samples. Doping was achieved by adding a solution of  $Mg(NO_3)_2$  in distilled water and drying overnight at 200°C. Earlier neutron scattering studies<sup>1</sup> showed that the green body density, rather than the preparation method, determines the sample characteristics.

The samples were heated to 1600°C,<sup>1,2</sup> at which time 90% TD was achieved. With the furnace temperature held constant at 1600°C, samples were removed one at a time to yield examples of sintered microstructure between 97% and more than 99% TD. The characteristics of the three suites of samples are given in Table I. Pore volume fractions were determined volumetrically with an uncertainty of 0.3%. Samples 13-7, 13-8, and D-6 were taken from samples measured earlier by neutron scattering.<sup>1,2</sup> The D-7A sample was obtained by further sintering a piece of the D-7 sample to 99.7% TD. The samples for the X-ray studies were cut out of the larger samples using a standard 3-mm-diameter electron microscopy die and then polished to thicknesses between 150 and 200  $\mu m$ .

### III. Experimental Procedure

#### (1) SAXS Instrument and Measurements

The small-angle X-ray scattering measurements were made by means of a modified Bonse-Hart-type double-crystal diffractometer<sup>3</sup> on the X23A, NIST Materials Science beamline at the National Synchrotron Light Source, Brookhaven National Laboratory. The double-crystal instrument offers high angular resolution at the smallest scattering angles where the scattering from large microstructure is to be found, and it covers the entire relevant size range for the alumina samples.

A diagram of the experiment is shown in Fig. 1. The energy of the incident photons is chosen using a monochromator consisting of two Ge(111) crystals. The size of the X-ray beam is defined by slits at the monochromator exit. Since the X-ray beam is nearly parallel, the slits are adjusted to maximize the coverage on each sample. The incident photon intensity is monitored by means of a combination ionization-chamber/helium-transport tube after the slits and before the sample position. Samples were placed on kapton tape and suspended from rings which were supported at the sample position by means of two fixed pins. The scattered photons were analyzed by two additional Ge(111) crystals, mounted so that they rotate as a monolith about the center of the surface of the first crystal, and were detected by a 5.5-mm-diameter photodiode detector.<sup>4</sup>

Small-angle scattering measurements were performed on the alumina samples using 11-keV photons. Each sample was aligned individually in the X-ray beam and the beam

definition slits were adjusted to maximize the coverage in each case. After the small-angle scattering from the sample was measured, the empty beam (with no sample in place) was measured before aligning the next sample. Thus, each sample measurement is paired with a corresponding empty beam measurement.

#### (2) SAXS Data and Analysis

The raw data of photon counts vs analyzer crystal angle were reduced to SAXS intensity vs scattering vector  $q = 4\pi \sin(\theta)/\lambda$ , where  $\theta$  is one-half of the scattering angle and  $\lambda$  is the photon wavelength. The intensity was placed on an absolute scale by a primary calibration technique.<sup>5</sup> Since the double-crystal instrument involves slit collimation, it was necessary to perform a geometrical correction which was made using the desmeared algorithm of Lake.<sup>7</sup> The desmeared intensities,  $I(q)$ , for each of the three suites of samples are plotted on a  $\ln(I(q))$  vs  $q^2$  scale in Fig. 2. Note that, in each case, the scattering from the most dense samples has the steepest slope at small  $q$  values while the least dense samples show the least curvature in the same  $q$  range. Such curvature is characteristic of samples which contain a distribution of sizes of scatterers. The slope of the curves at small  $q$  is determined by the size of the largest pores in the size distribution. Since the steepest slopes are associated with the most dense samples, the maximum pore size continues to increase as the material approaches full theoretical density.

Since the alumina samples do not contain a monodisperse pore size, a single radius of gyration could not be derived from a conventional Guinier<sup>6</sup> analysis in the small- $q$  region. However, for the purpose of comparing samples, fits to the desmeared data were made in the same limited range  $5 \times 10^{-3} \leq q \leq 6.5 \times 10^{-3} \text{ nm}^{-1}$  to the Guinier equation

$$I(q) = I(0) \exp(-q \cdot R_g^2/3) \quad (1)$$

where  $R_g$  is the radius of gyration of the larger particles and  $I(0)$  is the extrapolated scattering intensity at  $q = 0$  from the range of scattering vector values above.

The desmeared scattered intensity beyond  $q \sim 0.03 \text{ nm}^{-1}$  follows the standard Porod law<sup>8</sup> which can be written

$$I(q) = Pq^{-4} + B \quad (2)$$

where  $P$  is Porod's constant and  $B$  is a background term. Both  $P$  and  $B$  are obtained from linear least-squares fits to  $I(q)^{-1}$  vs  $q^4$  plots for each sample. The total scattering surface area per unit volume,  $S/V$ , is determined directly from  $P$  since

$$P = 2\pi(\Delta\rho)^2 S/V \quad (3)$$

The contrast,  $\Delta\rho$ , is the difference in X-ray scattering length density between the particle matrix and the pores. For the alumina samples,  $\Delta\rho$  is equal to  $32.6 \times 10^{10} \text{ cm}^{-2}$ . An average pore radius,  $R_p$ , can be calculated from  $S/V$  if the pore shape is known. After the background term is subtracted from  $I(q)$ , the scattered intensity curves, plotted on a  $\log(I(q))$  vs  $\log(q)$  scale, exhibit a slope of -4. A Porod plot from sample 13-8,

Table I. Alumina Samples

Sample	Pore volume fraction (%) <sup>a</sup>	Green density (%TD)	Time at 1600°C (min)	Sample density (%TD)	Sample density ( $\text{g} \cdot \text{cm}^{-3}$ )
Undoped alumina					
13-7	3.0	53.0	30	97.0	3.865
13-8	1.0	52.9	300	99.0	3.945
8-10	2.3	52.8	30	97.7	3.893
8-8	1.4	52.9	120	98.6	3.930
8-14	0.7	52.9	300	99.3	3.957
MgO-doped Alumina					
D-6	2.5	50.7	7	97.5	3.885
D-7	1.0	51.0	36	99.0	3.945
D-7A	0.3	51.0	180	99.7	3.973

<sup>a</sup>The uncertainty on all pore volume fraction values is  $\pm 0.3$ .

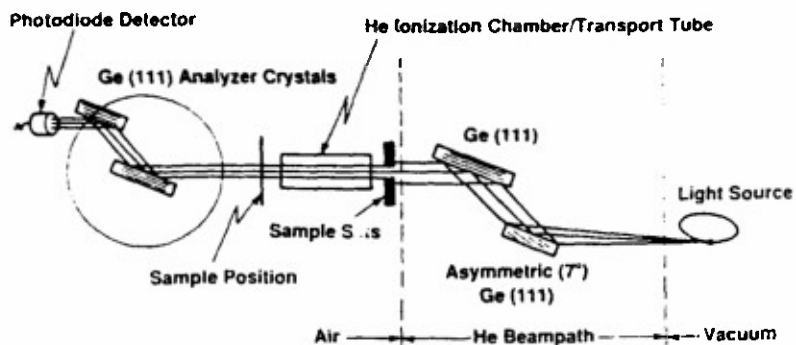


Fig. 1. High-resolution small-angle X-ray scattering instrument.

which is representative of Porod scattering from all of the samples, is shown in Fig. 3. The corresponding fitted slope is  $-4.02 \pm 0.06$  in the range  $0.03 \leq q \leq 0.11 \text{ nm}^{-1}$ .

The radius of gyration obtained from Eq. (1) is a volume-derived parameter and thus is weighted to the larger pores in the size distribution while the Porod radius is a surface-area-derived parameter and is weighted toward the smaller pores.

Thus, the two sets of results taken together are a qualitative measure of the width of the pore size distribution for each sample. To obtain a quantitative description of the distribution of pore sizes, the desmeared SAXS intensities were analyzed for a volume-weighted distribution  $(\Delta\rho)^2 V(D)$ , where  $V(D) dD$  is the volume fraction of pores with diameters between  $D$  and  $D + dD$ . The size distributions were derived

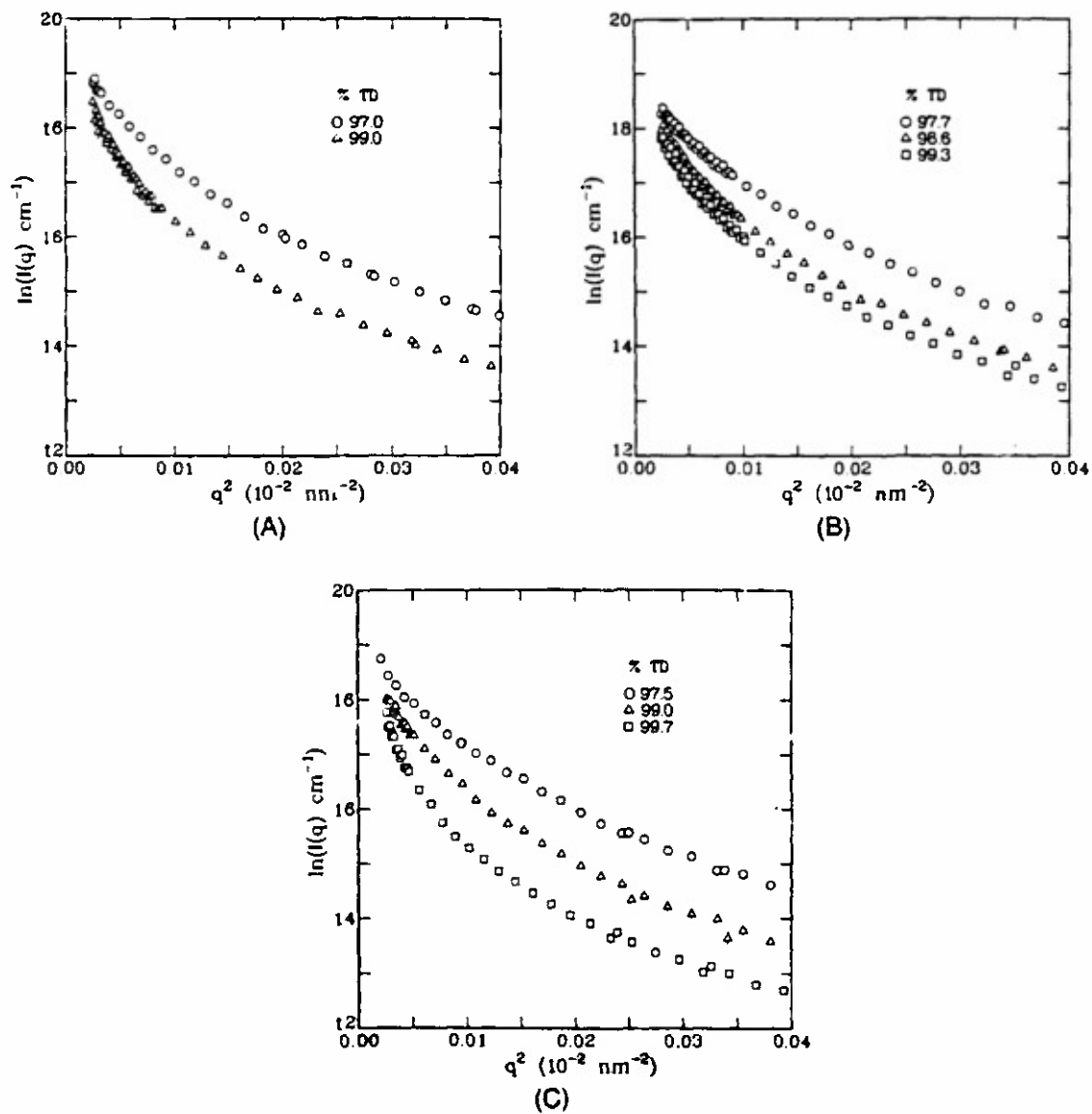


Fig. 2.  $\ln(I)$  vs  $q^2$  (Guinier) plots of desmeared SAXS intensities for the undoped alumina samples: (A) 13-series and (B) 8-series, and the  $\text{MgO}$ -doped alumina samples, (C) D-series.

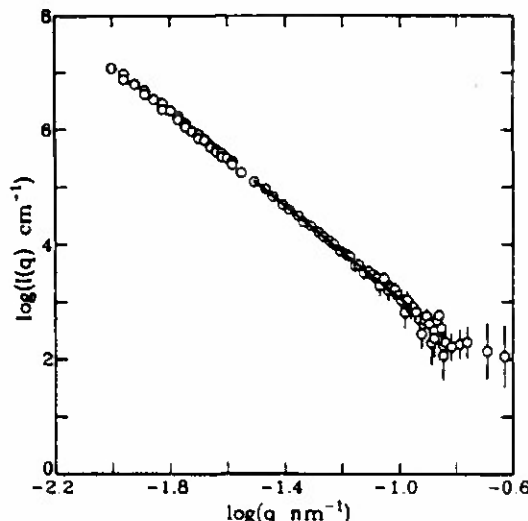


Fig. 3.  $\log(I/q)$  vs  $\log(q)$  (Porod) plot of the desmeared SAXS intensity for sample 13-8, which is a typical example of Porod scattering from each of the alumina samples studied. The solid line has a fitted slope of  $-4.02 \pm 0.06$ .

using a maximum entropy technique<sup>10</sup> for spherical scatterers implemented in the program MAXE obtained from the UKAEA Harwell Laboratory.

The maximum entropy algorithm has been successfully applied to a real system in the study of particle size distributions as a function of starting chemistry in precursor porous silica samples.<sup>11</sup> In this earlier work,<sup>11</sup> it had been emphasized that it is important to apply the maximum entropy method to scattering data encompassing a  $q$  range sufficient to cover the entire size range of the pores in the sample. Otherwise, the resultant curve fit will not accurately represent the true pore size distribution. The prior assumption used in the maximum entropy method is that all particle dimensions are equally probable. Hence all features in the calculated distributions are only produced by corresponding statistically significant features in the scattering data.

One measure of the integrity of the data inversion is a comparison of the pore volume fraction,  $\phi$ , calculated from maximum entropy with the volume fraction determined volumetrically. Another measure of the integrity of the data is a calculation of the invariant<sup>12</sup> of the scattered intensity. The invariant, often represented as  $Q$ , can be written as

$$Q = \int_0^\infty I(q)q^2 dq \quad (4)$$

When  $I(q)$  is measured on an absolute scale, Eq. (4) can be rewritten in terms of the scattering volume fraction such that

$$Q = 2\pi^2(\Delta\rho)^2\phi \quad (5)$$

Note that the shape of the pore size distribution, or equivalently, the shape of the scattered intensity curve, does not enter into the calculation of  $Q$ . Whatever the shape of  $I(q)$  vs  $q$  for a given value of  $\phi$ , the value of the invariant does not change, provided that the data are sufficient to encompass all pore sizes in the distribution. Thus, by integrating  $I(q) \cdot q^2$  over  $q$ , the volume fraction can be calculated directly from the data and compared to that measured volumetrically.

### (3) SEM Sample Preparation and Measurements

In preparation for scanning electron microscopy (SEM) measurements, the surfaces of the specimens were ground with successively finer SiC grit and given a final polish with 1-nm diamond paste. To improve the visibility of surface features, the samples were thermally etched by heating in air at 1500°C for 15 min and then removed at temperature and allowed to cool in air. The samples were viewed in the scanning electron microscope at both 12- and 24-kV accelerating

Table II. SAXS Guinier Results\*

Sample	Pore volume fraction (%)	$R_g$ ( $\mu\text{m}$ )'
<b>Undoped alumina</b>		
13-7	3.0	$0.30 \pm 0.02$
13-8	1.0	$0.37 \pm 0.02$
8-10	2.3	$0.26 \pm 0.01$
8-8	1.4	$0.30 \pm 0.02$
8-14	0.7	$0.31 \pm 0.03$
<b>Doped alumina</b>		
D-6	2.5	$0.31 \pm 0.01$
D-7	1.0	$0.30 \pm 0.01$
D-7A	0.3	$0.39 \pm 0.02$

\*Guinier fits were always made in the range  $5 \times 10^{-3} \leq q \leq 6.5 \times 10^{-3} \text{ nm}^{-1}$ . 'Radius of gyration.

potential and at 0° and 25° tilt. Magnification was checked with NIST SRM 484 (s/n JY-43-cc).

## IV. Experimental Results

### (1) SAXS Results

Values for the radius of gyration,  $R_g$ , obtained from a Guinier analysis in the data range  $5 \times 10^{-3} \leq q \leq 6.5 \times 10^{-3} \text{ nm}^{-1}$  are shown in Table II. These results, while weighted toward the larger pores in the size distribution, are not taken to represent the maximum pore size since the curvature of the data at the smallest  $q$  values measured is still increasing (see Fig. 2), which indicates that still larger pore sizes may be present. The Guinier analysis is generally valid<sup>9</sup> when the  $q$  range used is centered about  $qR_g \leq 1.2$ . In this case,  $qR_g \sim 1.5$  at the smallest  $q$  value measured. Therefore, the  $q$  range accessible with the high-resolution SAXS instrument, while adequate to detect the largest pore sizes, is not sufficient to account quantitatively for all of the large pores in the samples. However, these results can be used to place a lower limit on the maximum pore sizes present in the samples and, since they were obtained in the same  $q$  range for each sample, they can be meaningfully compared.

The  $R_g$  values in Table II show an increase in pore size with increasing sample density, independent of the presence of MgO sintering aid. This is illustrated when the results for all three suites of samples are plotted together, as shown in Fig. 4. The trend observed here confirms and extends the

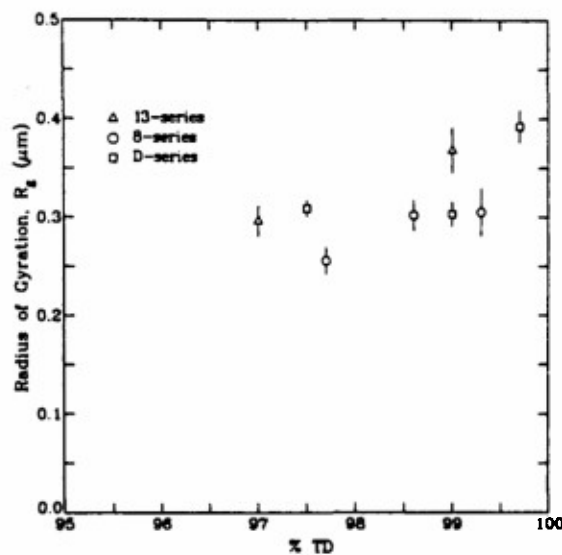


Fig. 4. Plot of pore  $R_g$  (radius of gyration) values for all samples, obtained from a Guinier analysis, as a function of sample density. In all cases, fits were made in the data range  $5 \times 10^{-3} \leq q \leq 6.5 \times 10^{-3} \text{ nm}^{-1}$ .

Table III. SAXS Porod Results

Sample	Pore volume fraction (%) <sup>a</sup>	$q_{\min}$ (nm <sup>-1</sup> )	$q_{\max}$ (nm <sup>-1</sup> )	$P \times 10^{-3}$ cm <sup>-1</sup>	$S/V \times 10^3$ cm <sup>-1</sup>	$R_p$ (μm) <sup>b</sup>
<b>Undoped alumina</b>						
13-7	3.0	0.03	0.11	$31.49 \pm 0.04$	$4.716 \pm 0.006$	$0.191 \pm 0.019$
13-8	1.0	0.03	0.11	$11.67 \pm 0.02$	$1.748 \pm 0.003$	$0.172 \pm 0.051$
8-10	2.3	0.03	0.11	$25.38 \pm 0.02$	$3.800 \pm 0.003$	$0.182 \pm 0.023$
8-8	1.4	0.03	0.11	$12.05 \pm 0.02$	$1.719 \pm 0.003$	$0.233 \pm 0.053$
8-14	0.7	0.03	0.11	$8.38 \pm 0.01$	$1.254 \pm 0.001$	$0.167 \pm 0.072$
<b>Doped alumina</b>						
D-6	2.5	0.03	0.13	$25.87 \pm 0.03$	$3.874 \pm 0.005$	$0.194 \pm 0.023$
D-7	1.0	0.03	0.13	$11.06 \pm 0.02$	$1.656 \pm 0.003$	$0.180 \pm 0.055$
D-7A	0.3	0.03	0.13	$4.89 \pm 0.02$	$0.732 \pm 0.003$	$0.123 \pm 0.123$

<sup>a</sup>The uncertainty on all pore volume fraction values is  $\pm 0.3$ . <sup>b</sup>Porod constant. <sup>c</sup>Normalized surface area. <sup>d</sup>Porod radius. Spherical scatterers are assumed.

trends observed in earlier neutron scattering studies<sup>1,2</sup> where the effective pore radius was observed to increase monotonically with increasing sample density during final-stage sintering. In addition, it was shown in one of these studies<sup>1</sup> that the effective radius of pores in the doped sample was consistently smaller than that of pores in undoped samples at the same density. Quantitatively, the pore sizes in the neutron scattering studies are somewhat larger than reported here. This occurs because the pore volume fractions used in the neutron scattering studies were derived directly from the data fitting procedure and are somewhat lower than the volumetrically determined values used in this work. In addition, the multiple small-angle neutron scattering technique accounts for the largest pores in the sample, which serves to increase the effective pore radius derived from those studies.<sup>1,2</sup>

Values for the pore radius obtained from a Porod analysis of the SAXS data and assuming a spherical pore shape are shown in Table III, along with the derived Porod constant,  $P$ , and the normalized surface area per unit volume,  $S/V$ . The largest possible linear region in the  $\log (J) \text{ vs } \log (q)$  curve beyond  $q = 0.03 \text{ nm}^{-1}$  was fit in each case, as given in the  $q_{\min}$  and  $q_{\max}$  columns of Table III. Figure 5 shows the Porod results for all three suites of samples. The large error bars for the samples at the highest densities are a direct result of the 0.3% uncertainty on the pore volume fraction values. Contrary to the behavior of the  $R_p$  values, the  $R_p$  values decrease slightly with increasing sample density, again independent of the presence of MgO in the sample. Since the  $R_p$  values are weighted to the larger pore sizes in the distribution and the

$R_p$  values are weighted to the smaller pore sizes, the behavior of the radii in Figs. 4 and 5 indicates that the pore size distribution broadens with increasing sample density.

The volume size distributions  $V(D)$ , derived for each sample using the maximum entropy algorithm, are plotted versus diameter,  $D$ , for each suite of samples in Fig. 6. The sample densities which have been used to identify the curves are those which had been determined volumetrically. The large peaks in the size distributions represent the centroids of the distributions, while the smaller ripples may be due to mathematical artifacts.<sup>13-15</sup> Therefore, smoothed lines have been drawn through the points for clarity. The volume-weighted mean pore radius,  $R_v$ , calculated from the resultant size distribution, is shown for each sample in Table IV. These values agree quantitatively with the average pore radii determined from the earlier neutron scattering studies,<sup>1,2</sup> provided that the volumetrically determined values for the pore volume fraction are used in all cases.

The broadening of the size distributions as a function of densification can be seen in Fig. 6 and the increase in the mean pore radius can be seen in Table IV. This table also includes the values of the standard deviation of the mean pore radius which is seen to increase as sample density increases.

## (2) SEM Results

Scanning electron micrographs for undoped samples 13-7 and 13-8, and doped samples D-6 and D-7, are presented in Fig. 7. The grain boundaries and pores can clearly be seen. While some of the pores are larger than 1 μm, most are smaller. In addition, most of the pores reside on grain boundaries while others are trapped inside large grains. The average grain size in the undoped samples (13-7 and 13-8) increases dramatically, along with an increase in pore size, as the sample goes from 97% to >99% TD. A similar increase in grain and pore size is seen in the doped samples (D-6 and D-7). A comparison of the micrographs of Fig. 7 with the pore size distributions in Fig. 6 shows that the SEM results are consistent with the SAXS results derived using the maximum entropy technique. Note that the region of sensitivity for the SEM studies differs from that of the SAXS studies. The SEM technique measures surface features. Therefore, it is well-suited for studying the largest pores in the samples since the necessary polishing and etching processes tend to remove the small pores from the sample surfaces. On the other hand, the SAXS technique measures bulk samples so it is sensitive to the smaller pores as well. Figure 6 shows that the majority of the pores in the samples fall below the size range readily accessible with SEM.

The most striking feature in the comparison between the doped samples and the undoped samples is that the average grain size in the doped samples is markedly smaller than that of grains in the undoped samples of approximately the same density. Since pore growth is associated with grain growth, this would imply that the average pore size is also smaller in the latest stages of sintering for the MgO-doped samples.

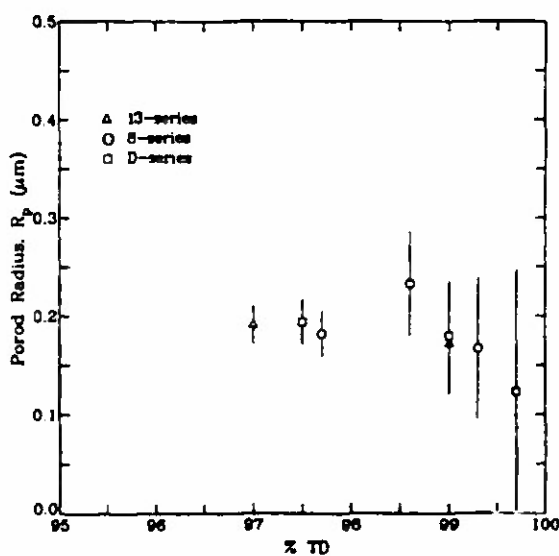


Fig. 5. Plot of pore  $R_p$  (Porod radius) values for all samples, obtained from a Porod analysis and assuming a spherical pore shape, as a function of samples density. Fits were made in the largest possible linear data range beyond  $q = 0.03 \text{ nm}^{-1}$ .

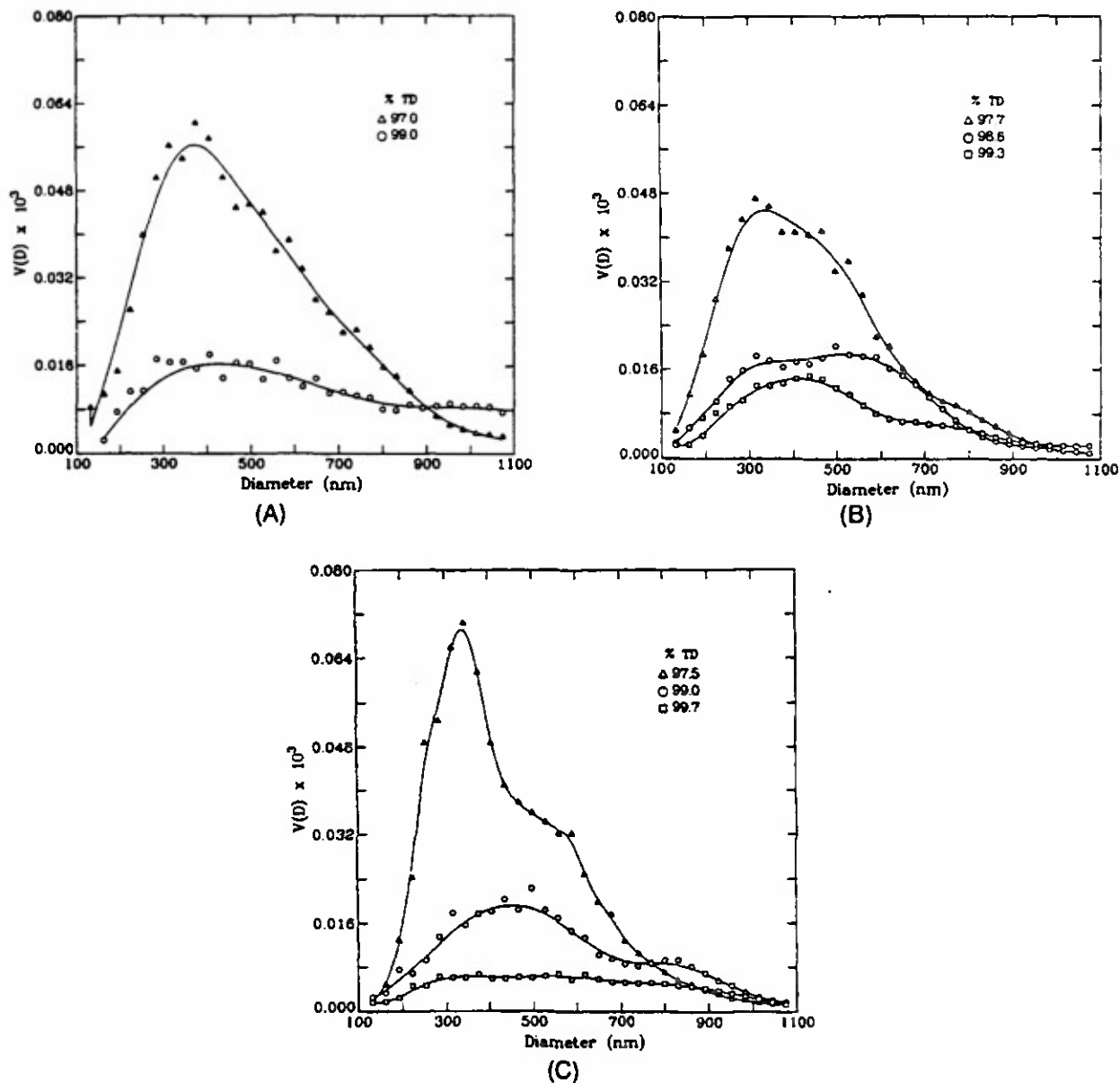


Fig. 6. Volume size distributions  $V(D)$ , derived using the maximum entropy procedure, plotted as a function of diameter,  $D$ , for the undoped alumina samples: (A) 13-series and (B) 8-series, and the MgO-doped alumina samples, (C) D-series. For clarity, smoothed lines have been drawn through the data points.

## V. Discussion

The motivation for studying the pore evolution during the late stages of sintering of undoped and doped alumina with high-resolution SAXS was the result of the earlier neutron scattering study<sup>1</sup> of the same material which suggested that

the effective pore radius continues to increase with increasing sample density, even when densities reach 98% TD. The neutron scattering results for the undoped 13- and doped D-series samples are reproduced in Fig. 8, where the effective pore radius is plotted versus %TD. This figure shows that the mean pore radius during intermediate-stage sintering is determined by the green body density or, in other words, by the original connectivity in the green state. The transition from intermediate stage (where the porosity consists mainly of interconnected channels) to final stage (where the porosity becomes isolated) apparently occurs between 86% and 92% TD, where the effective radius begins to increase rapidly with increasing sample density. This transition occurs at a greater density in the case of the MgO-doped sample, suggesting that the role of MgO as a sintering aid lies, at least in part, in extending the stable intermediate sintering stage, thus allowing the body to achieve greater density before final-stage sintering begins.

Although there are large uncertainties in the radii of the denser final-stage samples, the effective radius of the undoped alumina sample is consistently larger than that for the doped sample at the same density. This effect might be even more pronounced if the green densities had been identical. Ex-

Table IV. SAXS Maximum Entropy Results

Sample	Pore volume fraction (%)	$R_e$ ( $\mu\text{m}$ ) <sup>a</sup>
<b>Undoped alumina</b>		
13-7	3.0	0.245 (0.113)
13-8	1.0	0.336 (0.172)
8-10	2.3	0.225 (0.105)
8-8	1.4	0.236 (0.114)
8-14	0.7	0.280 (0.161)
<b>Doped alumina</b>		
D-6	2.5	0.225 (0.096)
D-7	1.0	0.272 (0.119)
D-7A	0.3	0.292 (0.130)

<sup>a</sup>Volume-weighted mean radius. Standard deviations of the mean radius are given in parentheses.

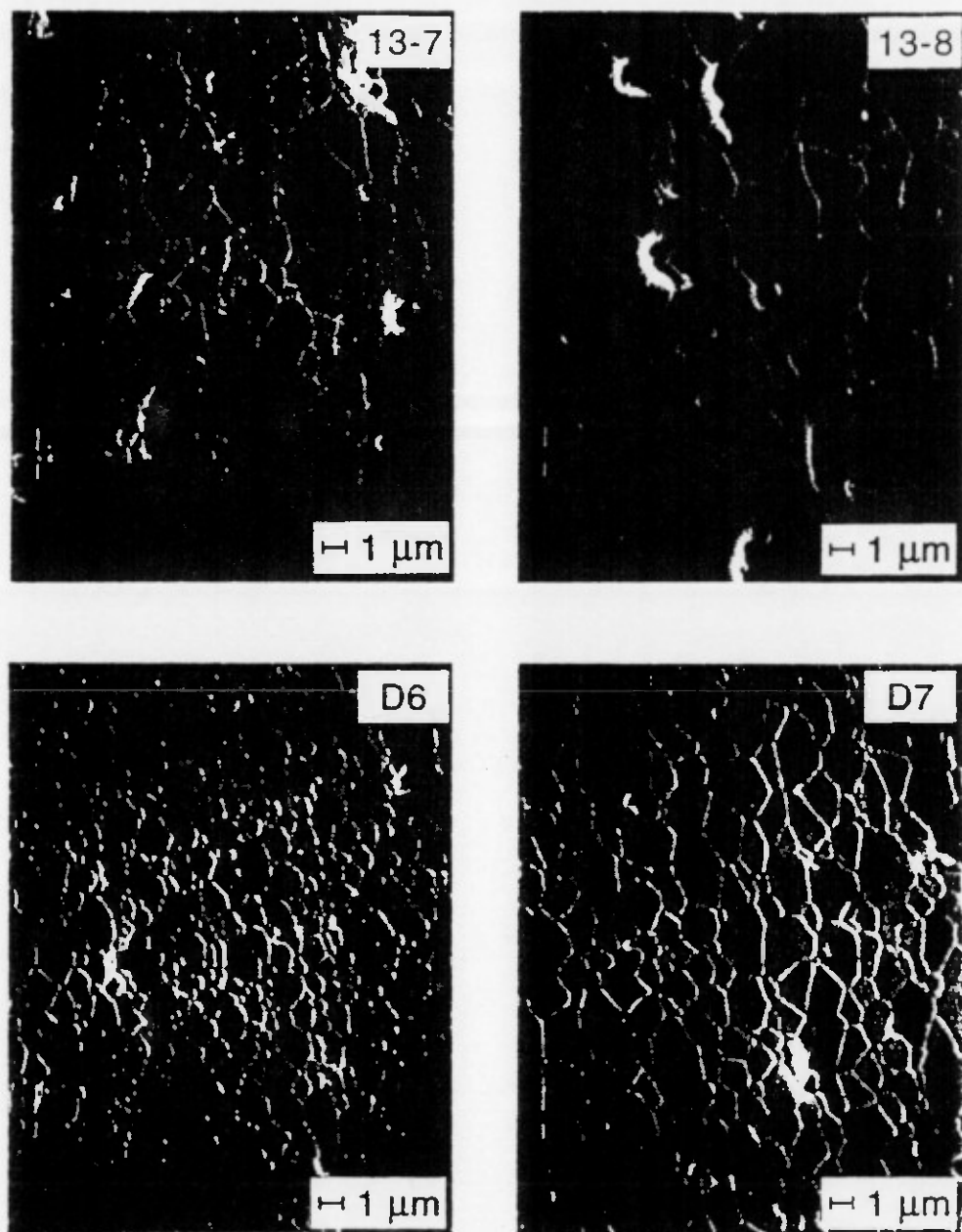


**Fig. 7.** Scanning electron micrographs of undoped alumina samples 13-7 (97.0% TD), 13-8 (99.0% TD) and of MgO-doped samples D-6 (97.5% TD) and D-7 (99.0% TD).

tending intermediate-stage sintering leads to a finer-grained ceramic in the case of alumina containing MgO since it does not undergo the same degree of exaggerated grain and pore growth as the undoped material. The high-resolution SAXS experiments were performed in order to measure the final-stage samples with higher precision than is possible with the neutron scattering technique and to extend the study of the evolution of the pore size distribution to sample densities greater than 99% TD.

The SAXS Guinier results (Table II and Fig. 4) confirmed the neutron scattering results and demonstrated that the average pore radius continues to increase in the final stage of sintering in both the undoped and doped alumina. Furthermore, the trend continues even as densities reach more than 99% TD. When these results are combined with those obtained from the Porod analysis (Table III and Fig. 5), it is evident that the pore size distribution broadens with sample density in both cases.

The more quantitative representation of the pore volume distributions, obtained by the maximum entropy technique

(Fig. 6), can be directly related to the grain size distributions observed in the SEM micrographs (Fig. 7). While the grain size distribution can be seen directly from the micrographs, the SAXS measurements are used to obtain a statistically significant description of the pore size distribution. The average pore diameters determined from the pore size distribution (Table IV) quantitatively confirm the neutron scattering results provided that the volumetric densities are used in both cases.<sup>1</sup>

Earlier studies<sup>5</sup> in which the dihedral angles between grains were measured and related to the grain size distributions in ~99% dense alumina and alumina with 0.25 wt% MgO demonstrated that the dihedral angle size distribution, and thus the grain size distribution, were narrower for the MgO-doped sample. However, the median value of the dihedral angle remained the same for both undoped and MgO-doped samples. This behavior can be seen in the micrographs for the ~97% TD samples as well as the ~99% TD samples, although the micrographs indicate that the average grain size is larger for the undoped cases. The narrowing of the grain

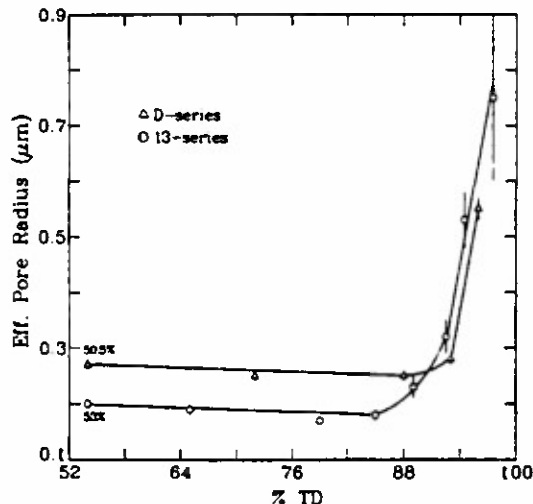


Fig. 8. Results from earlier multiple small-angle neutron scattering studies<sup>1</sup> showing the effective pore radius as a function of sample density for the undoped (13-series) and MgO-doped (D-series) samples.

size distribution implies that the ranges of the surface energy and/or the grain boundary energy become narrower with addition of MgO.

A similar trend is expected for the pore size distribution at the same densities. The derived volume distributions for the ~99% TD samples (13-8 and D-7) are plotted together in Fig. 9. The figure suggests that the size distribution is indeed narrower for the MgO-doped sample and that the doped sample contains a smaller volume of pores greater than ~800 nm in diameter. Table IV supports this conclusion, showing that both the mean pore radius and its standard deviation are smaller for the sample containing MgO. This effect may be masked somewhat since the green density of the MgO-doped sample was higher than that of the undoped sample, meaning that the average pore radius of the MgO-doped sample was larger from the beginning. If both samples had started out with identical green densities, the differences observed here in mean pore radius and in the width of the size distributions could possibly be larger.

The pore volume fractions,  $\phi$ , calculated from the maximum entropy procedure and from the invariant, where the

integral in Eq. (4) is taken from  $q = 0$  to  $q_{max}$ , are compared to the volumetric determination in Table V. The value of  $\phi$  determined from maximum entropy is, in some cases, lower than the volumetric determination, which has an uncertainty of  $\pm 0.003$ . Furthermore, the value determined from the invariant generally falls above that determined from maximum entropy. In the maximum entropy procedure, an analytical calculation of the volume fraction based on the known scattering function for spherical scatterers is made. On the other hand, the integral used in calculating the invariant begins at  $q = 0$ . Since no data are available at values below  $q = 5 \times 10^{-3} \text{ nm}^{-1}$ ,  $I(q)$  is extrapolated to  $q = 0$  using the Guinier approximation represented by Eq. (1).

Although both the maximum entropy and the invariant determinations of  $\phi$  yield volume fractions that agree well with those measured volumetrically, it is still possible that a small number of pores in each sample are too large to be measured, even with the high-resolution SAXS instrument. This was already suggested from the Guinier plots (Fig. 2), which display noticeable curvature at the smallest measured  $q$  values. In addition, the  $R_g$  values obtained from the Guinier analyses (Table II) indicate that  $qR_g \sim 1.5$  at  $q = 5 \times 10^{-3} \text{ nm}^{-1}$ , whereas the  $q$  range should be centered upon  $qR_g \leq 1.2$ .<sup>9</sup> Thus, those pores with sizes that correspond to the extremes of the  $q$  range may be underrepresented in the pore size distributions. Further evidence of the existence of larger pores is provided by the SEM micrographs in which a few pores with diameters larger than 1  $\mu\text{m}$  can be seen. Except that the pores at the extremes of the  $q$  range may not be completely included, the small number of such large pores will not significantly affect the derived pore size distributions.

## VI. Concluding Remarks

The evolution of the pore size distribution during final-stage sintering of alumina and of alumina doped with 0.25 wt% MgO was followed using high-resolution small-angle X-ray scattering. The pore radius of gyration, obtained from a Guinier<sup>8</sup> analysis, was observed to increase from ~0.3 to ~0.4  $\mu\text{m}$ , independent of the presence of MgO sintering aid, as the sample density increased from ~97% to >99% of theoretical density (Table II). In contrast, the pore radius derived from a Porod<sup>9</sup> analysis and assuming a spherical pore shape was observed to decrease from ~0.2 to ~0.1  $\mu\text{m}$  over the same range of sample densities (Table III). Taken together, these results indicate qualitatively that the pore size distribution broadens with increasing sample density. In addition, pore volume distributions, which provide a quantitative description of the pore size distribution, were derived for each sample using a maximum entropy analysis.<sup>10</sup> Both the mean pore radius and its standard deviation, obtained directly from the pore size distribution, were found to increase with increasing sample density. The trends observed here confirm earlier multiple small-angle neutron scattering studies<sup>1,2</sup> which demonstrated that the average pore radius continues to increase in the final stage of sintering in both the undoped and the doped samples and suggested that this trend continues even as densities reach more than 99% of theoretical. Furthermore, the average pore radii determined from the SAXS analyses agreed quantitatively with those determined in the neutron scattering experiment, provided that the volumetrically determined sample densities are used in both cases.

Scanning electron micrographs of both undoped (13-7 and 13-8) and MgO-doped (D-6 and D-7) samples show that the majority of pores are smaller than 1  $\mu\text{m}$ , supporting the scattering results. The average grain size as well as the average pore size increases for both doped and undoped samples as the density increases from 97% to >99% of theoretical. For a given sample density, the average grain size is markedly smaller, and the grain size distribution is narrower, in the

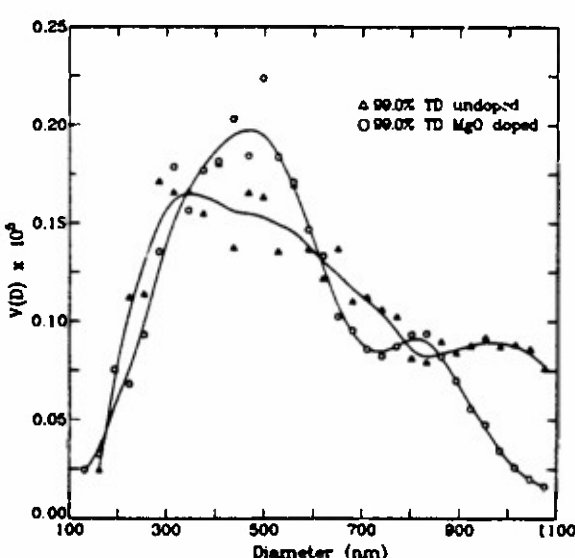


Fig. 9. Maximum entropy-derived volume distributions  $V(D)$  vs diameter,  $D$ , plots for the ~99% dense samples (A) 13-8 (undoped) and (B) D-7 (MgO doped).

Table V. Scattering Volume Fractions

Sample	Volumetric measurement	Volume fraction*	
		Maximum entropy determination	Invariant determination
<b>Undoped alumina</b>			
13-7	0.03	0.027	0.029
13-8	0.01	0.013	0.012
8-10	0.023	0.02	0.025
8-8	0.014	0.011	0.015
8-14	0.007	0.008	0.010
<b>Doped alumina</b>			
D-6	0.025	0.023	0.023
D-7	0.01	0.011	0.011
D-7A	0.003	0.005	0.007

\*The uncertainty in all pore volume fraction values is  $\pm 0.003$ .

MgO-doped samples. This confirms earlier studies<sup>5</sup> which showed that the distribution of dihedral angles between grains, and thus the grain size distribution, in ~99% dense MgO-doped alumina is narrower than in undoped alumina at the same density.

**Acknowledgment:** We are grateful to UKAEA Harwell for the MAXE software used to perform the maximum entropy data analysis.

## References

- G. G. Long, S. Krueger, and R. A. Page, "The Effect of Green Density and the Role of Magnesium Oxide Additive on the Densification of Alumina Measured by Small-Angle Neutron Scattering," *J. Am. Ceram. Soc.*, **74** [7] 1578–84 (1991).
- S. Krueger, G. G. Long, and R. A. Page, "Characterization of the Densification of Alumina by Multiple Small-Angle Neutron Scattering," *Acta Crystallogr. A*, **47**, 282–90 (1991).
- G. G. Long, P. R. Jemian, J. R. Weertman, D. R. Black, H. E. Burdette, and R. Spal, "High-Resolution Small-Angle X-ray Scattering Camera for Anomalous Scattering," *J. Appl. Crystallogr.*, **24**, 30–37 (1991).
- P. R. Jemian and G. G. Long, "Silicon Photodiode Detector for Small-Angle X-ray Scattering," *J. Appl. Crystallogr.*, **23**, 430–32 (1990).
- C. A. Handwerker, J. M. Dyns, R. M. Cannon, and R. L. Coble, "Dihedral Angles in Magnesia and Alumina: Distributions from Surface Thermal Grooves," *J. Am. Ceram. Soc.*, **73** [5] 1371–77 (1990).
- R. W. Hendricks, "A Unified Theory of Absolute Intensity Measurements in Small-Angle X-ray Scattering," *J. Appl. Crystallogr.*, **5**, 315–24 (1972).
- J. A. Lake, "An Iterative Method of Slit-Correcting Small-Angle X-ray Data," *Acta Crystallogr.*, **23**, 191–94 (1967).
- A. Guinier and G. Fournet, *Small Angle Scattering of X-rays*; p. 25. Wiley, New York, 1955.
- G. Kostorz, *Treasure of Material Science and Technology*, Vol. 15; pp. 227–89. Academic Press, New York, 1979.
- J. A. Porton, G. J. Daniell, and B. D. Rainford, "Particle Size Distributions from SANS Data Using the Maximum Entropy Method," *J. Appl. Crystallogr.*, **21**, 663–68 (1988).
- G. G. Long, S. Krueger, P. R. Jemian, D. R. Black, H. E. Burdette, J. P. Cline, and R. A. Gerhardt, "Small Angle Scattering Determination of the Microstructure of Porous Silica Precursor Bodies," *J. Appl. Crystallogr.*, **23**, 535–44 (1990).
- G. Porod; pp. 17–52 in *Small Angle X-Ray Scattering*. Edited by O. Glatter and O. Kratky. Academic Press, New York; 1982.
- A. Allen; unpublished results, 1989.
- S. F. Gull, "Developments in Maximum Entropy Data Analysis"; pp. 53–71 in *Maximum Entropy and Bayesian Methods*. Edited by J. Skilling. Klever, Dordrecht, Netherlands, 1989.
- R. K. Bryan, "Maximum Entropy Analysis of Oversampled Data Problems," *Eur. Biophys. J.*, **18**, 165–74 (1990). □

## Characterization of the Densification of Alumina by Multiple Small-Angle Neutron Scattering

BY S. KRUEGER AND G. G. LONG

*National Institute of Standards and Technology, Gaithersburg, MD 20899, USA*

AND R. A. PAGE

*Southwest Research Institute, San Antonio, TX 78228, USA*

(Received 15 July 1990; accepted 4 January 1991)

### Abstract

Multiple small-angle neutron scattering was used to follow the evolution of the pore-size distribution in  $\alpha\text{-Al}_2\text{O}_3$  through the intermediate and final stages of sintering. This new technique enables the study of microstructure in the 0.08–10  $\mu\text{m}$  size regime, which is the size range of importance for many materials systems, without needing to increase the resolution of currently available small-angle scattering instruments. The microstructure evolution results indicate a nearly constant effective pore radius for the alumina throughout the intermediate sintering stage, ranging from 0.19  $\mu\text{m}$  at 54% of theoretical density to 0.17  $\mu\text{m}$  at 79% dense. As the alumina densifies further, there is a transition region after which the effective pore radius grows rapidly to  $\geq 0.6 \mu\text{m}$  at 97.5% dense.

### 1. Introduction

Small-angle neutron scattering (SANS) is an important technique for the statistically significant evaluation of bulk microstructural parameters in materials containing dilute concentrations [where 'dilute' is represented by  $\phi/(1-\phi) \sim \phi$  and  $\phi$  is the scattering volume fraction] of scatterers between 10 and 1000  $\text{\AA}$ . However, the relevant structures in many physical systems, such as partially sintered ceramics, cannot readily be studied by SANS since the usual approximations are not valid for the larger sizes and more-dense structures present in these materials. To perform neutron scattering characterization of high technology materials as a function of thermal processing, it has become increasingly important to extend the range of particle-size determinations usually associated with SANS up to  $\sim 10 \mu\text{m}$  and to be able to include the analysis of thicker and less-dilute [ $\phi/(1-\phi) > \phi$ ] systems in which the coherent elastic differential scattering cross section is dominated by multiple scattering. These issues have been successfully addressed by the multiple small-angle neutron-scattering (MSANS) formalism of Berk & Hardman-Rhyne (1985, 1988), which applies when multiple scattering arises solely from the compounding of

single-particle scattering events, meaning that there is no scattering component due to correlations between particles. Berk & Hardman-Rhyne refer to this type of scattering process as 'incoherent multiple scattering'.

The central assumptions of the MSANS formalism are that the observed MSANS intensity is the result of incoherent multiple scattering from a randomly distributed monodisperse population of spheres comprised of material of uniform density (i.e. containing no internal structure) and that the phase shift  $\nu$  that a plane wave undergoes in traversing a particle of radius  $R$  is within the range  $\sim 0.1$  to 2. Effective (volume-weighted average) radii of the scatterers are extracted by measuring the wavelength dependence of the broadening of the scattering curves.

An earlier study of microstructure evolution in porous silica as a function of thermal processing (Long & Krueger, 1989) demonstrated that MSANS and SANS can effectively be used together to cover the full range of relevant microstructure sizes. In this work, MSANS was used to follow the evolution of the pore-size distribution in  $\alpha\text{-Al}_2\text{O}_3$  through the intermediate and final stages of sintering.

Knowledge of the microstructure evolution as a function of thermal processing is important for the development of process models in ceramics. The process models for both the silica (Kingery & Berg, 1955) and alumina (Coble, 1961) systems are comparatively well understood. Whereas porous silica is a glassy system which sinters by means of viscous flow, alumina is a polycrystalline system which sinters by means of volume and surface diffusion. The different sintering mechanisms should give rise to different microstructure evolution. Thus, these well characterized materials can serve as model systems for the new MSANS technique.

### 2. MSANS theory

The interaction of neutrons with matter is characterized by the phase shift  $\nu$  that a plane wave undergoes in traversing a particle of radius  $R$ . This phase shift

determines the shape of the single-particle differential scattering cross section,  $d\Sigma(Q)/d\Omega$ , as a function of the scattering wavevector  $Q$ , where  $|Q| = 2\pi\varepsilon/\lambda$  and  $\varepsilon \ll 1$  is the scattering angle.  $\nu$  depends upon  $\Delta\rho$ , the contrast of the particle or void, relative to the scattering matrix such that

$$\nu = 2\Delta\rho R\lambda, \quad (1)$$

where  $\Delta\rho$  is written as

$$\Delta\rho = \sum_{\text{cell}} (b_i/V) - \rho_{\text{matrix}}. \quad (2)$$

The  $b_i$  are the coherent scattering lengths of the individual nuclei whereas  $\rho_{\text{matrix}}$  is the average scattering-length density of the matrix. Thus, the phase shift is directly dependent upon the material contrast ( $\Delta\rho$ ), the dimension of the scattering particle or void ( $2R$ ) and the neutron wavelength ( $\lambda$ ).

If  $\nu \ll 1$  (the usual SANS diffraction regime), the measured scattered intensity can be described by the Born approximation (Porod, 1951; Weiss, 1951) of scattering theory or the Rayleigh-Gans model (Rayleigh, 1910, 1914; Gans, 1925) of wave optics. For appropriately thin samples, the majority of the incident neutron beam is transmitted through the sample and the remaining neutrons are scattered only once before exiting the sample. The scattered intensity as a function of  $Q$  is independent of neutron wavelength and its shape near  $Q=0$  depends only

on the particle dimensions. Fig. 1(a) represents a typical SANS scattering curve. The scattered intensity around  $Q=0$  cannot be measured directly because it lies in the same region as the transmitted beam, which is  $10^3$  to  $10^7$  times more intense than the scattered beam. Therefore, a beamstop is usually employed to prevent the transmitted beam from reaching and thus damaging the neutron detector. For any particle shape, the particle size can be described by its radius of gyration  $R_g$  or Guinier radius (Kostorz, 1979) which is the same as the radius of gyration in mechanics and is obtained from an analysis of the small- $Q$  portion of the scattered-intensity curve. The range for which the Guinier analysis is valid is defined by  $QR_g \leq \sim 1.2$  (Kostorz, 1979). In addition, the ratio of the total scattering surface area to the volume of the sample in the neutron beam,  $S/V_b$ , can be obtained from an analysis of the large- $Q$  portion of the scattered-intensity curve. In this region, the scattered intensity obeys the  $Q^{-4}$  Porod law (Kostorz, 1979). An equivalent spherical radius can be determined from the total scattering surface area.

At the opposite extreme, when  $\nu \gg 1$  (the multiple refraction regime), every particle scatters and the scattered intensity is derived from geometrical optics (von Nardroff, 1926). The shape of the scattering curve is independent of the particle radius and depends only upon the difference in index of refraction between the scatterers and the matrix which, in turn, depends upon neutron wavelength as  $\lambda^2$ . This regime is not pursued further here.

When  $\nu = 1$  (the MSANS diffraction regime), the scattered intensity cannot be described by either conventional SANS diffraction or by multiple refraction. Scatterers with radii in the  $0.1-10 \mu\text{m}$  range generally undergo phase shifts of the order of 1 for the range of neutron wavelengths usually available for SANS. Since larger particles scatter more intensely than smaller ones, the likelihood of multiple scattering becomes greater (Berk & Hardman-Rhyne, 1988). Furthermore, the incidence of coherent scattering between larger particles is greatly decreased, meaning that the single-particle scattering cross section does not contain a component due to interparticle interference. Thus, in the MSANS diffraction regime, multiple scattering arises solely from the statistical compounding of numerous coherent elastic single-particle scattering events in which interparticle interference does not play a significant role (Berk & Hardman-Rhyne, 1985).

A measure of the amount of incoherent multiple scattering is given by the parameter  $\bar{z}$  (Berk & Hardman-Rhyne, 1988), which is the sample thickness,  $z$ , divided by the statistical neutron mean free path length,  $l$

$$\bar{z} = z/l = 1.5\varphi z(\Delta\rho\lambda)^2 R, \quad (3)$$

where  $\varphi$  is the volume fraction of scatterers.  $\bar{z}$  is

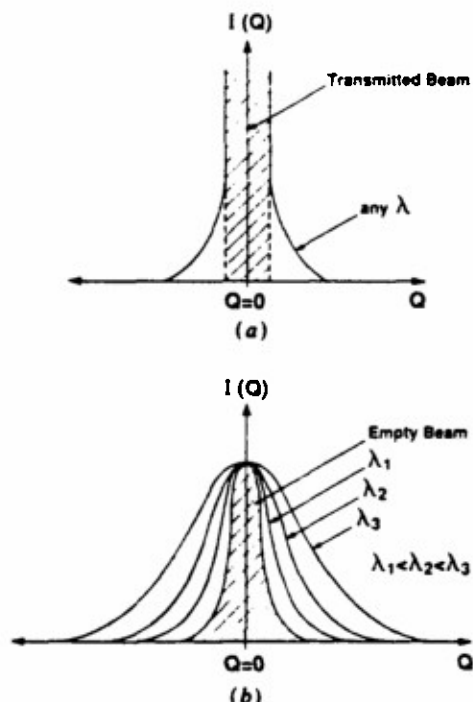


Fig. 1. (a) Representation of an  $I(Q)$  vs  $Q$  scattered-intensity curve arising from conventional small-angle scattering, illustrating its wavelength-independent shape and the transmitted-beam region near  $Q=0$ . (b) Representation of a typical set of  $I(Q)$  vs  $Q$  multiple small-angle scattered-intensity curves from a single sample, illustrating their wavelength-dependent shape and the empty-beam curve.

related to the sample transmission as  $T_s = \exp\{-\bar{z}\}$ . Since  $\Delta\rho$  involves only coherent scattering lengths,  $\bar{z}$  can only be calculated from the measured sample transmission after correcting for absorption and incoherent single-particle scattering, where applicable. A value of  $\bar{z} = 0.0$  means that there is no multiple scattering. In practice, the data from SANS samples of finite thickness such that  $0 < \bar{z} \leq 1$  always contain some multiple scattering which is either negligibly small or treated as a small correction to the single-particle scattering. In MSANS measurements, the amount of multiple scattering is copious and  $\bar{z}$  typically ranges from 10 to 400.

In the region of validity of MSANS, the intensity of the transmitted beam is immeasurably small and the width of the scattered intensity curve near  $Q = 0$  is broadened far beyond the broadening due to instrumental resolution. The amount of beam broadening is dependent upon the incident neutron wavelength as illustrated in Fig. 1(b) where representative MSANS curves are shown for different wavelengths incident on a single sample. The intensities have been normalized such that  $I(0) = 1.0$ . In each case, the scattered intensities,  $I(Q)$ , have a curvature,  $r_c$ , near  $Q = 0$  and can be approximately described as a Gaussian with a width proportional to  $\lambda^2$ . For large  $Q$ , there is a crossover to single-scattering Porod behavior (Berk & Hardman-Rhyne, 1985), where the cross section is proportional to  $Q^{-4}$ .

It is evident from (1) and (3) that the contribution of incoherent multiple scattering to the total cross section depends upon a balance of the parameters which define  $\nu$  and  $\bar{z}$ . For a given neutron-scattering contrast and wavelength, (3) indicates that the amount of multiple scattering depends linearly upon the sample thickness and the radii of the individual scatterers. Therefore, even though in practice thick samples ( $0.5$ - $1.0$  cm) are used to ensure copious multiple scattering, the MSANS formalism can also be applied to much thinner samples ( $0.1$ - $0.2$  cm) if the radii of the scatterers are sufficiently large. (From a practical standpoint, sample thickness can be chosen so that the wavelength dependence of the width of the scattering curve is easily observed within the range of available neutron wavelengths.)

Although the wavelength dependence at small  $Q$  seems to be the same as that for the multiple refraction regime, the underlying mechanism is different. When  $\nu = 1$ , an effective radius,  $R_{\text{eff}}(0)$ , where the 0 refers to  $Q = 0$ , can be determined for the scatterers from the wavelength dependence of  $r_c$  using the MSANS formalism represented in equations (2.12)-(2.15) of Berk & Hardman-Rhyne (1985, 1988). The dimensionless parameter  $r_c[QR] = r_c[Q]R$ , where [...] means with respect to, is related to  $\bar{z}$  via an empirical relation (Berk & Hardman-Rhyne, 1988)

$$r_c[QR] = 0.926\{\bar{z} \ln^{0.85} \bar{z}\}^{0.5} \text{ for } \bar{z} > 5, \quad (4)$$

which approximates the theory to better than 0.1% when  $\bar{z} > 10$ .

The MSANS formalism in effect replaces the standard Guinier analysis in the the small- $Q$  region of  $I(Q)$  where  $R_{\text{eff}}(0)$ , rather than  $R_g$ , defines the size of the scatterers. When polydispersity is present,  $R_{\text{eff}}(0)$  can be written in terms of the moments of an assumed particle-size distribution. For the small- $Q$  regime,  $R_{\text{eff}}(0) = \langle R^3 \rangle / \langle R^2 \rangle$  (Berk & Hardman-Rhyne, 1985), where the brackets denote the arithmetic average of the argument. Note that in the low- $\bar{z}$  limit the MSANS formalism no longer applies and the moments are expressed in terms of the Guinier radius of gyration such that  $R_g = [3\langle R^2 \rangle / 5\langle R^4 \rangle]^{1/2}$  (Kostorz, 1979). If a similar relation for the effective radius can be found using the large- $Q$  regime, then the average radius as well as the width of the size distribution can be found as shown below.

The standard Porod analysis (Kostorz, 1979) can be applied to the large- $Q$  region of  $I(Q)$ . In this region, the scattered intensity can be written as

$$I(Q) = PQ^{-4} + B, \quad (5)$$

where  $P$  is Porod's constant and  $B$  is a background term. The normalized total surface scattering area per unit volume,  $S/V_b$ , is determined directly from  $P$ . An effective pore radius,  $R_{\text{eff}}(\infty)$ , where  $\infty$  refers to the large- $Q$  regime, is calculated directly from  $S/V_b$  assuming spherical scatterers. For polydisperse systems, the moments of the size distribution are expressed as  $R_{\text{eff}}(\infty) = \langle R^3 \rangle / \langle R^2 \rangle$ . If both  $R_{\text{eff}}(0)$  and  $R_{\text{eff}}(\infty)$  are known,  $\langle R \rangle$  as well as the width,  $\beta$ , of an assumed particle-size distribution can be determined.

To apply the MSANS formalism to the analysis of scattering from a system of spheres containing no internal structure, (3) and (4) indicate that the sample thickness, the scattering volume fraction (which is a refinable parameter), the scattering-length density and the wavelength dependence of  $r_c$  must be known in order to derive  $R_{\text{eff}}(0)$ . In addition, the constraints that  $\bar{z} \geq 10$  and  $0.1 \leq \nu \leq 2$  must be satisfied. When  $\nu > 2$ , the scattering intensity falls into a crossover regime between diffraction and refraction. However, if  $\bar{z}$  is sufficiently large, the MSANS formalism may even apply if  $\nu > 2$  (Berk & Hardman-Rhyne, 1988).

The assumption that the scattering system is dominated by incoherent multiple scattering is extremely important since it means that the scattered intensity does not contain an interparticle interference term due to pair-pair correlations between particles. Since the scatterers are so large, i.e. comparable in size to the mean free path length of the neutrons, there is no coherent scattering between particles. Thus, even a dense system of scatterers may be considered dilute from the perspective of MSANS even though  $\phi/(1-\phi) \sim \phi$  does not apply.

Table 1. Alumina samples prepared from Baikowski CR6,  $6 \text{ m}^2 \text{ g}^{-1}$  powder

Sample	Thickness (cm)	Pore volume fraction, $\phi$	%TD Volumetric	MSANS
13-2	1.019	0.46	56.5	54
13-3	0.988	0.35	67.0	65
13-4	0.894	0.21	79.1	79
13-5	0.914	0.15	85.4	85
13-1	0.851	0.11	90.8	89
13-6	0.852	0.075	94.6	92.5
13-7	0.840	0.055	97.1	94.5
13-8	0.804	0.07	98.9	97.5

### 3. Alumina samples

The samples were prepared from Baikowski alumina powder ( $CR6, 6 \text{ m}^2 \text{ g}^{-1}$ ), slipcast to an average green density of 53% of theoretical density (TD), where  $TD = 3.965 \text{ g cm}^{-3}$ . The slip consisted of 43.5 vol.% alumina powder mixed into water along with 0.5 wt% of a polyelectrolyte dispersant (Darvan C). The suspension was ultrasonicated for 15 min and allowed to set overnight before being poured into molds with Teflon rings on top of plaster-of-paris blocks. After 55 min, the molds were removed from the blocks and sealed in a container overnight. The partially dried samples were then removed from the molds and sealed in containers for 2 d. The containers were then opened to the air for an additional 5–7 d before a series of oven-drying steps was performed as follows: 2 d at 337 K, 1 d at 354 K, 1 d at 375 K and 1 d at 389 K, after which a dry solid green body is obtained. In this fashion a family of eight nearly identical samples was prepared.

During sintering, samples were removed one by one at different times from the furnace to yield examples of material between 56.5 and 97.5% TD. The characteristics of the alumina samples are listed in Table 1. Sample densities measured volumetrically as well as those determined from the MSANS measurements are given. The sintering time-temperature curve is shown in Fig. 2. Each circle represents a sample removed from the furnace and the number alongside each circle is the measured %TD.

### 4. Neutron-scattering measurements

Measurements were made at the 20 MW research reactor at the National Institute of Standards and Technology (NIST). The NIST SANS facility (Glinka, 1981; Glinka, Rowe & LaRock, 1986) makes use of a velocity selector to choose the mean incident wavelength of the neutrons,  $\lambda$ , which have a wavelength spread  $\Delta\lambda/\lambda = 0.25$ . Copious neutron fluxes can be obtained in the wavelength region between 5 and 20 Å due to a cryogenic moderator installed in the reactor core. The neutron beam is collimated with a 12 mm aperture which follows the velocity selector and an 8 mm aperture which pre-

cedes the sample position. Scattered neutrons are detected by a  $64 \times 64 \text{ cm}$  position-sensitive detector divided into  $128 \times 128$  pixels. The data are circularly averaged to produce one-dimensional intensity,  $I(Q)$ , vs  $Q$  curves. Intensities measured for Porod analysis were placed on an absolute scale by comparison with  $I(Q)$  from a calibrated silica-gel sample measured under the same conditions.

The MSANS measurements were performed with no beamstop in front of the detector since the intense transmitted beam associated with conventional SANS measurements is absent. The absence of the beamstop ensures that the beam center can be found with high precision. With the center of the Gaussian precisely known, an accurate determination of the radius of curvature can be made. Measurement times ranged from 10 min to 1 h, depending upon the neutron wavelength. At the shortest wavelengths, the incident neutron beam is attenuated as needed in order to avoid saturating the detector. For a given wavelength, the broadest scattered intensity curves require the longest measuring times in order to accumulate sufficient counts.

### 5. Data analysis

#### 5.1. MSANS analysis

MSANS measurements were performed on each sample at a minimum of five neutron wavelengths. The scattering curves exhibited the expected broadening with increasing neutron wavelength as shown in

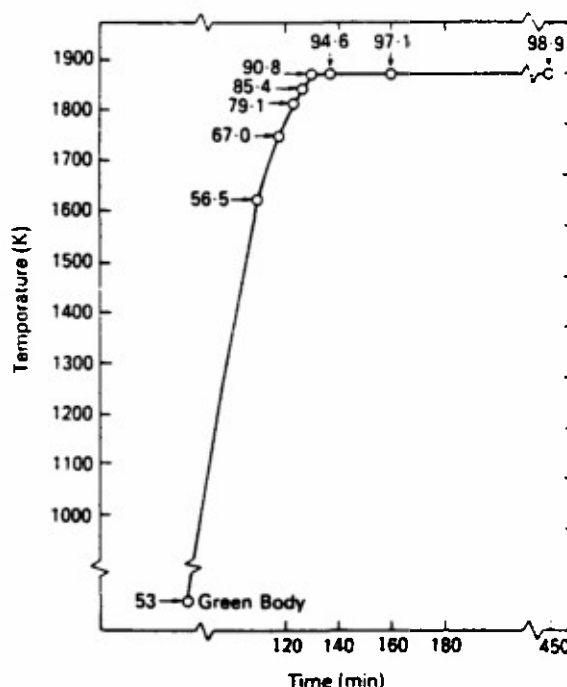


Fig. 2. Sintering time-temperature curve for the alumina samples. Each circle represents a sample removed from the furnace and the number alongside is the percent of theoretical density.

Fig. 3, where  $I(Q)$  vs  $Q$  curves, normalized to  $I(0) = 1.0$ , are plotted for the 85% TD sample. The features at  $Q \leq 0.005 \text{ \AA}^{-1}$ , most obvious for the longer-wavelength data, are due to a change in detector sensitivity at the beam-center position. To avoid this region, Gaussian fits were made to each curve in the  $Q$  range beginning where the intensity is  $\sim 85\text{--}90\%$  of  $I(0)$  and extending to  $\sim 45\%$  of  $I(0)$ . Below 40% of  $I(0)$ , the scattering curves did not fit well to a Gaussian.

For each curve fit, a radius of curvature is extracted from the standard deviation,  $\sigma$ , such that  $r_c = (1/2\sigma)^{1/2}$ . Blank spectra, measured at each wavelength with no scatterer in place, are also fitted to enable a correction for the instrument function (Hardman-Rhyne & Berk, 1985). Radii are extracted in each case from the empirical formula in (4) using (3) for  $\bar{z}$ . These values are averaged to obtain an effective radius,  $R_{\text{eff}}(0)$ , for the scatterers in each sample.

Finally, both  $R_{\text{eff}}(0)$  and the scattering-volume fraction,  $\varphi$ , are refined simultaneously for each sample using a least-squares fitting method. Owing to the approximate nature of the empirical formula (4), the full numerical MSANS analysis describing  $r_c$  as a function of  $\lambda$ , developed in (2.12)–(2.15) of Berk & Hardman-Rhyne (1985), is used in the refinement procedure.

## 5.2. Porod analysis

The scattering at large  $Q$  was measured for each sample with an incident neutron wavelength of  $6 \text{ \AA}$  and the detector offset to an angle of  $3.5^\circ$ . Sample transmissions were determined by dividing the total detector counts accumulated for each sample by the

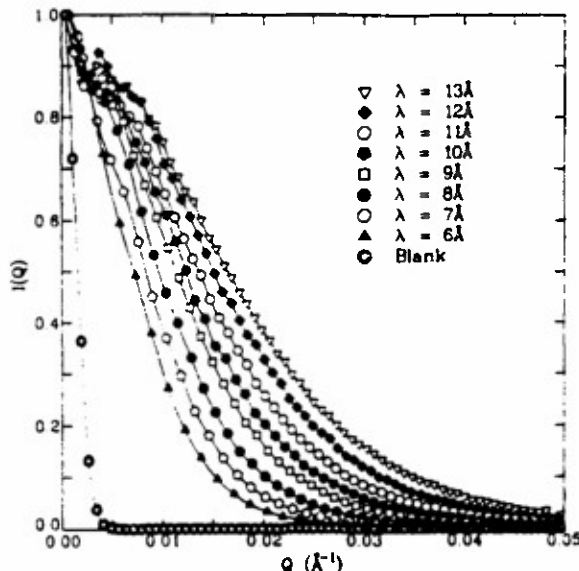


Fig. 3. Measured MSANS  $I(Q)$  vs  $Q$  curves from the 85% TD alumina sample for eight neutron wavelengths. The curve for the empty-beam 'blank' was taken at  $\lambda = 13 \text{ \AA}$ .

total detector counts accumulated under the same conditions with no sample in place. This method yields the equivalent of a single-scattering sample transmission. Values between 0.87 and 0.97 were measured, which fall within the range expected for  $\text{Al}_2\text{O}_3$  when no multiple scattering is present.

Since the scattered intensity follows (5) in the Porod regime, both the Porod constant,  $P$ , and the background term,  $B$ , were found directly by making linear least-squares fits to  $IQ^4$  vs  $Q^4$  curves for each sample. The largest possible linear region of the curves was fit. In each case, the maximum  $Q$  value was  $0.16 \text{ \AA}^{-1}$ , which is the largest  $Q$  value for which data were obtained. The minimum  $Q$  value ranged from  $0.035 \text{ \AA}^{-1}$  for the 97.5% TD sample to  $0.1 \text{ \AA}^{-1}$  for the 54% TD sample. The ratio of the normalized total scattering surface area to the volume of sample in the neutron beam  $S/V_b$  is determined directly from  $P$ . With the assumption of spherical scatterers,  $R_{\text{eff}}(\infty)$  for the large- $Q$  regime is also determined.

## 6. Results and discussion

The measured values of  $r_c(Q)$  (symbols) are plotted versus  $\lambda$  in Fig. 4 along with the theoretical values (solid lines) determined using the MSANS formalism [(2.12)–(2.15) in Berk & Hardman-Rhyne (1985)]. As the scattering volume fraction decreases (*i.e.* the %TD increases), the calculated values of  $R_{\text{eff}}(0)$  become

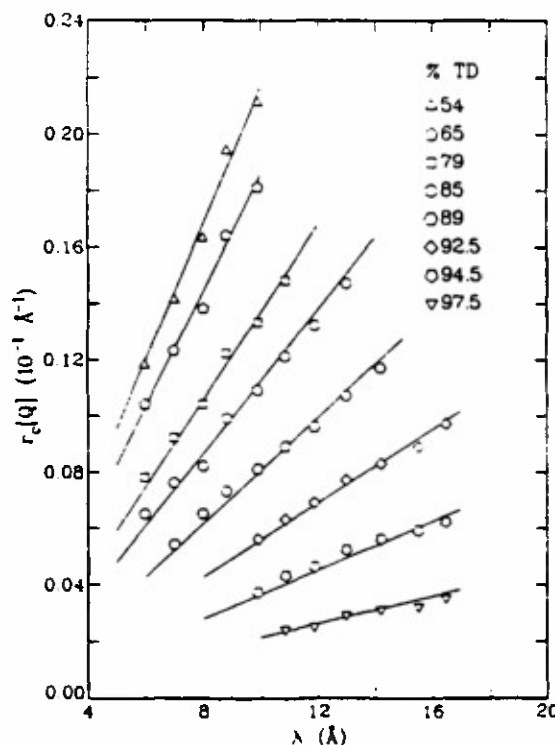


Fig. 4. Measured radii of curvature (symbols) and the corresponding MSANS theoretical fit (solid lines) as a function of neutron wavelength. The sample densities are those refined from the neutron-scattering measurements.

Table 2. MSANS results

Sample	%TD	Neutron wavelength $\lambda$ (Å)		$R_{\text{eff}}(0)$ (μm)	$\bar{z}$	Ratio*	Phase shift $\nu$	
		Min.	Max.				Min.	Max.
13-2	54	6.0	9.9	0.20(1)	152	14	26	0.13
13-3	65	6.0	9.9	0.19(1)	98	11	21	0.12
13-4	79	6.0	10.9	0.170(5)	49	193	7	0.10
13-5	85	6.0	13.0	0.18(1)	32	204	6	0.09
13-1	89	7.0	14.2	0.23(2)	47	234	7	0.17
13-6	92.5	9.9	14.2	0.32(3)	96	298	11	0.35
13-7	94.5	9.9	16.5	0.53(5)	73	248	9	0.45
13-8	97.5	10.9	16.5	0.75(15)	40	126	6	0.53

\* Ratio =  $R_{\text{eff}}(0)/R_s(0)$ , where  $R_s(0)$  is the pore radius calculated assuming no multiple scattering is present.

much more sensitive to small changes in the volume fraction,  $\phi$ . For example, an uncertainty of 0.01 on the value  $\phi = 0.01$  has a much greater effect on  $R_{\text{eff}}(0)$  than the same uncertainty on the value  $\phi = 0.4$ . In these cases, the refinement procedure was especially useful as it allowed the simultaneous determination of  $\phi$  and  $R_{\text{eff}}(0)$  values which best fit the  $r_c$  vs  $\lambda$  data. Values for the phase shift  $\nu$  ranged from 0.1 to 1.0, as shown in Table 2, which fall well within the allowed range for MSANS analysis.

The slopes of the  $r_c$  vs  $\lambda$  curves are steepest for the intermediate-stage alumina samples, which have the largest pore volume fraction. These samples also have the largest  $\bar{z}$  values and thus the largest amount of multiple scattering, even though the effective pore radii are smaller than those of the final-stage samples. In addition, the scattering intensities show beam broadening at smaller  $\lambda$  values and the width of the Gaussian at  $Q=0$  increases more rapidly with increasing  $\lambda$ .

When the pore volume fraction is small, as in the 97.5% TD sample,  $\bar{z}$  is correspondingly smaller and the slope of the  $r_c$  vs  $\lambda$  curves is much flatter. Since the amount of multiple scattering is much less in the denser samples, the scattered intensities must be measured using longer-wavelength neutrons for beam broadening to be observed. Without the cryogenic moderator, copious neutron fluxes at wavelengths beyond  $\sim 12$  Å would not be available and the most dense samples could not have been measured using the MSANS technique.

The refined value for the effective pore radius  $R_{\text{eff}}(0)$ , obtained from the data in Fig. 4, is listed for each sample in Table 2, along with the ranges of  $\lambda$ ,  $\bar{z}$  and  $\nu$ . Also listed is the ratio of  $R_{\text{eff}}(0)$  to the equivalent spherical radius  $R_s(0)$  calculated assuming that no multiple scattering is present, i.e. using the standard Guinier analysis to obtain  $R_g$  and then assuming spherical scatterers to obtain  $R_s(0)$ .

The data points from Fig. 4 for all of the samples (circles) along with the empirical curve as given by (4) (solid line) are plotted as a function of  $\bar{z}$  in Fig. 5. The dimensionless parameter  $r_c[QR]$  is obtained by multiplying  $r_c[Q]$  by the best  $R_{\text{eff}}(0)$  value for each

sample after refinement. The  $\bar{z}$  values for these samples range from 40 to 400, well within the range of validity of the empirical formula. Thus, excellent agreement with (4) is expected.

A  $\ln(I)$  vs  $\ln(Q)$  plot of the Porod data (circles) for the 85% TD sample is shown in Fig. 6. The fitted background term [see (5)] of  $0.018(1)$  cm<sup>-1</sup> was subtracted prior to plotting. The solid line is the linear fit to  $\ln(I)$  vs  $\ln(Q)$  in the range  $0.055 \leq Q \leq 0.155$  Å<sup>-1</sup>, where the slope was determined to be  $-4.02(2)$ . The effective pore radius,  $R_{\text{eff}}(\infty)$ , and the minimum  $Q$  value used for the Porod fit are listed in Table 3 for each sample, along with the normalized total scattering surface area,  $S/V_b$ . The normalized pore volume fraction  $\phi/(S/V_b)$  and the number of pores per unit sample volume,  $N/V_b$ , are also tabulated for each sample.

The  $R_{\text{eff}}(0)$  and  $R_{\text{eff}}(\infty)$  values calculated from the MSANS and Porod measurements, respectively, are plotted in Fig. 7, along with those obtained using

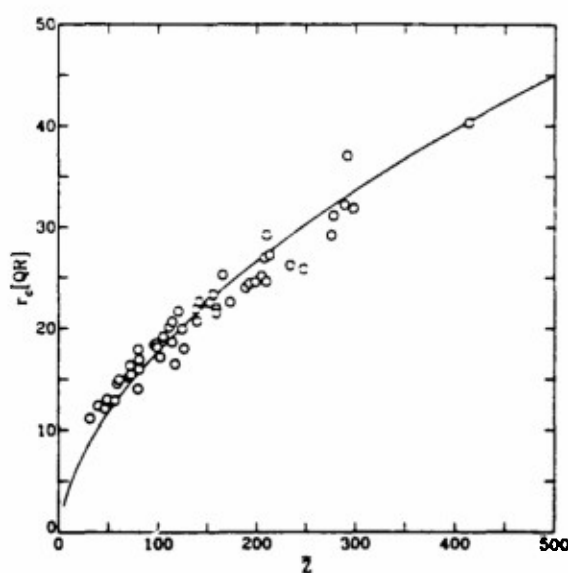


Fig. 5. Combined plot of  $r_c[QR]$  vs  $z$  for all samples at all neutron wavelengths measured. The solid line is the empirical formula (4). The data points are the products of the measured  $r_c[Q]$  and the best-fit value for the effective pore radius,  $R_{\text{eff}}(0)$ , for each sample.

mercury intrusion porosimetry (Rootare & Prenzlow, 1967) for the samples below 85% TD, where open porosity is expected. The MSANS determinations, which are weighted to the larger volume scatterers (Long & Krueger, 1989), indicate that the average pore radius for the distribution within the alumina is essentially flat, with a value of  $\sim 0.2 \mu\text{m}$ , in the intermediate sintering stage and increases sharply to  $\geq 0.6 \mu\text{m}$  in the final stage. The large error bar on the value for the 97.5% TD sample is a consequence of the shallow slope in the  $r_c$  vs  $\lambda$  curve (Fig. 4). Since three local minima in the  $\chi^2$  fitting parameter were found for  $R_{\text{eff}}(0)$  values between  $0.6$  and  $0.9 \mu\text{m}$ , no single fit could be chosen as the 'best fit' to the MSANS formalism. An uncertainty in the pore volume fraction,  $\varphi$ , of approximately 0.005 was also found from the fitting procedure.

The  $R_{\text{eff}}(\infty)$  values determined from the Porod analysis are weighted to the particles with the smallest scattering surface areas. Although consistently lower, the  $R_{\text{eff}}(\infty)$  values agree qualitatively with the  $R_{\text{eff}}(0)$  values. The average pore radius remains nearly constant at a value of  $\sim 0.1 \mu\text{m}$  throughout the intermediate stage and increases to  $\geq 0.4 \mu\text{m}$  in the final stage. The large error bar on  $R_{\text{eff}}(\infty)$  for the 97.5% TD sample is mainly due to the uncertainty in  $\varphi$  as determined from the MSANS analysis.

The porosimetry results agree qualitatively with results obtained from both the MSANS and Porod analyses for intermediate-stage sintering. The observed quantitative discrepancies are expected since the MSANS and Porod radii are derived from a measure of all of the voids in the system, with MSANS radii weighted to the larger-volume and

Porod radii weighted to the smaller-volume voids. On the other hand, the porosimetry radii mainly represent the size of the small necks between pores.

Mercury intrusion porosimetry assumes that the largest pores are on the outside of the sample. This is important because the pressure required to fill a large pore is less than that required to fill a small pore. However, as the mercury penetrates a homogeneous sample consisting of a random distribution of necks and larger channel-like voids, a significant number of necks may be encountered before the mercury reaches the open channels. Since the neck size is measured at a higher pressure than that required for the open channel, the mercury reaches the channel after the appropriate pressure to measure its size has been exceeded. Thus, large voids in the interior of a sample may not be measured, even if they form a majority population.

The MSANS and Porod results for pore size assume spherical scatterers whereas the porosimetry results are obtained assuming cylindrical pore morphology. Yet the same trend in the evolution of the effective pore radius during intermediate stage sintering is reported in each case. This occurs because the average length of the cylindrical channels is  $\geq 10 \mu\text{m}$ , which is beyond the measurable range of even the MSANS technique. Thus, the pore channels can be effectively represented by strings of spheres, with  $R_{\text{eff}}(0)$  and  $R_{\text{eff}}(\infty)$  corresponding to the cross-sectional radii of the cylinders.  $R_{\text{eff}}(0)$  is dominated by the larger-diameter and  $R_{\text{eff}}(\infty)$  by the smaller-diameter channels in the size distribution.

The important result of the MSANS, Porod and porosimetry measurements is that the effective pore radius remains constant through the intermediate stage of sintering. This is consistent with topological decay models of the intermediate sintering stage in which an interconnected pore network decays in a stable manner (Rhines & DeHoff, 1984). Throughout this stage, the network of interconnected channels decays such that the ratio  $\varphi/(S/V_b)$ , or pore volume fraction to surface area per unit volume of sample in the neutron beam, remains constant (DeHoff, Rummel, LaBuff & Rhines, 1966). Consequently, the pore channels become fewer while retaining a constant diameter as densification proceeds. This can easily be observed in Tables 2 and 3, which show constant  $R_{\text{eff}}(0)$ ,  $R_{\text{eff}}(\infty)$  and  $\varphi/(S/V_b)$  values for the intermediate-sintering-stage samples. Also shown is the number of pores per unit sample volume ( $N/V_b$ ), which decreases sharply, as expected, as intermediate-stage sintering progresses.

Before the channels have disappeared altogether, a transition into the final sintering stage occurs in which the porosity becomes isolated. Pore isolation occurs because the channels rupture or 'pinch off' when they can no longer maintain their length while at the same time remaining stable against the increas-

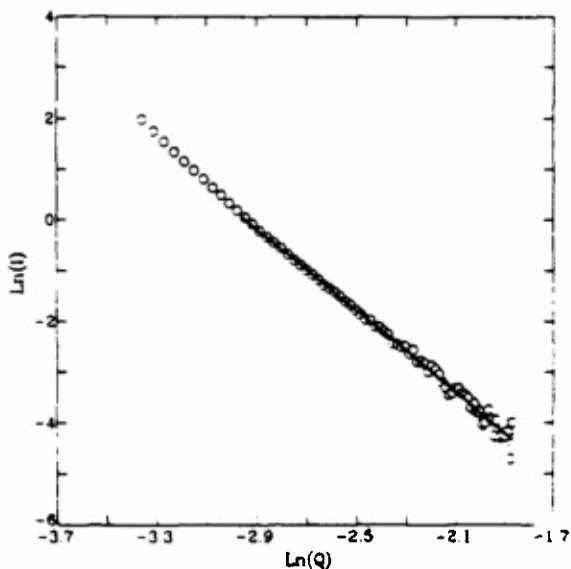


Fig. 6. Porod data for the 85% TD sample plotted on a  $\ln(I)$  vs  $\ln(Q)$  scale after subtraction of the filled background term [see (5)]. The solid line is the linear least-squares fit to the data in the range  $0.055 \leq Q \leq 0.155 \text{ \AA}^{-1}$ . The fitted slope is  $-4.02(2)$ .

Table 3. Porod results

Sample	%TD	$Q_{\min} (\text{\AA}^{-1})$	Pore radius $R_{\text{eff}}(\infty) (\mu\text{m})$	Normalized surface area $S/V_b^*$ ( $\times 10^4 \text{ cm}^{-1}$ )	Normalized pore volume $\phi/(S/V_b)$ ( $\times 10^{-6} \text{ cm}^3$ )	Number of pores per unit volume $N/V_b$ ( $\times 10^{12} \text{ cm}^{-3}$ )
13-2	54	0.10	0.091(1)	15.2(2)	3.03(4)	147.0(27)
13-3	65	0.09	0.108(1)	9.7(1)	3.60(4)	66.0(5)
13-4	79	0.07	0.108(1)	5.83(3)	3.60(2)	39.6(48)
13-5	85	0.065	0.120(1)	3.74(2)	4.01(2)	20.5(18)
13-1	89	0.055	0.154(1)	2.15(1)	5.12(2)	7.2(10)
13-6	92.5	0.045	0.185(1)	1.22(1)	6.16(3)	2.84(72)
13-7	94.5	0.04	0.298(2)	0.553(3)	9.93(4)	0.495(5)
13-8	97.5	0.035	0.44(9)	0.1623(4)	14.5(29)	0.08(3)

\*  $S/V_b$  is the ratio of the total scattering surface area to the volume of the sample in the neutron beam, where the beam diameter is 0.9 cm.

ing sintering force (Rhines & DeHoff, 1984). The isolated pores become more spherical, achieving radii which are greater than the cross-sectional radii of the original channels, yet are still within the MSANS range. As the number of isolated pores increases, their larger dimension increasingly contributes to the total scattering, until it finally dominates the measured MSANS intensities. Thus, as seen in Tables 2 and 3,  $R_{\text{eff}}(0)$  and  $R_{\text{eff}}(\infty)$  begin increasing gradually as the transition from intermediate to final-stage sintering begins. Late in the final sintering stage, a more rapid increase in both  $R_{\text{eff}}(0)$  and  $R_{\text{eff}}(\infty)$  is observed as the microstructure becomes dominated by isolated pores.

### 7. Concluding remarks

The multiple small-angle neutron-scattering technique was successfully used to observe the transition

from one sintering stage to another in the densification of alumina. The effective radius of the pore-size distribution, as measured by MSANS, Porod scattering and mercury porosimetry, remained constant throughout the intermediate stage of sintering, with a rapid increase measured by MSANS and Porod scattering as densification proceeds beyond 85% of theoretical density. These results are consistent with sintering models which equate the intermediate stage with the stable decay of a topological network of channels and junction pores in the system. Before complete densification can occur, a transition into the final sintering stage takes place in which the porosity forms isolated spherical voids. The Porod and MSANS results for the radii of the final-stage voids agree qualitatively, indicating that the pore-size distribution does not broaden appreciably as its peak advances toward higher  $R$  values during late-stage densification.

The agreement among the MSANS, Porod and porosimetry results concerning the constant value of the pore radius during the intermediate stage illustrates that the MSANS formalism, as applied to the alumina system, is adaptable to the use of strings of spheres to describe cylindrical pore channels and is thus not limited by the restriction of isolated spherical scatterers. The quantitative differences between the scattering and the porosimetry results arise because the MSANS and Porod radii are derived from a measure of all of the voids in the system, with MSANS radii weighted toward the larger and Porod radii weighted toward the smaller voids. However, in a system consisting of a homogeneous distribution of pore sizes, such as alumina, the porosimetry radii are dominated by the size of the small necks between pore channels.

As densification proceeds beyond 85% TD, the channels become pinched off and then the transition from an open pore network to isolated pores occurs, resulting in an increase in both  $R_{\text{eff}}(0)$  and  $R_{\text{eff}}(\infty)$ . Although even the largest pores are expected to begin to shrink by 95% TD (Johnson, 1990), the scattering results (Fig. 7) indicate that  $R_{\text{eff}}(0)$  and  $R_{\text{eff}}(\infty)$  may

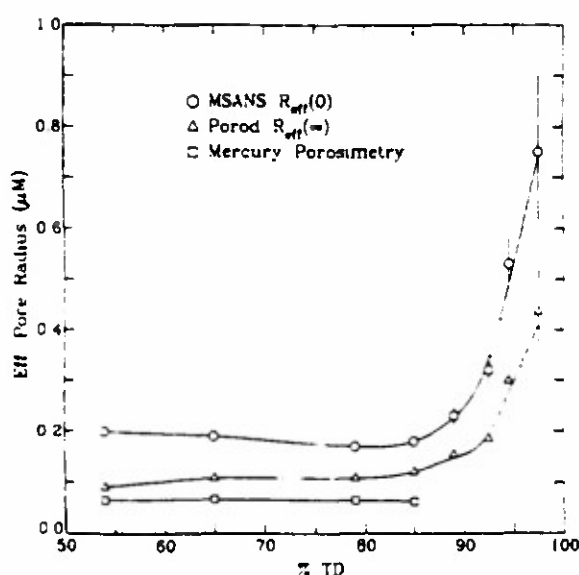


Fig. 7. Effective pore radii for the alumina samples as a function of percent theoretical density determined from the MSANS formalism from a Porod analysis and from mercury porosimetry measurements on the samples below 85% TD, where open porosity is expected.

still be increasing at 97.5% TD. This suggests that discontinuous grain growth may be taking place. However, the large uncertainties in the scattering volume fraction,  $\varphi$ , and the effective radii,  $R_{\text{eff}}(0)$  and  $R_{\text{eff}}(\infty)$ , preclude drawing firm conclusions.

Although the final-stage samples were originally intended for single-scattering SANS measurements, it was found that even the 97.5% TD sample was within the limit of applicability of the MSANS technique. There was significant wavelength-dependent beam broadening and even the smallest  $\bar{z}$  value ( $\bar{z} = 40$ ) is well within the MSANS formalism. However, the fact that  $\varphi$  is so small means that the change in  $r_c$  as a function of  $\lambda$  is small (see Fig. 4). This nearly flat slope makes the refinement procedure difficult, resulting in large uncertainties in the fitted  $R_{\text{eff}}(0)$  and  $\varphi$  values. To improve the determination of  $R_{\text{eff}}(0)$  during final-stage sintering, measurements of the higher-density samples are planned with a high-resolution small-angle X-ray scattering instrument (Long, Jemian, Weertman, Black, Burdette & Spal, 1991). This instrument can measure the single-scattering intensities from pores 4.0 nm to 1.0  $\mu\text{m}$  in size and thus bridge the gap between those sizes which can be easily measured by conventional SANS and MSANS techniques.

This work was supported in part by the US Army Research Office under contract no. MIPR ARO 102-90 and in part by the Department of Energy under grant no. DE-FG05-84ER45063.

#### References

- BERK, N. F. & HARDMAN-RHYNE, K. A. (1985). *J. Appl. Cryst.* **18**, 467-472.
- BERK, N. F. & HARDMAN-RHYNE, K. A. (1988). *J. Appl. Cryst.* **21**, 645-651.
- COBLE, R. L. (1961). *J. Appl. Phys.* **32**, 787-792, 793-799.
- DEHOFF, R. T., RUMMEL, R. A., LABUFF, H. P. & RHINES, F. N. (1966). *Modern Developments in Powder Metallurgy*, edited by H. H. HAUSNER, Vol. I, pp. 310-331. New York: Plenum Press.
- GANS, R. (1925). *Ann. Phys. (Leipzig)*, **76**, 29-38.
- GLINKA, C. J. (1981). *Neutron Scattering. AIP Conf. Proc.* No. 89, pp. 395-397.
- GLINKA, C. J., ROWE, J. M. & LAROCK, J. G. (1986). *J. Appl. Cryst.* **19**, 427-439.
- HARDMAN-RHYNE, K. A. & BERK, N. F. (1985). *J. Appl. Cryst.* **18**, 473-479.
- JOHNSON, D. L. (1990). Private communication.
- KINGERY, W. D. & BERG, M. (1955). *J. Appl. Phys.* **26**, 1205-1212.
- KDSTORZ, G. (1979). *A Treatise on Materials Science and Technology*, edited by H. HERMAN, Vol. 15, pp. 227-289. New York: Academic Press.
- LONG, G. G., JEMIAN, P. R., WEERTMAN, J. R., BLACK, D. R., BURDETTE, H. E. & SPAL, R. (1991). *J. Appl. Cryst.* **24**, 30-37.
- LONG, G. G. & KRUEGER, S. (1989). *J. Appl. Cryst.* **22**, 539-545.
- NARDROFF, R. VON (1926). *Phys. Rev.* **28**, 240-246.
- POROD, G. (1951). *Kolloid Z.* **124**, 83-114.
- RAYLEIGH, J. W. LORD (1910). *Proc. R. Soc. London Ser. A*, **84**, 25-46.
- RAYLEIGH, J. W. LORD (1914). *Proc. R. Soc. London Ser. A*, **90**, 219-225.
- RHINES, F. N. & DEHOFF, R. T. (1984). *Sintering and Heterogeneous Catalysis. Materials Science Research*, edited by G. C. KUCZYNSKI, A. E. MILLER & G. A. SARGENT, Vol. 16, pp. 49-61. New York: Plenum Press.
- ROOTARE, H. M. & PRENZLOW, C. F. (1967). *J. Phys. Chem.* **71**, 2733-2736.
- WEISS, R. J. (1951). *Phys. Rev.* **83**, 379-389.

# The Effect of Green Density and the Role of Magnesium Oxide Additive on the Densification of Alumina Measured by Small-Angle Neutron Scattering

Gabrielle G. Long\* and Susan Krueger

National Institute of Standards and Technology, Gaithersburg, Maryland 20899

Richard A. Page\*

Southwest Research Institute, San Antonio, Texas 78228

Small-angle neutron scattering measurements were used to examine the effect of green density and the role of MgO additive on the evolution of the porous microstructure of alumina during intermediate- and final-stage sintering. It was found that the initial connectivity in the green state plays a dominant role in establishing the channel diameters during the intermediate stage of sintering, and contributes also to determining the onset density at which the final stage of sintering begins. The role of MgO as a sintering aid lies, at least in part, in prolonging the stability of intermediate-stage sintering such that the body achieves greater density before the transition to final-stage sintering after which isolated pores are formed. [Key words: alumina, microstructure, sintering, characterization, neutrons.]

## I. Introduction

NUMEROUS sintering models have been developed over the years in attempts to reliably predict the kinetics of sintering and to estimate sintering rates. From a theoretical perspective, it is often difficult to proceed beyond idealized systems because of the complexity of real powder compacts. Experimentally, quantitative characterization is often hampered by the existence of a wide variety of conditions under which observations of the evolving physical system must be made. Although it has been difficult to find a consensus regarding many aspects of sintering mechanisms, there is general agreement that the driving force for sintering is the surface free energy, and that the microstructure characteristics determine the specific mechanisms by which the pore and the solid phases evolve during densification. The present investigation was undertaken to examine the microstructure evolution during sintering with the goal being to gain insight into the mechanisms operative during thermal processing.

Small-angle neutron scattering is a well-developed and recognized technique for the statistically significant characterization of microstructures in the 1 nm to 0.1  $\mu\text{m}$  range. This traditional size range, which is too low to include most of the microstructure relevant to ceramic research, has recently been extended to 10  $\mu\text{m}$  by the development of a multiple neutron scattering formalism. The new multiple scattering

formalism is directly applicable to the important questions concerning ceramic microstructure evolution during sintering in that it is valid for samples containing a large volume fraction of open or closed pores in the size range between 0.08 and 10  $\mu\text{m}$ . Indeed, the new technique is applicable to most, and under certain conditions all, porous microstructures from early-stage through intermediate- and final-stage thermal processing.

In the experiments that form the subject of this paper, samples of undoped alumina and of alumina with 0.25 wt% MgO added were prepared by slip casting, or alternatively by cold pressing. For each green density, a collection or suite of nearly identical samples were conventionally sintered. During sintering, these samples were removed one by one from the furnace as they reached densities between 52% and 99% of theoretical, yielding examples of microstructure from the early part of the intermediate stage of sintering out to the latter part of final-stage sintering. The microstructure parameters of these samples were derived from multiple small-angle neutron scattering measurements. In particular, the microstructure evolution as a function of green density and as a function of MgO additive was studied.

## II. Multiple Small-Angle Neutron Scattering Formalism

The application of the multiple small-angle neutron scattering (MSANS) technique<sup>1,2</sup> to microstructure evolution as a function of the thermal processing of ceramics has been described earlier.<sup>3,4</sup> In this paper, an overview of the assumptions involved is given and the general features of the formalism are described.

Unlike conventional small-angle neutron scattering (SANS), the scattering in the MSANS diffraction regime is dominated by incoherent multiple neutron scattering. Whether a particular scattering experiment is in the SANS or in the MSANS regime is determined by the value of the phase shift  $\nu$  that a neutron undergoes in traversing a particle or pore of radius  $R$ . The phase shift depends on three parameters—the contrast  $\Delta\rho$  of the scattering particle or pore relative to the matrix, the neutron wavelength  $\lambda$ , and the particle size  $2R$ :

$$\nu = 2\Delta\rho\lambda R \quad (1)$$

In SANS,  $\nu \ll 1$ , whereas in MSANS,  $0.1 < \nu < 2$ . A measure of the amount of multiple scattering is given by a parameter  $\bar{z}$ , called the scattering power, which is the sample thickness,  $z$ , divided by the neutron mean free path length,  $\ell$ :

$$\bar{z} = z/\ell = 1.5\phi z(\Delta\rho\lambda)^2 R \quad (2)$$

$\phi$  is the volume fraction of scatterers, which for ceramic bodies more than 50% dense is  $1 - d/d_{th}$ , where  $d$  is the sample density and  $d_{th}$  is the theoretical density of a fully densified body.  $\Delta\rho$  is the neutron contrast scattering-length density<sup>4</sup> of

T. Shaw—contributing editor

Manuscript No. 197246. Received October 3, 1990; approved March 22, 1991.

Presented at the 91st annual meeting of the American Ceramic Society, Indianapolis, IN, April 26, 1989 (Basic Science Division, Paper No. 83-B-89). Supported by the U.S. Army Research Office under Contract No. MIPR-ARO 102-90 and by the U.S. Department of Energy under Grant No. DE-FG03-84ER45063.

\*Member, American Ceramic Society.

spectra, measured at each wavelength with no scatterer in place, were also fitted to enable a correction<sup>8</sup> for instrumental broadening. The radii of the pores were extracted from each curve using an empirical formula<sup>2</sup> for the description of MSANS:

$$r_c[Q] = 0.926\{\bar{z} \ln^{0.85} \bar{z}\}^{0.5} \quad (\text{for } \bar{z} \geq 5) \quad (3)$$

where  $\bar{z}$  is given by Eq. (2) and  $[ \dots ]$  means with respect to and defines the scale for describing  $r_c$ . These values of  $R$ , derived from the fitted values of  $r_c$  for each wavelength, were averaged together to obtain an effective radius  $R_{eff}(0)$  for the scattering pores in each sample. The (0) is a reminder that this derivation of effective pore radius comes from an analysis of the portion of the scattering curves near  $Q = 0$ .

Finally, both  $R_{eff}(0)$  and the scattering volume fraction,  $\phi$ , were refined simultaneously for each sample using a least-squares fitting method. Because of the approximate nature of

Eq. (3), the full numerical MSANS analysis describing the dependence of the radius of curvature on neutron wavelength, developed in Eqs. 2.12 to 2.15 of Berk and Hardman-Rhyne,<sup>1</sup> was used in the refinement procedure.

The measured  $r_c$  (symbols) vs wavelength for each of the four suites of samples is shown in Fig. 3, along with theoretical values (solid lines) determined by means of the MSANS formalism. The good fit between the measurements and the theory suggests that the MSANS formalism is well-suited to the analysis of the porous microstructure of these samples.

## V. Results and Discussion

Results from the measurements on the slip-cast alumina (series 13) samples are considered first. The Porod results for these samples are given in Table II, and the evolution of the number density as a function of percent theoretical density is

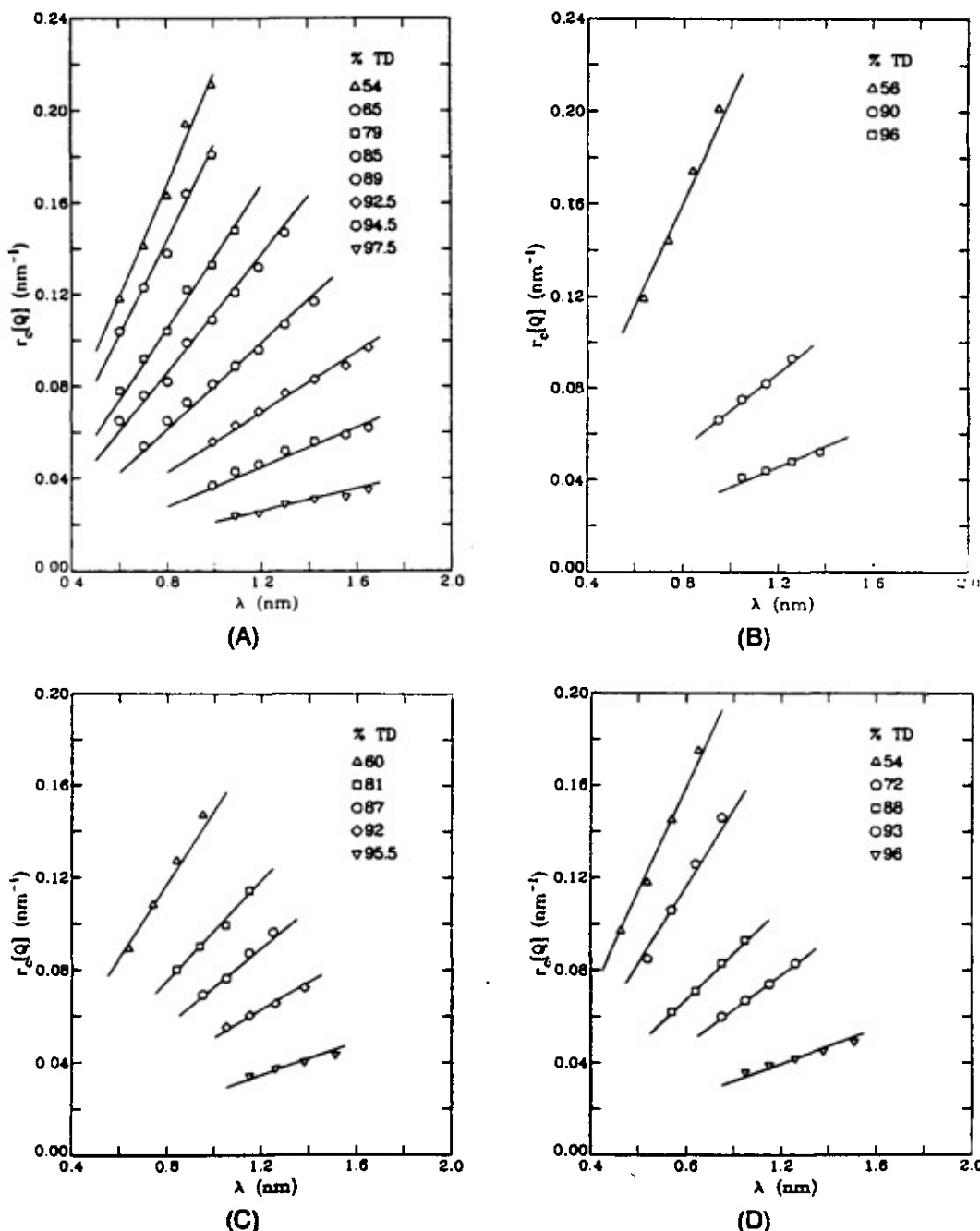


Fig. 3. Measured radii of curvature (symbols) and the corresponding MSANS theoretical fit (solid lines) as a function of neutron wavelength for (A) the 13-series, (B) the V-series, (C) the 15-series, and (D) the D-series.

Table II. Porod Results for the (13-Series) Slip-Cast Alumina Samples

Sample	$Q_{exp}$ ( $\text{\AA}^{-1}$ )	Surface area ( $\times 10^4 (\text{S}/\text{V}) \text{ cm}^{-1}$ )	Number density ( $\times 10^{12} \text{ cm}^{-3}$ )	$R_{eff}(\infty)$ ( $\mu\text{m}$ )	$\phi/S_s$
13-2	0.10	$15.20 \pm 0.2$	$147 \pm 27$	$0.091 \pm 0.001$	$3.03 \pm 0.04$
13-3	0.09	$9.71 \pm 0.1$	$66 \pm 15$	$0.108 \pm 0.001$	$3.60 \pm 0.04$
13-4	0.07	$5.83 \pm 0.03$	$39.6 \pm 4.8$	$0.108 \pm 0.001$	$3.60 \pm 0.02$
13-5	0.065	$3.74 \pm 0.02$	$20.5 \pm 1.8$	$0.120 \pm 0.001$	$4.01 \pm 0.02$
13-1	0.055	$2.15 \pm 0.01$	$7.2 \pm 1.0$	$0.154 \pm 0.001$	$5.12 \pm 0.02$
13-6	0.045	$1.218 \pm 0.005$	$2.84 \pm 0.72$	$0.185 \pm 0.001$	$6.16 \pm 0.03$
13-7	0.04	$0.553 \pm 0.003$	$0.495 \pm 0.005$	$0.298 \pm 0.002$	$9.93 \pm 0.04$
13-8	0.035	$0.1723 \pm 0.0004$	$0.08 \pm 0.03$	$0.44 \pm 0.09$	$14.5 \pm 2.9$

shown in Fig. 4. The number of pores per unit volume decreases by several orders of magnitude as densification of the alumina proceeds. Figure 5 shows the evolution of the MSANS-derived pore radius,  $R_{eff}(0)$ , for the same slip-cast alumina samples as a function of densification. Although the number of pores is rapidly decreasing, the actual size of the pores is constant over the entire range of densities representative of intermediate-stage sintering, from about 55% to approximately 87% TD. In the final stage of sintering, above 87% TD, the size of the pores increases rapidly despite the rapid decrease in their numbers. Also shown in Fig. 5 are the Porod-derived pore radii,  $R_{eff}(\infty) = 3\phi/S_s$ , where  $(\infty)$  indicates the large  $Q$  region of the scattering pattern and  $S_s$  is the surface scattering area per unit volume. Finally, results are also shown from MIP measurements over the range of densities where the pore structure was open enough for this technique to be attempted. The  $R_{eff}(\infty)$  results are in qualitative agreement with the  $R_{eff}(0)$  results in that they both indicate a constant pore radius during the intermediate stage of sintering and a rapidly increasing pore size during the final stage of sintering. The porosimetry results qualitatively confirm both of the neutron scattering analyses by again indicating a constant effective pore radius for the intermediate stage. The ordering of sizes from these three techniques is as expected since the MSANS results are volume-weighted,<sup>1</sup> emphasizing the population of large pores in the distribution, the Porod SANS results are surface-area-weighted,<sup>1</sup> emphasizing the smaller pores in the distribution, and the porosimetry results are limited by the narrow necks connecting the large population of larger pores.

All three techniques indicate that the effective pore size and also the pore morphology are constant through the intermediate sintering stage of alumina. These results lend support to the topological decay model of Rhines and DeHoff<sup>9</sup> in which the interconnected network of pores decays in a stable

manner. During the intermediate stage, the interconnected pore channels decay such that the volume fraction to surface area per unit volume ( $\phi/S_s$ ) remains constant.<sup>10</sup> Consequently, the pore channels become fewer, while retaining the same diameter, as densification proceeds. From Table II, the Porod results for the ratio of the volume fraction to surface area per unit volume can be seen to have nearly constant values throughout the intermediate sintering stage.

Next, MSANS results from all four suites of samples are considered. Figure 6 shows the evolution of the pore size as a function of densification for the four suites of samples, and Table III lists the experimental MSANS parameters and the effective pore radii. The numbers associated with the left-most symbols in the figure indicate the average green density of each suite of samples. As one might expect from the results on undoped alumina shown in Fig. 5, the effective pore radius was constant during the intermediate stage of sintering for each of the suites of samples. However, the actual value of  $R_{eff}(0)$  depends inversely on the green density as shown in Table IV. The greater the green density, the smaller the effective radius that persists during intermediate-stage sintering. Evidently, once the size of the pore channels is established, it is constant until the onset of the final stage of sintering. These results indicate that for the alumina system the connectivity that is established in the green body determines the pore size throughout the stable intermediate sintering stage, and once this size is determined, it is unvarying as long as isolated porosity has not yet begun to form.

At the onset of final-stage sintering, the pore radius apparently coarsens abruptly. Part of this apparent coarsening may be due to the pinching-off of pore channels such that the larger dimension of the newly isolated pores comes increasingly within the range of sizes visible to the MSANS technique. Another possibility is that the increase in the effective pore radius may be smaller than it seems if the error bars on

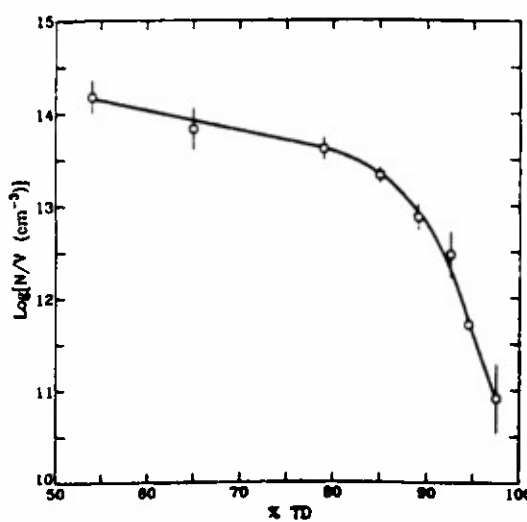


Fig. 4. Number density vs %TD for the 13-series undoped alumina samples.

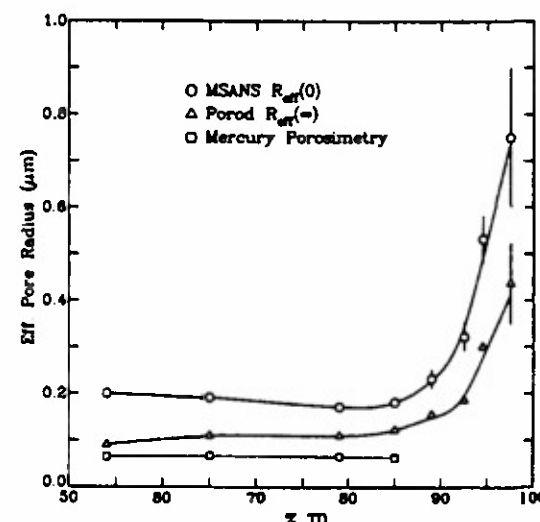


Fig. 5. Effective pore radii for the 13-series alumina as a function of %TD derived from MSANS, from Porod scattering, and from MIP.

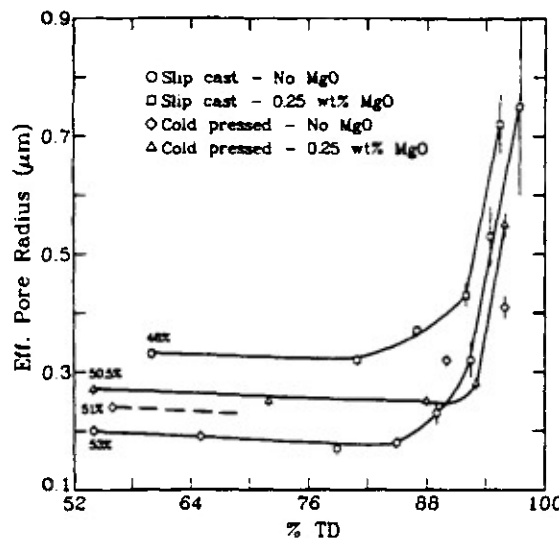


Fig. 6. Effective pore radii,  $R_{eff}(0)$ , as a function of %TD for all four series of samples. The number appearing near the leftmost symbols is the average green body density for each series.

the measurements could be reduced. A future objective of the authors is an investigation of the final stage of sintering in alumina with improved resolution. The present objective which remains is the determination of the influence of MgO additive on pore coarsening in the final stage.

Figure 6 indicates that for the D-series of samples with 0.25 wt% MgO, the intermediate sintering stage remains stable out to significantly higher density (~93% TD) than the undoped alumina 13-series, which remains stable out to ~87% TD. Consequently, the pores in the doped sample begin to coarsen later and thus do not suffer the same degree of exaggerated growth evident in the thermal processing of the undoped alumina, even though the average green density was lower in the doped sample. Similarly, the transition to the final sintering stage for the doped sample with the lowest green body density (15-series) occurs no later in the densification process (~87% TD) than the transition in the undoped alumina with higher average green density. Evidently, while the green density determines the scale of the pore channel size in intermediate-stage sintering and, in part, determines when

the transition to final-stage sintering will occur, the MgO sintering aid can effectively alter the position of the transition between connected and isolated porosity. The transition to isolated porosity is delayed in the doped alumina because the additive apparently enhances the stability of the intermediate sintering stage during which most of the porosity is removed. Since isolated pores begin to form in the doped sample only after the remaining porosity is significantly reduced, there is less opportunity for pore coarsening to take place. Reductions in pore coarsening have also been observed in SANS measurements of plasma-sintered MgO-doped alumina.<sup>11</sup>

The present study has followed the microstructure evolution of porosity as a function of sintering to gain insight into densification processes. Research by others<sup>12,13</sup> has focused on the evolution of the mean pore spacing or on the behavior of the dihedral angle between the free surfaces of grains sharing a grain boundary. Although the force balance is most directly related to the dihedral angle, all three types of measurement—pore size, mean pore spacing, and dihedral angle—are complementary. In particular, it was found that the mean pore spacing by number (see Fig. 17 of Ref. 12) is constant during the intermediate sintering stage and increases during final-stage sintering. Thus the trends observed for the mean pore spacing, which is also some measure of the grain behavior, are the same as those observed in the pore sizes measured in the present SANS study. Measurements<sup>13</sup> of the dihedral angle in nearly fully dense alumina and alumina doped with 0.25 wt% MgO found that while the median dihedral angle was the same in both cases, the doped sample had a significantly narrower distribution of dihedral angles. High-resolution SAXS measurements<sup>14</sup> currently under way are being used to examine the evolution of the pore size distribution, as a function of doping, as alumina approaches full theoretical density.

## VI. Summary and Conclusions

A combination of small-angle neutron scattering (Porod) measurements, multiple small-angle neutron scattering measurements, and mercury intrusion porosimetry measurements was used to investigate the effect of green body density and the role of MgO sintering aid on the densification of alumina. It was found that the initial connectivity that is established in the green body plays a dominant role in establishing the channel diameters during the intermediate stage of sintering. It

Table III. MSANS Results

Sample No.	%TD	Wavelength (nm)		$R_{eff}$ ( $\mu\text{m}$ )	$\xi$		Phase shift	
		Min	Max		Min	Max	Min	Max
13-2	54	0.60	0.99	$0.20 \pm 0.01$	152	414	0.13	0.22
13-3	65	0.60	0.99	$0.19 \pm 0.01$	98	289	0.12	0.21
13-4	79	0.60	1.09	$0.17 \pm 0.005$	49	193	0.10	0.22
13-5	85	0.60	1.30	$0.18 \pm 0.01$	32	204	0.09	0.28
13-1	89	0.70	1.42	$0.23 \pm 0.02$	47	234	0.17	0.41
13-6	92.5	0.99	1.42	$0.32 \pm 0.03$	96	298	0.35	0.66
13-7	94.5	0.99	1.65	$0.53 \pm 0.05$	73	248	0.45	0.93
13-8	97.5	1.09	1.65	$0.75 \pm 0.15$	40	126	0.53	1.10
V-1	56	0.64	0.95	$0.24 \pm 0.01$	273	519	0.18	0.25
V-2	90	0.95	1.26	$0.32 \pm 0.01$	132	226	0.35	0.45
V-3	96	1.05	1.38	$0.41 \pm 0.02$	76	162	0.44	0.72
15-2	60	0.64	0.95	$0.33 \pm 0.01$	261	513	0.26	0.34
15-4	81	0.84	1.15	$0.32 \pm 0.01$	173	332	0.30	0.42
15-5	87	0.95	1.26	$0.37 \pm 0.01$	185	322	0.40	0.53
15-6	92	1.05	1.38	$0.43 \pm 0.02$	157	304	0.51	0.75
15-7	95.5	1.15	1.51	$0.72 \pm 0.05$	100	211	0.69	1.11
D-1	54	0.53	0.85	$0.27 \pm 0.01$	206	450	0.17	0.24
D-3	72	0.64	0.95	$0.25 \pm 0.01$	169	306	0.21	0.26
D-4	88	0.74	1.05	$0.25 \pm 0.01$	78	161	0.21	0.31
D-5	93	0.95	1.26	$0.28 \pm 0.01$	84	152	0.29	0.40
D-6	96	1.05	1.51	$0.55 \pm 0.02$	63	140	0.45	0.77

**Table IV. Relationship between Green Body Density and Intermediate-Stage Pore Size**

Sample series	$R_{eff}(0)$ ( $\mu\text{m}$ )	Green body density (%)
13-	0.19	53
V-	0.24	51
D-	0.26	50.5
15-	0.33	46

was demonstrated that this stage is consistent with the topological model of Rhines *et al.*<sup>5,10</sup> It was also shown that the average green density plays a significant role in determining the onset density at which final-stage sintering begins. The role of MgO as a sintering aid lies, at least in part, in its ability to prolong the stability of the intermediate stage of sintering such that the ceramic body achieves greater density before isolated porosity is formed.

The onset of final-stage sintering was indicated, in both the Porod scattering results and in the MSANS results, by the appearance of an increasing size of the pore radii as densification proceeded. This upturn in pore size, which was not observed to turn down again even when the density reached more than 95% of theoretical, occurred in the presence of a very significant decrease in the pore number density. Since the error bars on the pore sizes determined by the present neutron scattering studies are too large to enable an observation of the density at which the effective pore size may begin to decrease, further investigations of the final stage of sintering, with improved experimental resolution, are intended. Those studies will attempt to determine when/if the downturn in pore radius occurs as a function of densification, and what the influence of MgO additive may be on that process.

**References**

- <sup>1</sup>N. F. Berk and K. A. Hardman-Rhyne, "Characterization of Alumina Powder Using Multiple Small-Angle Neutron Scattering. I. Theory," *J. Appl. Crystallogr.*, **18** [6] 467–72 (1985).
- <sup>2</sup>N. F. Berk and K. A. Hardman-Rhyne, "Analysis of SAS Data Dominated by Multiple Scattering," *J. Appl. Crystallogr.*, **21** [6] 645–51 (1988).
- <sup>3</sup>G. G. Long and S. Krueger, "Multiple Small-Angle Neutron Scattering Characterization of the Densification of Ceramics: Application to Microporous Silica," *J. Appl. Crystallogr.*, **22** [6] 539–45 (1989).
- <sup>4</sup>S. Krueger, G. G. Long, and R. A. Page, "Characterization of the Densification of Alumina by Multiple Small-Angle Neutron Scattering," *Acta Crystallogr.*, in press.
- <sup>5</sup>G. Kostorz, *Treatise of Material Science and Technology*, Vol. 15; pp. 227–89. Academic Press, New York, 1979.
- <sup>6</sup>C. J. Glinka, "The National Bureau of Standards Small-Angle Scattering Spectrometer," *AIP Conf. Proc.*, **89**, 395–97 (1981).
- <sup>7</sup>C. J. Glinka, J. M. Rowe, and J. G. LaRock, "The Small-Angle Scattering Spectrometer at the National Bureau of Standards," *J. Appl. Crystallogr.*, **19** [6] 427–39 (1986).
- <sup>8</sup>K. A. Hardman-Rhyne and N. F. Berk, "Characterization of Alumina Powder Using Small-Angle Neutron Scattering. II. Experiment," *J. Appl. Crystallogr.*, **18** [6] 473–79 (1985).
- <sup>9</sup>F. N. Rhines and R. T. DeHoff, "Channel Network Decay in Sintering"; pp. 49–61 in *Materials Science Research*, Vol. 16, *Sintering and Heterogeneous Catalysis*. Edited by G. C. Kuczynski, A. E. Miller, and G. A. Sargent. Plenum Press, New York, 1984.
- <sup>10</sup>R. T. DeHoff, R. A. Rummel, H. P. LaBuff, and F. N. Rhines, "The Relationship Between Surface Area and Density in the Second Stage of Sintering"; pp. 301–31 in *Modern Developments in Powder Metallurgy*, Vol. 1. Edited by H. H. Hausner. Plenum Press, New York, 1966.
- <sup>11</sup>R. A. Page, S. Spooner, W. B. Sanderson, and D. L. Johnson, "Pore Evolution During Glow Discharge Sintering of Alumina," *J. Am. Ceram. Soc.*, **71** [12] 1125–29 (1988).
- <sup>12</sup>B. R. Patterson and L. A. Benson, "The Effect of Powder Size Distribution on Sintering," *Prog. Powder Metall.*, **39**, 215–30 (1983).
- <sup>13</sup>C. A. Handwerker, J. M. Dynys, R. M. Cannon, and R. L. Coble, "Dihedral Angles in Magnesia and Alumina: Distributions from Surface Thermal Grooves," *J. Am. Ceram. Soc.*, **73** [5] 1371–77 (1990).
- <sup>14</sup>S. Krueger, G. G. Long, D. R. Black, D. B. Minor, P. R. Jemian, G. W. Nieman, and R. A. Page, *J. Am. Ceram. Soc.*, in review. □

# Small-angle neutron scattering characterization of processing/microstructure relationships in the sintering of crystalline and glassy ceramics

G. G. Long and S. Krueger

*National Institute of Standards and Technology, Gaithersburg, Maryland 20899*

R. A. Gerhardt

*Rutgers University, Piscataway, New Jersey 08855*

R. A. Page

*Southwest Research Institute, San Antonio, Texas 78228*

(Received 22 April 1991; accepted 26 July 1991)

Small-angle neutron scattering measurements were used to examine the pore microstructure evolution of glassy silica and polycrystalline alpha-alumina as a function of sintering. It was shown that the two major sintering mechanisms, viscous flow and surface and volume diffusion, lead to very different microstructure evolution signatures in terms of the average pore size as a function of density. However, with respect to topology, the evolution of the porosity per unit surface area as a function of density is remarkably similar in the two systems.

## I. INTRODUCTION

Knowledge of the microstructure evolution as a function of thermal processing is important for the development of process models in ceramics. Although it is difficult to achieve a consensus regarding many aspects of sintering mechanisms, there is general agreement that the driving force for sintering is the reduction in surface free energy. The shape of the minimum free energy surface is expected to influence strongly the microstructure evolution during thermal processing. In effect, the topological characteristics of a compact from moment to moment influence the sintering mechanisms by which the pore and solid phases of the structure evolve. Such topological characteristics as the pore sizes, size distributions, surface areas, and number distributions can be monitored by small-angle neutron scattering, yielding a direct measure of the microstructure that drives the sintering.

The present investigation was undertaken to examine processing/microstructure relationships during sintering of two relatively well-understood model systems, polycrystalline alumina, in which solid-state diffusion mechanisms dominate, and porous glassy silica, in which viscous flow is dominant. The goal is to gain a quantitative measure of the structural evolution of the porous phase that takes place when different sintering mechanisms dominate densification.

In the experiments that form the subject of this paper, undoped alumina was prepared by slip casting and microporous silica was prepared by a sol-gel process. For each system, a collection or suite of nearly identical samples were prepared and sintered. During sintering,

samples were removed from the furnace one by one as they achieved intermediate densities representative of microstructures from the early part of the intermediate stage of sintering to the late part of the final stage of sintering. Microstructure parameters of these samples were derived from small-angle neutron scattering and multiple-small-angle neutron scattering, as required by the sizes and volume fractions of the pores. This process yielded a quantitative signature of the structural evolution of crystalline and glassy materials as a function of sintering.

## II. SMALL-ANGLE NEUTRON SCATTERING

Small-angle neutron scattering (SANS) is a well-recognized technique for the statistically significant characterization of microstructure in the 1 nm to 0.1  $\mu\text{m}$  size range.<sup>1</sup> This traditional size range, which is too low to include many of the microstructural features relevant to ceramic research, has recently been extended to 10  $\mu\text{m}$  by the development of a multiple-small-angle neutron scattering (MSANS) formalism.<sup>2,3</sup> The new multiple-scattering formalism is valid for samples containing a large volume fraction of open or closed pores in the size range between 0.08 and 10  $\mu\text{m}$ . For the microporous silica used in this study, MSANS was applicable to samples in the intermediate stage of sintering. For the alumina used in this study, MSANS measurements were valid from early intermediate stage through to the final stage of thermal processing. The reason that MSANS could not be used for all of the structures in this study is that an important change takes place in the microstructure morphology within one of the systems.

The application of the MSANS technique to microstructure evolution in ceramics as a function of sintering has been described earlier.<sup>4,5</sup> In this paper, the earlier measurements are reviewed and extended, and conclusions are drawn based on the existence of either glass-and-void or crystalline-and-void phases in the body.

Unlike conventional SANS, the scattering in the MSANS diffraction regime is dominated by incoherent-multiple-neutron scattering. Since the radii of the scattering pores are between 0.08 and 10  $\mu\text{m}$ , which is of the same order of magnitude as the neutron mean free path length, the neutrons scatter from only one pore at a time, even though they may scatter many times before leaving the sample. This means that there is no contribution to the measured scattering from interference between pores.

Whether a particular scattering experiment is in the SANS or in the MSANS regime is determined by the phase shift  $\nu$  that a neutron undergoes in traversing a particle of radius  $R$ . The phase shift depends on three parameters: the contrast<sup>4</sup>  $\Delta\rho$  of the pore relative to the matrix, the neutron wavelength  $\lambda$ , and the particle size  $2R$ .

$$\nu = 2\Delta\rho\lambda R. \quad (1)$$

In SANS,  $\nu \ll 1$ , whereas in MSANS,  $0.1 \leq \nu \leq 2$ .

A measure of the amount of multiple scattering is given by the parameter  $\bar{z}$ , called the scattering power,<sup>2</sup> which is the sample thickness  $z$  divided by the neutron mean free path length  $l$

$$\bar{z} = z/l = 1.5\phi z(\Delta\rho\lambda)^2 R. \quad (2)$$

$\phi$  is the volume fraction of scatterers, which for ceramic bodies more than 50% dense is  $(1 - d/d_{th})$ , where  $d$  is the sample density and  $d_{th}$  is the theoretical density of a fully densified body. In the present case,  $\phi$  is the porosity.  $\Delta\rho$  is the neutron scattering length density<sup>5</sup> of the pores relative to the matrix (that is, the particles) mentioned above,  $\lambda$  is the neutron wavelength, and  $R$  is the mean effective radius of the pores. From a materials perspective, the greater the number of pores and the larger their size, the greater the multiple scattering. However, even if the pore volume fraction is small, as in the final stage of sintering, if the remaining pores have large radii, multiple scattering measurements can still be carried out successfully, provided that the samples are thick enough and long wavelength neutrons (of the order of 1.2 to 2 nm) are available. For sintering of microporous silica, the pore structure within the samples representative of the final stage could not be measured by MSANS, and the structural evolution measurements had to be completed using SANS measurements. The absence of MSANS for the final stage densification of silica implies that there are no large spherical pores left, as will be explained below. For conventional sintering of alumina, the entire pore evolution from early intermediate stage to late final stage can be observed by means of

MSANS because even the residual pores near the end of final-stage sintering can be approximated by spheres and are large enough to be measured. It was found that the measurement techniques that can be used yield important clues as to the differences that will be observed between the sintering of these crystalline and glassy systems.

The MSANS analysis assumes that the scatterers can be described as spheres with no internal structure in a featureless matrix. Of course, the pores in both systems have no internal structure. For the silica case, the single colloidal particles and the particle agglomerates have been shown<sup>6</sup> to be spherical. The voids between the particles for porosities between 85% and 50% were shown in Ref. 6 to be reasonably well approximated by spheres. The point at which the pores may become isolated could not be determined in that work. However, the matrix is always glassy, and thus it is relatively featureless. For alumina, the crystalline matrix contains features such as dislocations which will cause scattering. Such structures do not generally fall into the same size range as the pores and are thus outside the region of sensitivity of MSANS. For alumina, the spherical approximation for the shape of the isolated pores is applicable to the final stage of sintering, but there is some question as to how well the method will perform during the intermediate stage of sintering when the pores form an interconnected network of cylindrical channels. Relevant to this concern, it was found<sup>4</sup> that the spherical approximation is valid provided that the cylindrical channels can be modeled by strings of spheres. This will be true when the length dimension of the cylinders is beyond the range of sizes measured by MSANS. For intermediate stage sintering of alumina, the length of the interconnected pore channels may be well beyond 10  $\mu\text{m}$ . Supporting evidence for the validity of the strings-of-spheres approximation for alumina comes from mercury intrusion porosimetry (MIP) measurements on the same intermediate stage samples. In MIP, a cylindrical morphology is assumed for the pore shape. Since the MIP results<sup>5</sup> and the MSANS results showed the same behavior, this can be taken as evidence that each approximation serves appropriately in the respective method.

In conventional SANS, the width of the scattering curve as a function of scattering wave vector  $\mathbf{Q}$  (where  $|\mathbf{Q}| = (4\pi/\lambda) \sin \theta$ , and  $2\theta$  is the scattering angle) is independent of the incident neutron wavelength. In MSANS, the width of the scattering curve changes as a function of wavelength; that is, there is wavelength-dependent beam-broadening. Thus, with the phase shift between 0.1 and 2, with the pore size between 0.08 and 10  $\mu\text{m}$ , and with  $\bar{z} \geq 10$ , the wavelength dependence of the MSANS data can be used to obtain useful pore size information. By studying the samples over a range of incident neutron wavelengths, the statistics of the data refinement are significantly improved. The parameters

required for the data analysis are sample thickness  $z$ , material contrast  $\Delta\rho$ , the scattering volume fraction  $\phi$  (which is the same as the porosity), and the wavelength dependence of the beam broadening over at least three, and preferably more, wavelengths.

Even under scattering conditions where the low-wave-vector portion of the scattering curve near  $Q = 0$  is dominated by multiple scattering, the large-wave-vector portion of the scattering curve, defined by  $QR \geq 10$ , follows<sup>2</sup> single particle Porod<sup>7</sup> scattering. This means that the usual analysis of the large- $Q$  portion of the scattering curve can be carried out independent of the existence of MSANS at low- $Q$ . This is very useful, because a Porod analysis yields values for the total surface scattering area of the pores.

$$\frac{d\Sigma}{d\Omega} = \frac{2\pi(\Delta\rho)^2 S}{VQ^4} \quad (3)$$

$V$  is the sample volume in the neutron beam and  $S$  is the total surface area of the scattering pores. From this the Porod constant  $P$  can be defined as

$$P = 2\pi(\Delta\rho)^2(S/V), \quad (4)$$

and one has a direct measure of the total surface area of the pores per unit volume that is independent of model for the pore shape. If the pores can be assumed to be spherical, one has another measure of their size since  $R = 3\phi(V/S)$ , and one can also obtain a value for their number density from  $N_p = (S/V)[1/(4\pi R^2)]$ .

### III. SAMPLES

The silica samples were prepared by the Shoup<sup>8</sup> technique from 85 wt. % potassium silicate and 15 wt. % colloidal silica. Detailed information on sample preparation is given elsewhere.<sup>9</sup> The porosity of the nominally alkali-free (<100 parts in  $10^6$  Na and K) precursor body was 84%. Each of the samples was subjected to a firing temperature above the onset of sintering, which occurs between 1420 and 1470 K, depending on the average pore size of the dried precursors. Crystallization was carefully avoided in the sintering of this material. The densities of the small-angle neutron scattering samples were between 60% and 98% of theoretical density (TD), where the TD for silica is  $2.20 \text{ g cm}^{-3}$ . Thus the samples are representative of intermediate-stage to final-stage thermal processing.<sup>10</sup> The silica sample characteristics are given in Table I.

The alumina samples were prepared from Baikowski alumina powder (CR6,  $6 \text{ m}^2 \text{ g}^{-1}$ ), and were slipcast to an average green density of  $52.8 \pm 0.4\%$  TD, where TD for alumina is  $3.965 \text{ g cm}^{-3}$ . Detailed information on sample preparation is given elsewhere.<sup>5</sup> During sintering, the samples were removed from the furnace one at a time, yielding examples of microstructure between 56

TABLE I. Silica samples.

Sample number	Porosity $\phi$	Thickness, cm	Density, $\text{g cm}^{-3}$
1	0.40	0.487	1.30
2	0.35	0.142	1.42
4	0.30	0.123	1.56
5	0.26	0.122	1.63
6	0.05	0.486	2.09
7	0.05	0.113	2.10
9	0.02	0.130	2.15

and 98% TD. The alumina sample characteristics are given in Table II.

### IV. MULTIPLE SCATTERING MEASUREMENTS

The neutron scattering measurements were performed at the 20 MW research reactor at the National Institute of Standards and Technology (NIST). The NIST SANS facility<sup>11</sup> makes use of a velocity selector for choosing the mean wavelength of the incident neutrons, which have a wavelength spread of  $\Delta\lambda/\lambda = 0.25$ . Copious neutron fluxes are available in the wavelength region between 0.5 and 2.0 nm due to a cryogenic moderator installed in the reactor core. The neutron beam was collimated with a 12 mm aperture following the velocity selector and an 8 mm aperture preceding the sample position. Scattered neutrons were detected by a  $64 \times 64 \text{ cm}^2$  position-sensitive detector divided into 128  $\times$  128 pixels. The data were circularly averaged to produce one-dimensional intensity  $I(Q)$  versus scattering vector  $Q$  curves.

In conventional SANS, a beamstop is used in the center of the scattering pattern to protect the detector from the unscattered transmitted beam. This transmitted beam is  $10^3$  to  $10^7$  times greater in intensity than the scattered beam. For MSANS, measurements were performed with no beamstop in place since the intense transmitted beam associated with SANS is absent. Performing the measurements without a beamstop ensures that the beam

TABLE II. Alumina samples.

Sample number	Porosity $\phi$	Thickness, cm	Density, $\text{g cm}^{-3}$
t3-2	0.46	1.019	2.15
13-3	0.35	0.988	2.59
13-4	0.21	0.894	3.15
t3-5	0.15	0.914	3.39
13-1	0.11	0.851	3.55
t3-6	0.075	0.852	3.69
t3-7	0.055	0.840	3.77
t8-8	0.025	0.804	3.89

center can be located with good precision, and enables an accurate determination of the beam-broadening of the  $I(Q)$  curve at  $Q = 0$ . Measurement times were of the order of 10 min to 1 h, depending on the amount of multiple scattering present.

MSANS measurements were made at a minimum of five wavelengths per alumina sample. Multiple scattering curves from one of the alumina samples (13-5) are shown in Fig. 1, where all of the curves have been normalized to  $I(0) = 1$ . The feature at  $Q \approx 0.05 \text{ nm}^{-1}$ , which appears in all of the broadened spectra, is due to a change in the detector sensitivity near  $Q = 0$ . To avoid this region, Gaussian fits to the data were made beginning at 85–90%  $I(0)$  and extending out to approximately 45%  $I(0)$ . Below 40%  $I(0)$ , as the theory predicts, the curves are not well-described by a Gaussian. For the silica samples, the region that was distorted by the changes in detector sensitivity was larger because a different portion of the detector was used. Therefore, the silica curves could be fit only between 75% and 40% of  $I(0)$ .

The wavelength dependent beam-broadening of the MSANS curves is described as a radius of curvature,  $r_c$ , at  $Q = 0$  in the scattering curve, in keeping with the earlier literature.<sup>2,3</sup> For each scattering curve, a radius of curvature was extracted from the fitted standard deviation  $\sigma$ , such that  $r_c = (1/2\sigma)^{1/2}$ . Blank spectra, measured at each wavelength with no sample in place, were also measured to enable a correction<sup>12</sup> for instrumental broadening. The radii of the pores were extracted from each curve using an empirical formula<sup>3</sup> for the description of the MSANS:

$$r_c[QR] = 0.926 \{ \bar{z} \ln^{0.85} \bar{z} \}^{0.5} \quad \text{for } \bar{z} \geq 10, \quad (5)$$

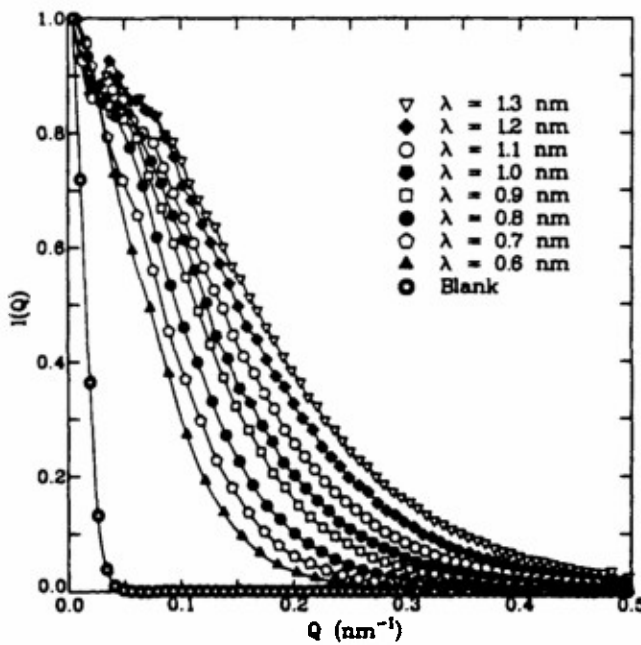


FIG. 1. MSANS curves from alumina sample 13-5.

where  $\bar{z}$  is given by Eq. (2) and [...] means "with respect to" and defines the scale for describing  $r_c$ . The values of  $R$ , derived from the fitted values of  $r_c$ , are averaged together to obtain an effective radius  $R_{\text{eff}}(0)$  for the scattering pores in the sample. The (0) is a reminder that this value of the pore radius comes from the  $Q = 0$  portion of the scattering curve. Later in this paper, another pore radius will be derived from the large  $Q$  (Porod) portion of the scattering curves, and it will be referred to as  $R_{\text{eff}}(\infty)$ .

To complete the MSANS analysis, both  $R_{\text{eff}}(0)$  and the scattering volume fraction  $\phi$  are refined simultaneously for each sample using a least-squares fitting procedure. Due to the approximate nature of Eq. (5), the full numerical MSANS analysis describing the dependence of the radius of curvature on neutron wavelength, developed in Eqs. (2.12)–(2.15) of Ref. 2, was used in the refinement procedure.

The measured  $r_c$ 's as a function of wavelength for the silica samples are shown in Fig. 2, and the measured  $r_c$ 's versus  $\lambda$  for the alumina samples are shown in Fig. 3. The lines in Figs. 2 and 3 are the theoretical curves determined by means of the MSANS formalism. The data for silica sample 4, with  $\phi = 0.3$  was too close to the data for silica sample 5 with  $\phi = 0.26$ , so it was omitted from the figure for clarity. Nevertheless, both figures indicate good agreement between the theory and the measurements, demonstrating that the MSANS formalism is well-suited to the analysis of these porous microstructures.

It is interesting to note that, regardless of whether the phase of the material is glassy or crystalline, the  $r_c$

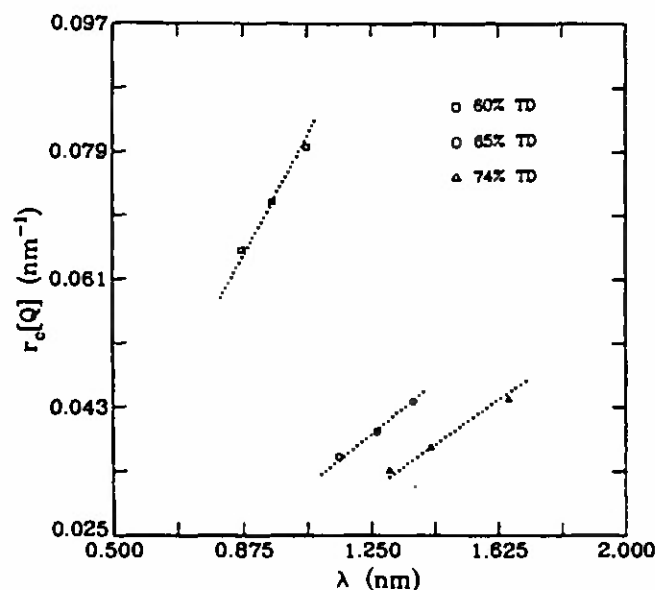


FIG. 2. Radii of curvature for the silica samples derived from the data (symbols) and calculated from the theory (dotted lines) as a function of neutron wavelength.

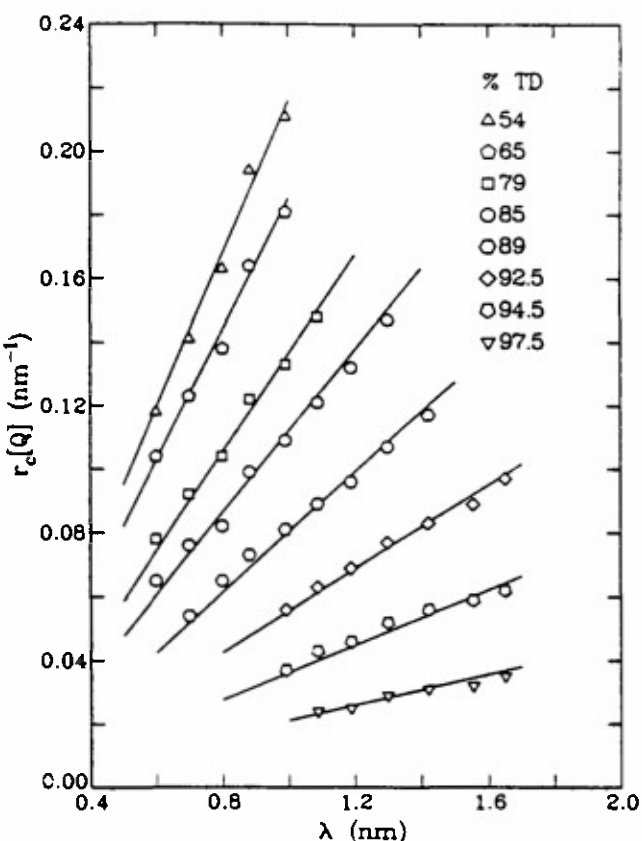


FIG. 3. Radii of curvature for the alumina samples derived from the data (symbols) and calculated from the theory (solid lines) as a function of neutron wavelength.

versus  $\lambda$  curves have the steepest slopes for the data from the samples with the largest volume fraction of pores, and the shallowest slopes for the data from the samples with the least porosity. This trend was observed also<sup>13</sup> in MSANS data from alumina samples that had been doped with 0.25 wt. % MgO. The results indicate that while the size of the pores may be increasing, decreasing, or remaining constant as the porosity is decreasing, the general trend of the  $r_c$  versus  $\lambda$  curves is observed to behave as shown in Figs. 2 and 3. Thus, even though both  $\phi$  and  $R_{\text{eff}}(0)$  are implicit in these curves, the slope is dominated by the volume fraction of pores  $\phi$ .

## V. RESULTS AND DISCUSSION

Results from the sintering of microporous silica are considered first. The Porod results for silica are given in Table III. The Porod analysis yields directly a value for the total surface scattering area. This surface area, normalized to unit volume of sample in the neutron beam, is generally seen to decrease as densification proceeds. Assuming a spherical shape for the pores, a value for their average radius  $R_{\text{eff}}(\infty)$  can be derived, and this is also given in Table III. The average radius is first seen to coarsen and then to shrink. Finally the radius appears to become very large, which is hard to understand unless this is taken as evidence that the spherical approximation fails for the pore shape in silica over 95% TD. Since it will be demonstrated that the pore morphology in final-stage silica is disk-like, the last two numbers in Table III are not physically meaningful and are left for reference purposes only. Another parameter, the pore volume fraction divided by the surface area normalized to unit volume, is also shown in Table III. Since this is a topological parameter, all of the values for  $\phi(S/V)$  shown in the table are physically relevant. More will be said about the meaning of this parameter below.

Near  $Q = 0$ , MSANS was used to measure the average pore sizes of microporous silica. During the intermediate stages of thermal processing there was a considerable amount of wavelength-dependent broadening; however, there was no detectable broadening in the late stage samples, even with the longest wavelength neutrons (2 nm) and the thickest samples. In an earlier study,<sup>4</sup> it was demonstrated that pores with radii between 0.08 and 3  $\mu\text{m}$  would have produced detectable broadening using the longest wavelength neutrons available. The absence of such broadening in the final stage indicates that the large sphere-like voids present during the intermediate stage of sintering were completely removed before the silica reached 95% TD. To observe the pore population in the late stage of sintering, measurements were made by means of SANS. In the SANS analysis, the scattering pore size was estimated by fitting the small

TABLE III. Silica Porod results.

Sample number	Porod constant, $\times 10^{26} \text{ cm}^{-5}$	$S/V \times 10^4 \text{ cm}^{-1}$	Porosity $\phi, \%$	$\phi/(S/V) \times 10^{-6} \text{ cm}$	$R_{\text{eff}}(\infty) \text{ nm}$
1	$12.7 \pm 0.34$	$16.98 \pm 0.40$	40	$2.36 \pm 0.06$	$71 \pm 2$
2	$8.42 \pm 0.14$	$11.26 \pm 0.18$	35	$3.11 \pm 0.05$	$93 \pm 2$
4	$9.54 \pm 0.12$	$12.76 \pm 0.16$	30	$2.35 \pm 0.03$	$70 \pm 1$
5	$7.88 \pm 0.04$	$10.54 \pm 0.05$	26	$2.46 \pm 0.01$	$74 \pm 0.5$
6	$0.283 \pm 0.002$	$0.378 \pm 0.003$	5	$13.2 \pm 1.0$	$397 \pm 28$
9	$0.118 \pm 0.001$	$0.156 \pm 0.001$	2	$12.8 \pm 0.8$	$384 \pm 32$

$Q$  scattering data to the Guinier equation<sup>14</sup>

$$I(Q) = I(0) \exp\left(-\frac{Q^2 R_g^2}{3}\right) \quad (6)$$

where  $R_g$  is the radius of gyration of the pores and  $I(0)$  is the extrapolated scattering intensity at  $Q = 0$ . The SANS results on the late stage samples revealed the presence of small pore populations with radii of gyration 33 nm and less. The MSANS and SANS results are shown in Table IV. It can be seen that the pores first coarsen and then shrink abruptly as the silica densifies. These results support a model<sup>9</sup> proposed for this system in which there are two distinct populations of pores. There is a population of small pores that exist within loosely aggregated clusters or "domains" of closely-packed fine silica particles. These pores within domains are actually voids between touching particles. Also there is a population of large pores that are found between domains. The latter population of pores dominates the MSANS data. The small pores are less stable and thus are eliminated first, causing the domains to densify and the interdomain pores to coarsen. When the intradomain pores have disappeared, the interdomain pores can stop coarsening and begin to shrink. These small-angle neutron scattering results indicate that it is possible to determine exactly when domain densification is complete.

Comparing the Porod and the MSANS and SANS results for pore radius, one can see that the Porod-derived radius, which is a measure of all of the porosity but weighted toward the smaller pore population, begins to decrease earlier than the MSANS-derived radius. This can be taken as evidence of the existence of the population of small pores that is beyond the range of visibility of the MSANS. With regard to the final-stage data, the lack of MSANS indicates that there are no large pores left while the Porod results imply the presence of large pores. The apparent contradiction is removed when one considers the question of the final stage silica pore shape. For the final stage, consistency among all the results is achieved only when the pore shape is taken as disk-like. The scattered intensity from disk-like pores of

finite thickness,  $T$ , and a much larger diameter can be written as<sup>15</sup>

$$I(Q) = A \cdot \frac{2\pi}{Q^2} I_t(Q), \quad (7)$$

where  $A$  is a constant and  $I_t(Q)$  is the "thickness factor". Analogous to Eq. (6),  $I_t(Q)$  can be approximated at small  $Q$  by

$$I_t(Q) = I_t(0) \exp(-Q^2 R_t^2) \quad (8)$$

where  $R_t = T/\sqrt{12}$ . Thus, by fitting  $I(Q) \cdot Q^2$  vs  $Q^2$  at small  $Q$ ,  $T$  can be obtained. The results are given in Table IV. Thus, if the final-stage porosity in the microporous silica is taken to be disk-like, the radii of gyration measured by means of SANS indicate disk thicknesses of  $\lesssim 50$  nm.

Finally, electron microscope micrographs were taken from fracture surfaces of the 74% and the 95% dense silica. These are shown in Figs. 4(a) and 4(b). At 74%, the porosity is still interconnected by large cylindrical pores, but some narrow porosity has also formed. By 95% dense, the microstructure contains no large pores and only the narrow collapsed porosity is seen. These micrographs confirm the change in pore morphology observed by MSANS and SANS.

Next the alumina results are considered. The Porod results for alumina are given in Table V. The surface area per unit volume decreases monotonically as densification proceeds. However, the pore radius, assuming spheres, is seen to be relatively constant during the intermediate stage of sintering, and increases rapidly during the final sintering stage.

The MSANS results for alumina are given in Table VI, where, unlike silica, MSANS characterization could be used throughout. It can be seen from the table that the effective size of the pores is almost constant over the entire range of densities representative of intermediate stage sintering, from approximately 55% TD to about 87% TD. Above 87% TD, the sizes of the pores increase rapidly, despite the sharp decrease in their numbers. This trend, i.e., constant pore radius in

TABLE IV. MSANS and SANS results from silica.

Sample number	Porosity $\phi$ , %	$R_{\text{eff}}(0)$ , $\mu\text{m}$	$T$ , nm	$\bar{z}$		$v$	
				min	max	min	max
1	40	$0.176 \pm 0.01$	...	32	72	0.11	0.14
2	35	$0.225 \pm 0.015$	...	21	38	0.19	0.34
4	30	$0.223 \pm 0.015$	...	22	49	0.21	0.36
5	26	$0.118 \pm 0.02$	...	16	31	0.15	0.28
6	5	<0.08	...				
7	5	...	$45 \pm 6$				
9	2	<0.08	$49 \pm 4$				

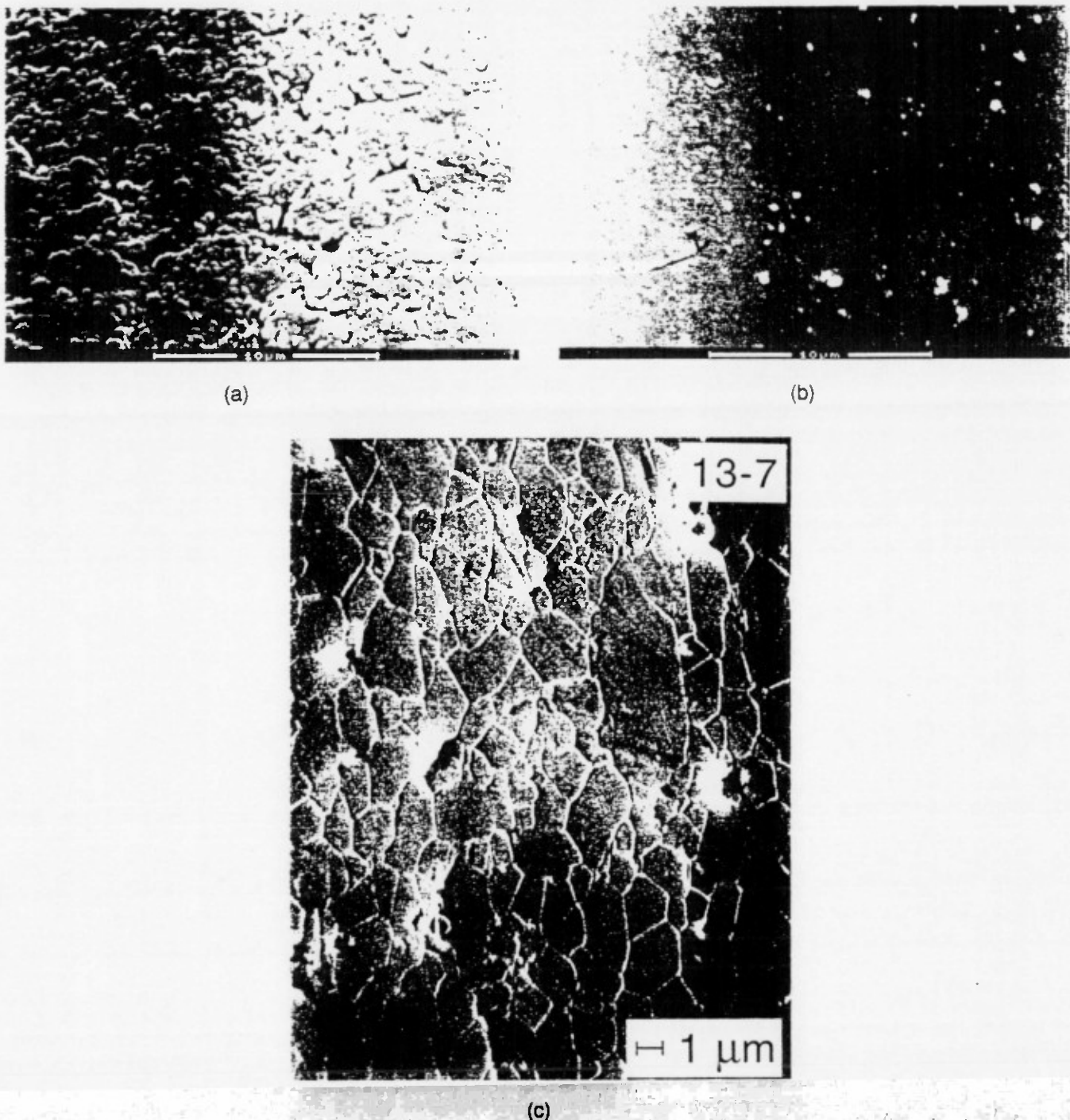


FIG. 4. Scanning electron micrographs of (a) a fracture surface of 74% dense microporous silica, (b) a fracture surface of 95% dense microporous silica, and (c) a polished surface of 95% dense alumina.

the intermediate sintering stage and rapidly increasing pore radius in the final sintering stage, is also seen for  $R_{\text{eff}}(\infty)$  which was derived from Porod scattering, where a spherical approximation was made for the pore shape. The qualitative agreement between the Porod and the MSANS results for average pore radius suggests that, unlike silica, there is only one pore-size distribution

present in alumina. The MSANS results are weighted toward the larger pores in the distribution and the Porod results are weighted toward the smaller pores in the distribution, but it appears that there is only one distribution present.

The constant pore radius in the intermediate sintering stage of alumina lends support to the topolog-

TABLE V. Alumina Porod results.

Sample number	Porod constant $\times 10^{26} \text{ cm}^{-5}$	$S/V$ $\times 10^4 \text{ cm}^{-1}$	Porosity $\phi, \%$	$\phi/(S/V)$ $\times 10^{-6} \text{ cm}$	$R_{\text{eff}}(\infty)$ nm
13-2	31.3 $\pm$ 0.4	15.2 $\pm$ 0.2	46	3.03 $\pm$ 0.04	91 $\pm$ 1
13-3	20.0 $\pm$ 0.2	9.71 $\pm$ 0.1	35	3.60 $\pm$ 0.04	108 $\pm$ 1
13-4	12.0 $\pm$ 0.07	5.83 $\pm$ 0.03	21	3.60 $\pm$ 0.02	108 $\pm$ 1
13-5	7.70 $\pm$ 0.04	3.74 $\pm$ 0.02	15	4.01 $\pm$ 0.02	120 $\pm$ 1
13-1	4.42 $\pm$ 0.03	2.15 $\pm$ 0.01	11	5.12 $\pm$ 0.02	154 $\pm$ 1
13-6	2.51 $\pm$ 0.011	1.218 $\pm$ 0.005	7.5	6.16 $\pm$ 0.03	185 $\pm$ 1
13-7	1.14 $\pm$ 0.006	0.553 $\pm$ 0.003	5.5	9.93 $\pm$ 0.04	298 $\pm$ 2
13-8	0.355 $\pm$ 0.0009	0.5123 $\pm$ 0.0009	2.5	14.5 $\pm$ 0.9	440 $\pm$ 90

ical decay model of Rhines and DeHoff<sup>16</sup> in which the interconnected channel network of pores decays in a stable manner. During the intermediate stage, the interconnected pore channels are expected to decay such that the volume fraction to surface area per unit volume,  $\phi/(S/V)$ , remains constant,<sup>17</sup> as can be seen from Table V. Consequently, the pore channels become fewer, while retaining the same diameter, as densification proceeds. At the onset of final-stage sintering, the pore radius coarsens abruptly. Part of this apparent coarsening may be due to the pinching off of pore channels such that the larger dimension of the newly-isolated pores comes increasingly within the range of sizes visible to the MSANS technique. The error bars on these late-stage radii are large because it is difficult to fit the shallow slopes of the relevant  $r_c$  versus  $\lambda$  curves. The authors have recently attempted to improve the precision of these results with independent measurements using high-resolution small-angle x-ray measurements<sup>18</sup> on the same late-stage alumina samples. The new results confirm the average pore sizes and the trends shown here. A micrograph of a polished surface of the 95% dense sample is shown in Fig. 4(c).

The behavior of the total surface area of the pores, as a function of densification, is shown in Fig. 5 for both silica and alumina. Although there are some quantitative differences below 80% TD, it is interesting to see that the total surface area of the pores in the glassy system and

in the crystalline system falls on the same densification curve. Next, the parameter  $\phi/(S/V)$ , which was taken above to be an indicator of the existence of a topologically stable sintering stage in intermediate stage sintering of alumina, is compared for the densification of alumina and silica in Fig. 6. The topology of the microstructure evolution of silica and alumina are on the same general curve. This is a remarkable result. The pore morphology for the polycrystalline alumina goes from interconnected cylindrical channels to pinched-off sphere-like shapes; the pore morphology for the glassy silica goes from interconnected cylindrical channels to a collapsed disk-like shape that is largely interconnected even at 95% dense. Nevertheless, the topological parameter  $\phi/(S/V)$  evolves in the same general manner during the sintering of both.

The SANS and MSANS results for the pore radius as a function of densification are compared for the two systems in Fig. 7. In this figure, the differences in signatures of the sintering of a glass undergoing viscous flow and crystalline material densifying mainly by surface and volume diffusion are evident. The glassy silica flows such that the smaller voids are first removed, causing the temporary coarsening of the largest pores. The point at which all the intradomain pores have vanished can easily be seen. After that point, the large pores shrink rapidly and eventually collapse as the silica sinters to full theoretical density. The alumina densifies by the

TABLE VI. MSANS results for alumina.

Sample number	Porosity $\phi, \%$	$R_{\text{eff}}(0)$ $\mu\text{m}$	$\bar{z}$		$\nu$	
			min	max	min	max
13-2	46	0.20 $\pm$ 0.01	152	415	0.13	0.22
13-3	35	0.19 $\pm$ 0.01	98	289	0.12	0.21
13-4	21	0.17 $\pm$ 0.005	49	193	0.10	0.22
13-5	15	0.18 $\pm$ 0.01	32	204	0.09	0.28
13-1	11	0.23 $\pm$ 0.02	47	234	0.17	0.41
13-6	7.5	0.32 $\pm$ 0.03	96	298	0.35	0.66
13-7	5.5	0.53 $\pm$ 0.05	73	248	0.45	0.93
13-8	2.5	0.75 $\pm$ 0.15	40	126	0.53	1.10

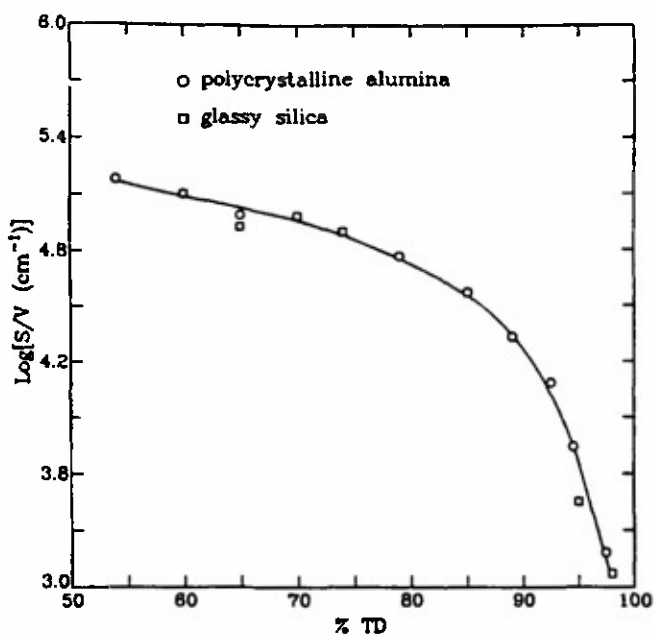


FIG. 5. Total surface scattering area per unit volume ( $S/V$ ) as a function of densification (i.e., percent theoretical density) for silica and alumina.

stable removal of pore channels one by one from an interconnected network. During this intermediate stage, the average pore channel radius remains constant. Only in the final stage, in contrast to the silica, do the isolated pores exist and require the proximity of grain boundaries for their ultimate removal.

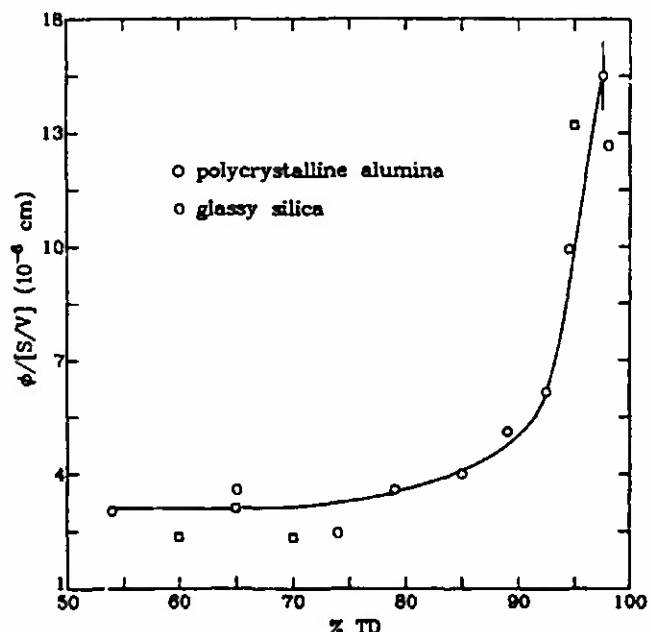


FIG. 6. Pore volume fraction, normalized to  $S/V$ , as a function of densification (% TD) for silica and alumina.

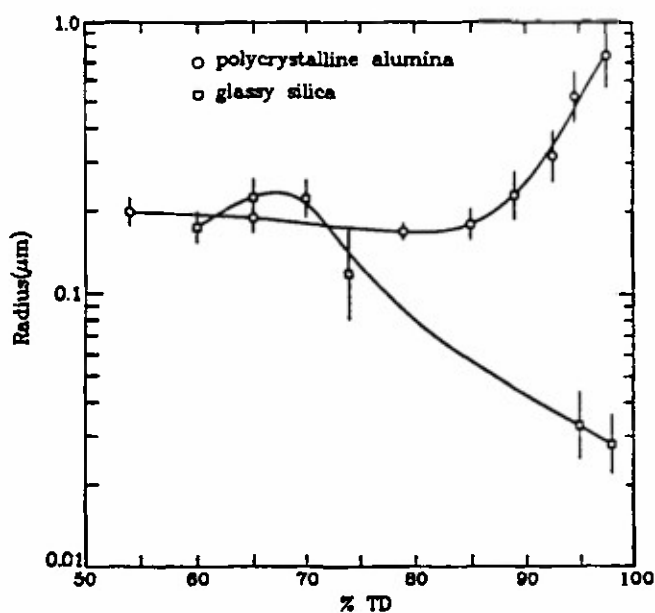


FIG. 7.  $R_{\text{eff}}(0)$  as a function of percent theoretical density for silica and alumina.

## VI. SUMMARY AND CONCLUSIONS

Small-angle neutron scattering measurements were used to examine the evolution of the porous microstructure of ceramic bodies as a function of densification. Topologically, both systems were shown to evolve in the same way. However, the structural evolution in terms of pore size and morphology displays a different characteristic signature depending on the sintering mechanism that is operative. For the densification of a glassy ceramic, porous silica, the densification path that is observed is attributed to the viscous flow mechanism of densification and to the absence of a grain boundary. For the densification of a crystalline ceramic, polycrystalline alpha-alumina, the densification path that is observed is attributed to the dominance of diffusion sintering mechanisms and to the conditions imposed by the existence of the grain boundary. Whereas the density of the green body established the radius of the interconnected pore channels, which was constant throughout intermediate stage sintering in alumina, the density of the green body may play a less important role in the sintering of glassy silica.

## ACKNOWLEDGMENTS

The authors gratefully acknowledge support for this work from the United States Army Research Office through Contract No. MIPR-ARO-102-90, and from the United States Department of Energy under Contract No. DE-FG05-84ER45063.

## REFERENCES

1. G. D. Wignall, in *Transactions of the American Crystallographic Association*, edited by P. W. Schmidt (Am. Cryst. Assoc., New York, 1983), Vol. 19.
2. N. F. Berk and K. A. Hardman-Rhyne, *J. Appl. Cryst.* **18**, 467-472 (1985).
3. N. F. Berk and K. A. Hardman-Rhyne, *J. Appl. Cryst.* **21**, 645-651 (1988).
4. G. G. Long and S. Krueger, *J. Appl. Cryst.* **22**, 539-545 (1989).
5. S. Krueger, G. G. Long, and R. A. Page, *Acta Cryst. A* **47**, 282-290 (1991).
6. H. Kerch, R. A. Gerhardt, and J. L. Grazul, *J. Am. Ceram. Soc.* **73**, 2228-2237 (1990).
7. G. Kostorz, *A Treatise on Materials Science and Technology*, edited by H. Herman (Academic Press, New York, 1979), Vol. 15, pp. 227-289.
8. R. D. Shoup, *Colloid Interface Sci.* **3**, 63-69 (1976).
9. W. Cao, R. A. Gerhardt, and J. B. Wachtman, Jr., *J. Am. Ceram. Soc.* **71**, 1103-1113 (1988).
10. G. W. Scherer, *J. Am. Ceram. Soc.* **60**, 236-239 (1977).
11. C. J. Glinka, in *Neutron Scattering, A.I.P. Conf. Proc. No. 89* pp. 393-397 (1981), and C. J. Glinka, J. M. Rowe, and J. G. LaRock, *J. Appl. Cryst.* **19**, 427-439 (1986).
12. K. A. Hardman-Rhyne and N. F. Berk, *J. Appl. Cryst.* **18**, 473-479 (1985).
13. G. G. Long, S. Krueger, and R. A. Page, *J. Am. Ceram. Soc.* **74**, 1578-1584 (1991).
14. A. Guinier and G. Fournet, *Small-Angle Scattering of X-rays* (John Wiley, New York, 1955), p. 25.
15. G. Porod, in *Small-Angle X-ray Scattering*, edited by O. Glatter and O. Kratky (Academic Press, New York, 1982), pp. 35-36.
16. F. N. Rhines and R. T. DeHoff, in *Sintering and Heterogeneous Catalysis*, edited by G. C. Kuczynski, A. E. Miller, and G. A. Sargent, *Mater. Sci. Res.* **16** (Plenum Press, New York, 1984), pp. 49-61.
17. R. T. DeHoff, R. A. Rummel, H. P. LaBuff, and F. N. Rhines, in *Modern Developments in Metallurgy*, edited by H. H. Hausner (Plenum Press, New York, 1966), pp. 301-331.
18. S. Krueger, G. G. Long, D. R. Black, D. Minor, P. R. Jemian, G. W. Nieman, and R. A. Page, *J. Am. Ceram. Soc.* (1991, in press).